The interplay between magnetic fields and kinematics in low-mass star formation

Farideh S. Tabatabaei

München 2025

The interplay between magnetic fields and kinematics in low-mass star formation

Farideh S. Tabatabaei

Dissertation
der Fakultät für Physik
der Ludwig-Maximilians-Universität
München

vorgelegt von
Farideh S. Tabatabaei
aus Qom, Iran

München, den 18.02.2025

Erstgutachter: Prof. Dr. Paola Caselli
Zweitgutachter: Prof. Dr. Til Birnstiel
Tag der mündlichen Prüfung: 02.04.2025

Contents

List of Figures

List of Tables

Zusammenfassung

Die Erforschung der Geschichte der Sternentstehung ist bei massearmen Sternen wie unserer Sonne besonders faszinierend, da sie in direktem Zusammenhang mit der Geschichte unseres eigenen Sonnensystems steht. Bei massearmen Sternen werden die physikalischen und chemischen Eigenschaften in erster Linie durch ihre dichten Kerne bestimmt. Diese dichten Kerne haben ihren Ursprung in lokalen Verdichtungen innerhalb von Molekülwolken, die häufig in fadenartigen Strukturen im interstellaren Medium (ISM) zu finden sind. Daher ist die Erforschung der Sternentstehung untrennbar mit der Analyse von Molekülwolken und deren filamentären Strukturen verbunden. Filamente, langgestreckte Strukturen im ISM, sind von zentraler Bedeutung für den Sternentstehungsprozess. Beobachtungsstudien haben immer wieder ihre Allgegenwart und ihre universellen Eigenschaften hervorgehoben und ihre Rolle bei der Bildung von dichten Kernen und Sternen unterstrichen. Diese Strukturen werden durch das komplexe Zusammenspiel von Turbulenzen, Magnetfeldern und Schwerkraft geformt. An den Schnittpunkten von Filamenten ist die Dichte oft erhöht, was zu Knotenpunkten führt, in denen Haufen und massereiche Sterne entstehen können. Diese Arbeit konzentriert sich auf das Verständnis des Einflusses von Magnetfeldern und Kinematik auf die Dynamik und Stabilität von filamentären Strukturen.

Das erste Projekt untersucht den protostellaren Kern IRAS15398-3359, ein junges stellares Objekt der Klasse 0 in seinem frühen Entstehungsstadium. Anhand von Molekülllinienbeobachtungen von $C^{18}O$ (2-1) und DCO^{+} (3-2) mit dem APEX-Teleskop habe ich die kinematischen und magnetischen Eigenschaften des Kerns analysiert. Der Geschwindigkeitsgradient um den Protostern zeigte Materialzufluss und -abfluss, was auf die Verschmelzung von filamentären Strukturen in der Nähe des Kerns hindeutet. Polarisationsdaten zeigten eine stark übereinstimmende Ausrichtung zwischen dem Magnetfeld und der Rotationsachse des Kerns, was die regulierende Rolle des Magnetfelds während des Kollapses verdeutlicht.

Das zweite Projekt konzentriert sich auf ein isoliertes Filament östlich des Klumpens Barnard 59 im Pfeifennebel. Um die Magnetfelstruktur und -stabilität des Filaments zu untersuchen, wurden Polarisationsbeobachtungen aus dem Nahinfrarot mit Daten von Molekülllinien kombiniert. Die geschätzte Magnetfeldstärke, hergeleitet mit der Davis-Chandrasekhar-Fermi-Methode, spricht gegen einen radialen Kollaps. Das radiale Dichteprofil des Filaments, modelliert mit polytropen zylindrischen Modellen, deutet darauf hin, dass nicht-thermische Bewegungen und Magnetfelder eine dominante Rolle bei der Aufrechterhaltung der Stabilität spielen. Außerdem wurde ein Gasfluss in Richtung des Knotenpunkts beobachtet, was die Dynamik des Filaments mit der Sternentstehungsaktivität in der Re-

gion in Verbindung bringt.

Das letzte Projekt untersucht das Snake-Filament, eine auffällige Struktur mit besonderen magnetischen und kinematischen Eigenschaften. Um das Filament zu charakterisieren, verwendete ich Polarisationsdaten aus dem Optischen und Nahinfraroten, sowie Beobachtungen der $C^{18}O$ (1-0) und ^{13}CO (1-0) Moleküllinien. Die Ergebnisse zeigen eine überwiegend parallele Magnetfeldausrichtung in den Regionen mit geringerer Dichte, mit einem signifikanten Geschwindigkeitsgradienten entlang des Filamentrückens. Die Polarisationseffizienz nimmt mit zunehmender visueller Extinktion ab, übereinstimmend mit einer geringeren Ausrichtung der Körner in dichteren Bereichen.

Diese Studien zeigen die entscheidende Rolle von Magnetfeldern und Kinematik bei der Bildung von Filamentstrukturen und der Regulierung der Sternentstehung. Zukünftige Beobachtungen mit höherer Auflösung und Sensitivität werden die komplexen Beziehungen zwischen Filamenten, Magnetfeldern und Sternentstehung weiter aufdecken und unser Verständnis dieser Prozesse verbessern.

Summary

The investigation of star formation history is particularly intriguing in the case of low-mass stars, such as our Sun, due to its direct connection to the history of our own solar system. In low-mass stars, physical and chemical properties are primarily determined by their dense cores. These dense cores originate from localized over-densities within molecular clouds, often found in filamentary structures in the interstellar medium (ISM). As a result, the study of star formation is intrinsically tied to investigating molecular clouds and their filamentary structures. Filaments, elongated structures within the ISM, are pivotal to the star formation process. Observational studies have consistently highlighted their ubiquity and universal properties, underscoring their role in the formation of dense cores and stars. These structures are shaped by the complex interplay of turbulence, magnetic fields, and gravity. At the intersections of filaments, density is often enhanced, creating hubs associated with the formation of clusters and massive stars. This thesis focuses on understanding the influence of magnetic fields and kinematics on the dynamics and stability of filamentary structures.

The first project examines the protostellar core IRAS15398-3359, a Class 0 young stellar object in its early formation stage. Using molecular line observations of $C^{18}O$ (2–1) and DCO^+ (3–2) with the APEX telescope, I analyzed the kinematic and magnetic properties of the core. The velocity gradient around the protostar revealed material inflow and outflow, suggesting the merging of filamentary structures near the core. Polarization data indicated a strong alignment between the magnetic field and the core's rotation axis, highlighting the magnetic field's regulatory role during collapse.

The second project focuses on an isolated filament east of the Barnard 59 clump in the Pipe Nebula. Near-infrared polarization observations were combined with molecular line data to study the filament's magnetic field structure and stability. The magnetic field strength, estimated using the Davis–Chandrasekhar–Fermi method, indicated support against radial collapse. The filament's radial density profile, modeled using polytropic cylindrical models, suggested that non-thermal motions and magnetic fields play a dominant role in maintaining stability. Additionally, gas flow toward the hub was observed, linking the filament's dynamics to star formation activity in the region.

The final project investigates the Snake filament, a prominent structure with distinct magnetic and kinematic properties. I used optical and near-infrared polarization data, along with molecular line observations of $C^{18}O$ (1–0) and ^{13}CO (1–0), to characterize the filament. Results revealed a predominantly parallel magnetic field orientation in the

lower-density regions, with a significant velocity gradient along the filament's spine. The polarisation efficiency decreases with increasing visual extinction, consistent with reduced grain alignment in denser areas.

These studies demonstrate the critical role of magnetic fields and kinematics in shaping filamentary structures and regulating star formation. Future observations with higher angular resolution and sensitivity will further uncover the complex relationships between filaments, magnetic fields, and star formation, advancing our understanding of this process.

Chapter 1

Introduction

1.1 Molecular clouds and star formation

The interstellar space is not empty, but full of a medium (the ISM), which consists of all matter and energy between stars in a galaxy. The ISM serves as the fuel for star formation and is replenished by material ejected from stars during their life cycles. The ISM is primarily composed of gas, with hydrogen (H) constituting about 70% of its mass, helium (He) about 28%, and the remaining 2% consisting of heavier elements referred to as "metals" by astronomers (Spitzer 1978; Ferrière 2001). These atoms can form molecules under specific physical conditions, with over 300 molecules identified in space so far (McGuire 2022; Ceccarelli et al. 2023).

The ISM exists in several phases, distinguished by their temperature, density, and the predominant form of hydrogen. These phases are the hot ionized medium (HIM), the warm ionized medium (WIM), the warm and cold neutral medium (WNM and CNM), and molecular gas (Ferrière 2001; McKee & Ostriker 1977). The HIM is the hottest and most diffuse phase, with temperatures of $\sim 10^6$ K and densities $n \approx 0.003\,\mathrm{cm}^{-3}$. The WIM and WNM have temperatures of ~ 8000 K and similar densities ($n \approx 0.3\,\mathrm{cm}^{-3}$), but the WIM is ionized while the WNM is neutral (Stahler & Palla 2004). The CNM is denser ($n \sim 50\,\mathrm{cm}^{-3}$) and cooler ($T \sim 100$ K).

1.1.1 Molecular clouds

Molecular clouds are the primary sites of star formation, containing the majority of the molecular hydrogen (H_2) in the galaxy. These clouds are typically shielded from UV radiation by interstellar dust. Molecular clouds are the coldest regions of the ISM, with temperatures ranging from 10 to 20 K. They also exhibit the highest densities compared to other ISM phases, with $n \geq 10^2\,\mathrm{cm}^{-3}$ (Stahler & Palla, 2004).

Giant Molecular Clouds, with typical masses of 10^5–$10^6\,M_\odot$ and sizes of ~ 50 pc, host most of the star-forming activity in the Milky Way (e.g., Orion and Taurus, Heyer & Dame 2015). Smaller molecular clouds, such as Bok globules, contain less mass (~ 2–$50\,M_\odot$) and are often isolated (Stahler & Palla 2004).

Molecular hydrogen (H_2) is the most abundant molecule in molecular clouds, making up the majority of the molecular phase of the ISM. However, due to its non-polar nature, H_2 lacks strong emission lines in the infrared or radio frequencies, making it difficult to detect directly. Instead, carbon monoxide (CO), the second most abundant molecule with an abundance of $X_{\mathrm{CO}} \approx 10^{-4}$ relative to H_2 (e.g., Bolatto et al. 2013), is commonly used as a proxy to study the molecular phase. CO efficiently emits through its rotational transitions in millimeter and submillimeter wavelengths, serving as a key tracer of molecular gas. Additionally, CO is a dominant coolant in molecular clouds, allowing the gas to maintain isothermal conditions during the early stages of gravitational collapse.

Although interstellar dust comprises only about 1% of the total mass of the interstellar medium, its presence is crucial for many astrophysical processes, in particular star and planet formation (Kennicutt & Evans 2012). Dust grains interact with electromagnetic radiation through absorption, scattering, and emission, collectively resulting in the extinction of the background radiation. Shorter wavelengths are more affected by extinction, causing reddening of starlight, such as dust within molecular clouds absorbs background starlight, making these clouds appear as dark patches in optical and near-infrared observations (see Fig. 1.1). The total visual extinction, A_V, caused by dust is often used as a proxy for gas column density, while the dust's re-emission at longer wavelengths is a key tool for characterizing molecular clouds (Stahler & Palla 2004; Kennicutt & Evans 2012).

Molecular clouds represent a critical phase in the star formation process. As the diffuse gas in the ISM condenses and cools, it eventually collapses under gravity to form dense cores and protostars. This process is tightly linked to the physical and chemical structure of the ISM. Understanding the interplay of these structures is crucial for studying star formation across different environments, such as low-mass star-forming regions like Taurus and Ophiuchus clouds (Ortiz-León et al. 2018; Galli et al. 2018), or high-mass star-forming regions like Orion (Kounkel et al. 2017).

1.1.2 Cloud Stability and Fragmentation

Molecular clouds, particularly giant molecular clouds, are critical to the star formation process. Unlike the diffuse atomic phases of the interstellar medium, which are typically in pressure equilibrium, molecular clouds are predominantly governed by gravity. The stability of these clouds can be analyzed using the *virial theorem*, which relates the total energy of a system to its gravitational, thermal, and kinetic energies. In its simplest form, the virial theorem can be expressed as:

$$\frac{1}{2}\frac{d^2I}{dt^2} = 2U + W, \tag{1.1}$$

where I is the moment of inertia, U is the thermal energy, and W is the gravitational energy. For a molecular cloud of mass M, radius R, and temperature T, the gravitational and thermal energy terms are given by:

$$|W| \sim \frac{GM^2}{R}, \tag{1.2}$$

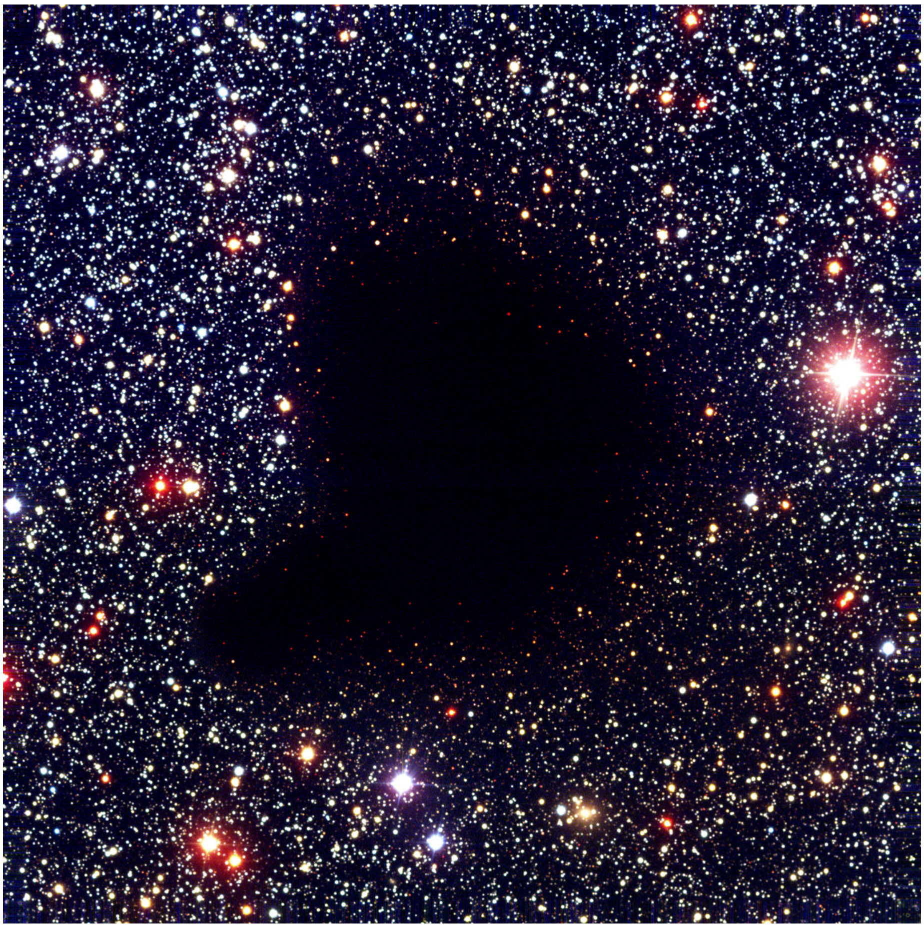

Figure 1.1: The image of the small molecular cloud (Bok globule) Barnard 68 in Pip Nebula, using the 8.2-m Very Large Telescope. This dark cloud appears completely opaque in visible and near-infrared wavelengths due to the obscuring effect of dust particles within its interior, blocking the background starlight. Credit: ESO (https://www.eso.org/public/images/eso0102a/)

$$U \sim \frac{3k_BT}{2\mu m_H}M, \tag{1.3}$$

where G is the gravitational constant, k_B is the Boltzmann constant, m_H is the mass of the hydrogen atom, and μ is the mean molecular weight of the gas. Thermal energy in molecular clouds is generally insufficient to balance gravitational forces. The ratio of thermal to gravitational energy is often much smaller than one, as expressed by:

$$\frac{U}{|W|} \sim \frac{3k_BTR}{2\mu m_H GM} \approx 0.02 \times \left(\frac{T}{20\,\mathrm{K}}\right)\left(\frac{R}{10\,\mathrm{pc}}\right)\left(\frac{M}{10^4 M_\odot}\right)^{-1}. \tag{1.4}$$

For a typical molecular cloud of mass $10^4 M_\odot$, size $\sim$ 10pc and with gas temperature of $\sim$ 20K (Bergin & Tafalla, 2007), we obtain $\frac{U}{|W|} \ll 1$, indicating that gravitational energy dominates thermal energy, and such clouds should collapse under their own gravity. The time required for this collapse is characterized by the free-fall time if thermal energy is relatively negligible in Eq. 1.1:

$$\frac{1}{2}\frac{d^2I}{dt^2} = W \sim -\frac{GM^2}{R}, \tag{1.5}$$

The time required for a pressure-less homogeneous sphere with a density ρ to collapse to a point is given by:

$$t_{\rm ff} \approx \sqrt{\frac{R^3}{GM}} \approx \sqrt{\frac{3\pi}{32G\rho}}, \tag{1.6}$$

For a molecular cloud with the aforementioned dimensions ($10^4 M_\odot$, size $\sim$ 10 pc), the timescale is estimated to be on the order of a few times $\sim 10^6$ yr. Zuckerman & Palmer (1974) pointed out that if molecular clouds were to collapse at free-fall velocity, the star formation rate in the Milky Way would be an order of magnitude higher than the observed rate of approximately $1\,M_\odot$/yr (Robitaille & Whitney, 2010). This suggests that molecular clouds are more stable than would be expected if only thermal motions were responsible for balancing the gravitational potential. Additional factors contributing to cloud stability include kinetic energy (K) from bulk motions such as rotation and turbulence, as well as the magnetic energy ($\mathcal{M}$) stored within the clouds. These mechanisms can be incorporated into the *virial* theorem as (Stahler & Palla, 2004):

$$2U + W + 2K + \mathcal{M} = 0. \tag{1.7}$$

Non-thermal motions, including turbulence, contribute significantly to the overall energy budget of molecular clouds. Observations of CO and its isotopologues reveal that turbulence in molecular clouds is supersonic (Larson, 1981). Additionally, magnetic fields are ubiquitous in the ISM (Soler et al. 2016; Planck Collaboration et al. 2016a) and play a crucial role in stabilizing molecular clouds. Observational studies have shown that magnetic pressure can provide sufficient support to maintain an equilibrium state in molecular clouds, balancing the gravitational pull (Crutcher et al., 2010). The magnetic field properties in the ISM will be presented in more detail in Sect. 1.2

Jean Mass

The Jeans criterion further defines the conditions under which molecular clouds remain stable or collapse. It states that the Jeans mass, which is the maximum mass a spherical cloud of a given density and temperature can have before collapse occurs, and the Jeans length, which represents the corresponding critical size, determine the cloud's stability. This mass can be determined by applying Eq. 1.1 under equilibrium condition, $2U = |W|$. Then we have:

$$\frac{k_B T}{\mu m_H} = \frac{G M_J}{R}. \tag{1.8}$$

Given that the number density is defined as $n = \rho/\mu m_H$, and density is defined as $\rho \propto M/R^3$, the Jeans mass (M_J) and the corresponding Jeans length (λ_J) can be expressed as:

$$M_J \propto T^{\frac{3}{2}} n^{-\frac{1}{2}} \approx 2 M_\odot \left(\frac{T}{10\,\mathrm{K}}\right)^{\frac{3}{2}} \left(\frac{n}{10^3\,\mathrm{cm}^{-3}}\right)^{-\frac{1}{2}}, \tag{1.9}$$

$$\lambda_J \propto \left(\frac{M_J}{\mu m_H n}\right)^{\frac{1}{2}} \approx 0.4\,\mathrm{pc} \left(\frac{T}{10\,\mathrm{K}}\right)^{\frac{1}{2}} \left(\frac{n}{10^3\,\mathrm{cm}^{-3}}\right)^{-\frac{1}{2}}. \tag{1.10}$$

These equations emphasize that lower temperatures promote collapse. As M_J decreases with increasing density, the stable mass threshold becomes smaller, leading to the fragmentation of the cloud into cores. Generally, objects with masses significantly exceeding M_J are considered unstable and likely to undergo fragmentation, forming dense cores. These dense cores, with typical temperatures of $T \leq 10\,\mathrm{K}$ and densities of $n \sim 10^4 - 10^6\,\mathrm{cm}^{-3}$, are the birthplaces of stars and are called *prestellar cores* (Ward-Thompson et al., 1999).

1.1.3 Low-Mass Star Formation

Low-mass star formation (stars with $M_\star < 8\,M_\odot$) occurs in dense cores within molecular clouds. These regions, including prominent star-forming clouds like Ophiuchus and Taurus, provide valuable insights into the formation process due to their proximity and abundance of young stellar objects (YSOs) (Lada, 1987; Andre et al., 2000; Dunham et al., 2014). Studying the formation of low-mass stars is particularly important as it offers clues about the early conditions of our own Solar System. The formation process of low-mass stars is well-categorized into evolutionary stages based on their observational characteristics (Lada, 1987; Andre et al., 1993a, 2000; Dunham et al., 2014). These stages are traditionally defined by the spectral energy distribution (SED) of the protostar across optical, infrared, and submillimeter wavelengths. The stages are classified into four main categories—Class 0, Class I, Class II, and Class III—each corresponding to a specific phase in the protostar's evolution (Chen et al., 1995; Andre et al., 1993a; Dunham et al., 2014). Figure 1.2 illustrates the various stages of protostellar collapse leading to the formation of a star with a planetary system, with each step labeled according to its corresponding class. In the Class 0 phase, the protostar is deeply embedded in a dense envelope, with significant accretion from the envelope onto the young stellar object. The protostar irradiation is re-emits in the far infrared, dominating the SED ($T_{\mathrm{bol}} < 70\,\mathrm{K}$). As accretion continues and the envelope starts to dissipate, the emission from the protostar and its surrounding disk is less obscured, and more emission is observed at mid and near-infrared wavelengths. This marks the Class I phase, where the SED shows the light that has contributions from the star, disk, and remaining envelope ($70\,\mathrm{K} < T_{\mathrm{bol}} < 650\,\mathrm{K}$). By the Class II stage, the envelope is fully cleared, leaving the protoplanetary disk as the primary source of infrared excess in the SED. The protostar, now visible in optical wavelengths, is identified as a classical T-Tauri star ($650\,\mathrm{K} < T_{\mathrm{bol}}$[1] $< 2800\,\mathrm{K}$). Finally, in the Class III phase, the disk

[1] T_{bol} is the temperature of a black body that has the same mean frequency as the observed SED.

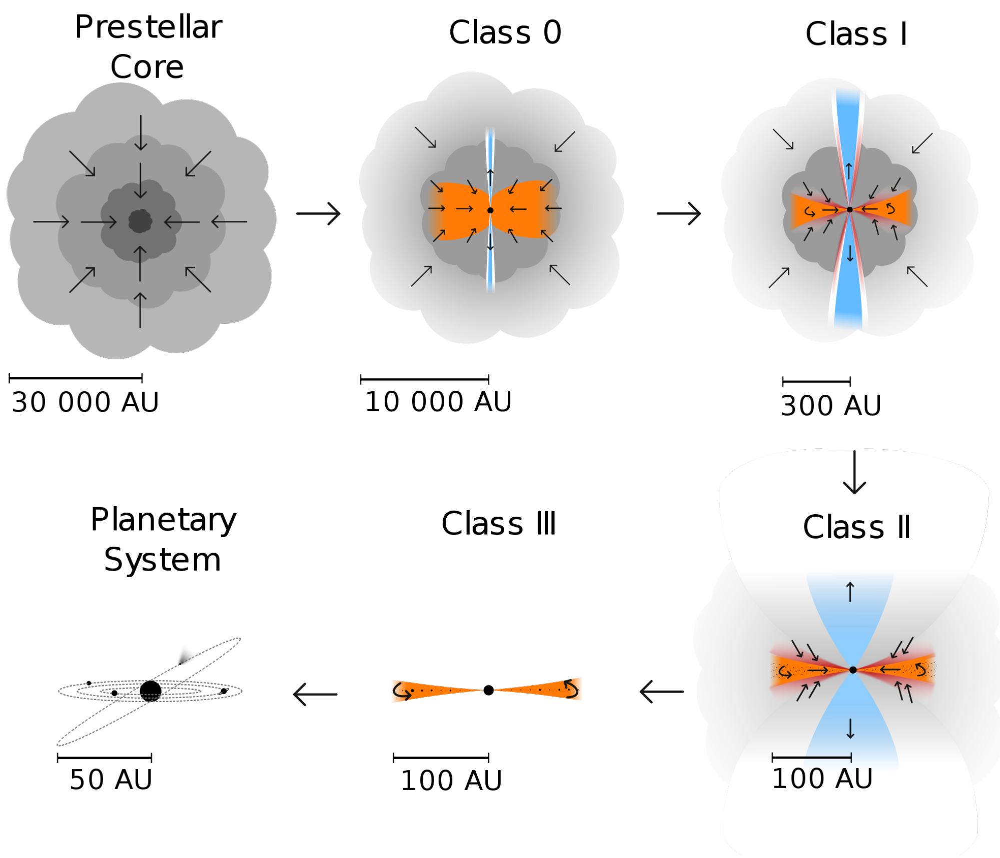

Figure 1.2: A diagram depicting the stages of protostar evolution and planetary system, along with their respective observational classifications. The gray regions indicate the envelope material, the orange areas represent the protostellar disk, and the blue regions highlight the bipolar outflows. Credit: Persson, Magnus Vilhelm (2014). https://doi.org/10.6084/m9.figshare.654555.v7

is nearly cleared, producing only weak infrared emission. The star, now a weak T-Tauri star, no longer accretes significant material (Greene et al., 1994).

1.1.4 Filamentary structure of clouds

A "filament" is considered an elongated structure in the ISM (André et al., 2014). The large molecular clouds are usually organized in filamentary structures from large (several pc) to small scales (a few 0.1 pc), and most dense cores are located within these filamentary structures. Results from Galactic imaging surveys accomplished with the *Herschel* Space Observatory (Pilbratt et al., 2010) between late 2009 and 2013 show that such filaments are ubiquitous in the cold ISM, exhibit a high degree of universality in their properties, and likely play a crucial role in the star formation process (André et al., 2014). The existence of parsec-scale filamentary structures in nearby interstellar clouds and their potential sig-

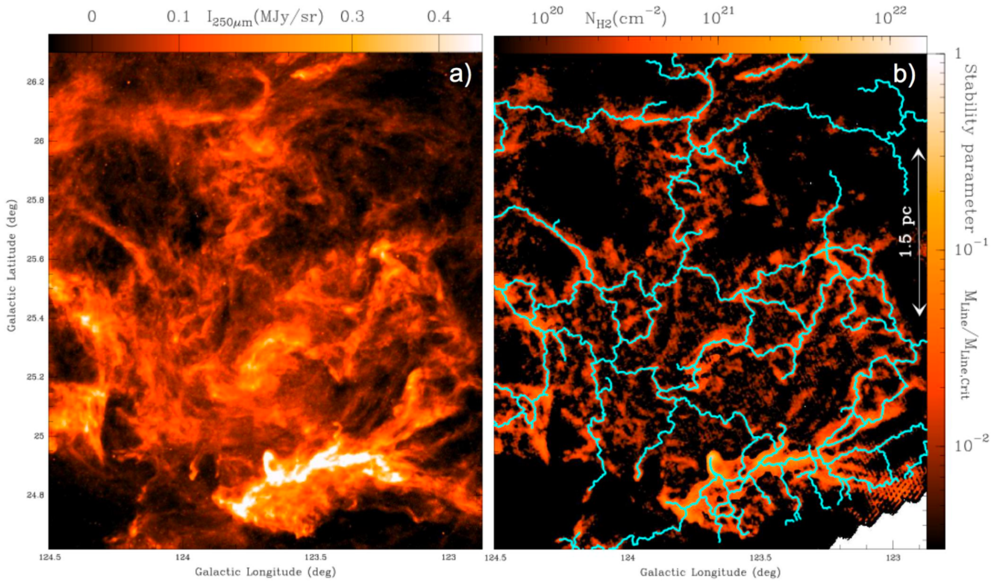

Figure 1.3: (a) Herschel/SPIRE 250 μm dust continuum map of a part of the Polaris Flare translucent cloud. (b) Column density map from Herschel data. The skeleton of the filament network is shown in light blue. Based on the typical filament width of $\sim$ 0.1 pc (Arzoumanian et al., 2011), the column density map represents mass per unit length along the filaments, color scale on the right. Credit: André et al. (2014)

nificance for star formation have been highlighted by numerous authors over the past three decades. For instance, Schneider & Elmegreen (1979) analyzed the properties of 23 elongated dark nebulae observed on optical plates, which exhibited significant condensations or internal globules. They referred to these structures as “globular filaments”. High-angular-resolution observations of HI in the Riegel-Crutcher cloud by McClure-Griffiths et al. (2006) revealed an intricate network of aligned HI filaments. The filaments that were observed in HI self-absorption by McClure-Griffiths et al. (2006) had an insufficient column density, $A_V < 0.5$ mag, to shield CO from photodissociation. These HI filaments tend to be aligned with the ambient magnetic field, indicating a magnetic dominance in their structure (McClure-Griffiths et al. 2006). The presence of filamentary structures is ubiquitous in every cloud observed by *Herschel*, regardless of their star-forming scope (see Molinari et al., 2010). For instance, Fig. 1.3(a) presents the 250 μm continuum emission map of the Polaris Flare, which is a non-star-forming cloud (Ward-Thompson et al. 2010; Miville-Deschênes et al. 2010). Figure 1.3(b) displays a column density map of the same cloud, derived from *Herschel* data and filtered to highlight the filamentary structures (Bontemps et al. 2010). In both panels, filaments are clearly visible throughout the cloud, even though no star formation is present. This widespread filamentary structure suggests that filament formation occurs prior to star formation in the cold ISM and is linked to internal processes within the clouds (André et al. 2014).

The organization of filaments varies across clouds. In Vela C, Hill et al. (2011) iden-

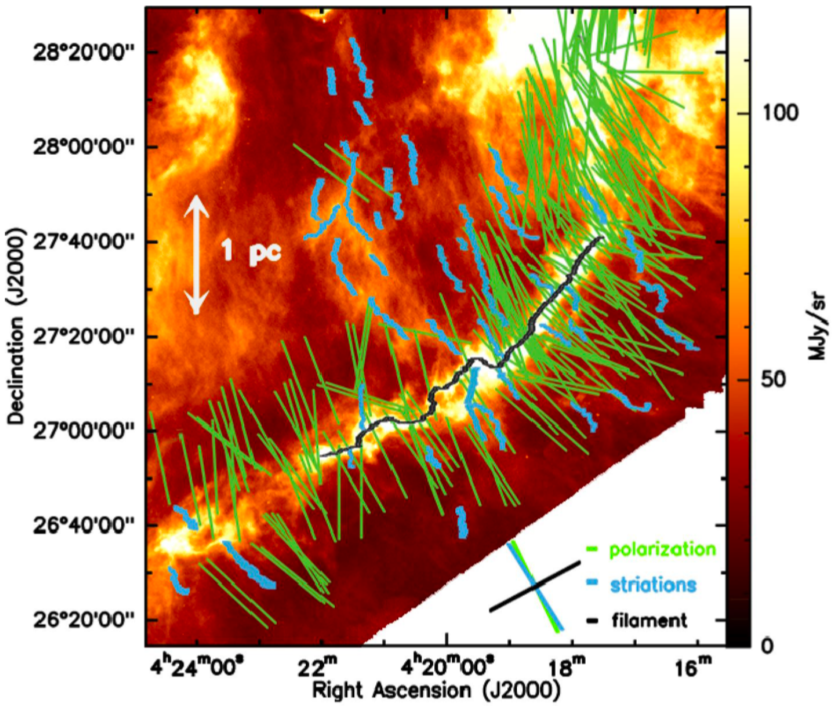

Figure 1.4: Optical and infrared polarization vectors, tracing the magnetic field orientation, overlaid on the Herschel/SPIRE 250 μm image of the B211/B213 filaments region in Taurus. The plane-of-the-sky projection of the magnetic field is perpendicular to the B211/B213 filament and roughly aligned with the direction of the blue striations. Credit: André et al. (2014)

tified disorganized filaments in the low-column density "nests" dominated by turbulence and more unidirectional filaments in the high-column density "ridges," where gravity plays a dominant role. Similar patterns are observed in other regions, such as filaments in the low-density Polaris Flare (Fig. 1.3; André et al., 2014), which are turbulence-dominated, and also the dense, self-gravitating B211/B213 filament in Taurus (Fig. 1.4; Palmeirim et al., 2013a; André et al., 2014). Observations further indicate that dense filaments tend to align perpendicular to the local magnetic field, while low-density filaments are typically parallel to the local magnetic field (Fig. 1.4; Peretto et al. 2012; Goodman et al. 1990; Palmeirim et al. 2013a; André et al. 2014). Moreover, *Herschel* observations establish a clear connection between filamentary structures and the formation of cold, dense cores (Könyves et al. 2010; Men'shchikov et al. 2010; Polychroni et al. 2013). Filament intersections are particularly significant, as they create regions of higher column density at the points of convergence, further enhancing star formation. Such intersections have been identified as preferred environments for massive star and cluster formation (Myers, 2009, 2011). For instance, Peretto et al. (2012) revealed the “hub-filament” structure (see also Myers, 2009) formed by merging filaments within the Barnard 59 (B59) core of the

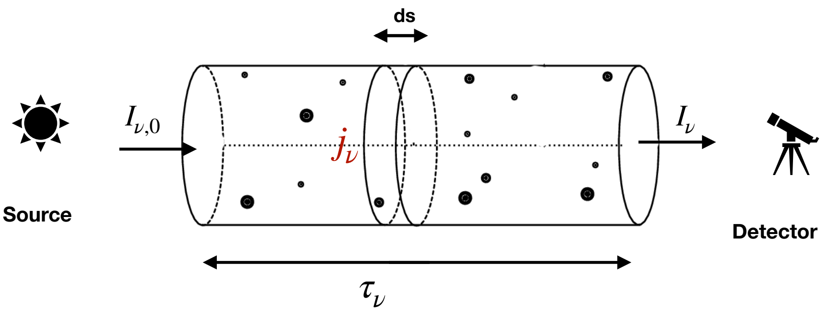

Figure 1.5: Schematic view of the radiation passing through a slab of gas. As photons traverse an infinitesimally thin slab of width ds, the slab absorbs the background radiation $I_{\nu,0}$ and emits radiation according to its emissivity j_ν.

Pipe Nebula. While the Pipe Nebula is largely quiescent in terms of star formation, B59 is an exception, where star formation is likely enabled by the increased local density (and gravitational dominance) resulting from filament intersections. Additionally, the merging of filaments may play a role in the formation of higher-mass stars. Merging structures are often dominated by a single massive filament fed by smaller, neighboring sub-filaments (see Hill et al. 2011; Hennemann et al. 2012).

Filaments play a crucial role in the formation of prestellar cores (Könyves et al., 2010), supporting a scenario that can be explained in two main steps. First, the dissipation of kinetic energy in large-scale MHD flows, whether turbulent or not, appears to generate filaments approximately $\sim$ 0.1 pc in width within the ISM (Arzoumanian et al., 2011). Second, the densest filaments fragment into prestellar cores through gravitational instability, provided the mass per unit length exceeds the critical value of $M_{\rm line,crit} \approx 16\,M_\odot\,{\rm pc}^{-1}$. This corresponds to a critical column density threshold of $\Sigma_{\rm gas}^{\rm crit} \sim 160\,M_\odot\,{\rm pc}^{-2}$ ($A_V^{\rm crit} \sim 8$ mag) or a critical volume density of $n_{\rm H_2}^{\rm crit} \sim 2 \times 10^4\,{\rm cm}^{-3}$ (see also Bontemps et al., 2010; André et al., 2014). In contrast to the standard gravo-turbulent fragmentation model (e.g., Mac Low & Klessen, 2004a), where filaments are present but do not play a fundamental role, the André et al. (2014) model focuses on filamentary geometry as an essential component. This includes features such as the existence of a critical mass per unit length for nearly isothermal filaments.

1.1.5 Radiative processes

The gas in the ISM, including molecular clouds and filamentary structure, is continuously heated by energetic cosmic ray particles, the interstellar radiation field. In molecular clouds, this energy is dissipated primarily through two radiative processes: (i) blackbody radiation emitted by dust particles, and (ii) spectral line emission from atoms and molecules. These emissions are not only crucial for cooling the gas but are also the primary tools astronomers use to observe and study molecular clouds. Both forms of emission provide invaluable information about the physical and chemical conditions of star-forming environments, enabling the development of physical models to explain the observed phenomena. The following subsections detail these processes and the associated mechanisms, and they are mainly based on Stahler & Palla (2004).

Radiative transfer

The radiative transfer equation is fundamental in understanding how radiation propagates through a medium, such as interstellar material consisting of gas and dust. This equation describes the changes in the intensity of radiation I_ν as it travels through a thin slab of material of infinitesimal width ds, see Fig. 1.5. The interaction of radiation with the medium, through absorption and emission processes, is described by the radiative transfer equation:

$$\frac{dI_\nu}{ds} = -\rho\kappa_\nu I_\nu + j_\nu, \tag{1.11}$$

where ρ is the density of the material, κ_ν is the absorption coefficient, which depends on the material properties and the frequency of the radiation ν, j_ν is the emissivity, representing the energy emitted per unit time, volume, frequency, and solid angle. This equation indicates that radiation can be absorbed by the material (first term) or emitted by it (second term), modifying the intensity I_ν as the ray traverses through the medium. The optical depth τ_ν characterizes the absorption and re-emission of radiation by dust grains along the line of sight and is defined as:

$$\tau_\nu = \int \rho\kappa_\nu \, ds, \tag{1.12}$$

where ρ is the gas density. The source function, denoted as S_ν, is a characteristic property of the medium and expressed as: $S_\nu = \frac{j_\nu}{\kappa_\nu}$.

Integrating Eq. 1.11 along the optical depth τ_ν, with some little algebra, we obtain the emergent radiation flux:

$$I_\nu = I_{\nu,0}e^{-\tau_\nu} + \int_0^{\tau_\nu} S_\nu(\tau'_\nu)e^{-(\tau_\nu-\tau'_\nu)}d\tau'_\nu. \tag{1.13}$$

In the case of black-body radiation, the source function S_ν is equivalent to the Planck function $B_\nu(T)$ (Rybicki & Lightman, 1985), given by:

$$B_\nu(T) = \frac{2h\nu^3}{c^2}\frac{1}{e^{h\nu/k_BT} - 1}, \tag{1.14}$$

where h is Planck's constant, ν is the frequency, c is the speed of light, k_B is Boltzmann's constant, and T is the temperature. Thus, when the source function is the black-body radiation and temperature T, Eq. 1.13 becomes:

$$I_\nu = I_\nu(0)e^{-\tau_\nu} + B_\nu(T)\left[1 - e^{-\tau_\nu}\right], \tag{1.15}$$

Assuming the background intensity $I_{\nu,0}$ is the cosmic microwave background (CMB) at a temperature of $T_{\rm bg} = 2.73\,{\rm K}$, the difference between observed and background intensity is given by:

$$\Delta I_\nu = I_\nu - I_{\nu,0} = [B_\nu(T) - B_\nu(T_{\rm bg})] \left(1 - e^{-\tau_\nu}\right). \tag{1.16}$$

This difference is often expressed in terms of the *brightness temperature* T_B, defined as:

$$T_B = \frac{c^2}{2k_B\nu^2}\Delta I_\nu. \tag{1.17}$$

The brightness temperature T_B represents the temperature a blackbody would have to emit the same intensity as observed radiation, ΔI_ν. Substituting this definition into the Eq. 1.16, we have the *detection equation*:

$$T_B = [J_\nu(T) - J_\nu(T_b)] \left(1 - e^{-\tau_\nu}\right), \tag{1.18}$$

where $J_\nu(T)$ is defined as:

$$J_\nu(T) = \frac{h\nu}{k_B}\frac{1}{e^{h\nu/k_BT} - 1}. \tag{1.19}$$

The solution to the radiative transfer equation, expressed in terms of this observable, can be written as:

$$\frac{T_B}{f} = [J_\nu(T) - J_\nu(T_{\rm bg})] \left(1 - e^{-\tau_\nu}\right), \tag{1.20}$$

where f is the filling factor, representing the fraction of the observational beam filled by the emitting source. The filling factor modifies the brightness temperature, such that the true brightness temperature $T_{B,\rm real}$ is related to the observed brightness temperature T_B by $fT_{B,\rm real} = T_B$ (Mangum & Shirley 2015).

Molecular Line Emission and the Two-Level System

Molecular line emission originates from transitions between quantized energy levels of molecules, including rotational, vibrational, and electronic states. These transitions are typically triggered by collisions or radiation. In molecular clouds, the prevailing temperatures are sufficient to excite molecules to higher energy states, particularly within their rotational and vibrational levels. For a two-level system with upper and lower states u and l, the populations are described by the Boltzmann equation:

$$\frac{n_u}{n_l} = \frac{g_u}{g_l}\exp\left(-\frac{\Delta E}{k_BT_{\rm ex}}\right), \tag{1.21}$$

where n_u and n_l are the populations of molecules in the upper (u) and lower (l) energy states, g_u and g_l are the statistical weights of the two states, $\Delta E = h\nu$ is the energy difference, and $T_{\rm ex}$ is the excitation temperature. The emissivity j_ν of the molecular line in Eq. 1.11 is given by:

$$j_\nu = \frac{h\nu}{4\pi}n_uA_{ul}\phi(\nu), \tag{1.22}$$

where A_{ul} is the Einstein coefficient for spontaneous emission, and $\phi(\nu)$ is the line profile function and describes the probability of emission at frequency ν. If the temperature of the medium varies on scales larger than the mean free path of particles, Eq. 1.21 remains valid. This condition is referred to as local thermodynamic equilibrium (LTE). This implies that the transitions occur at a constant temperature, which can be assumed to be equal to the temperature of the gas, i.e., $T_{\rm ex} = T$.

Column Density from Observations

In the previous section, we introduced the concept of the absorption coefficient for a transition, $\alpha_\nu = \rho\kappa_\nu$, in Eq. 1.12. The absorption coefficient arises from two processes: spontaneous absorption and stimulated emission, the latter being regarded as a negative form of absorption. For a two-level system, α_ν can be expressed in terms of the Einstein coefficients $B_{\rm lu}$ and $A_{\rm ul}$ as follows:

$$\alpha_\nu = \frac{h\nu_0}{4\pi} n_l B_{lu} \left(1 - \exp\left(\frac{h\nu_0}{k_B T_{\rm ex}}\right)\right) \phi(\nu) = \frac{h\nu_0}{4\pi} n_u A_{ul} \left(\exp\left(\frac{h\nu_0}{k_B T_{\rm ex}}\right) - 1\right) \phi(\nu), \quad (1.23)$$

and τ_ν becomes:

$$\tau_\nu(s) = \int_{s_0}^{s} \alpha_\nu(s')\, ds'. \quad (1.24)$$

For a two-level system, the column density of molecules in the upper energy level is given by $N_u = \int n_u ds$. Using Eq. 1.23 and integrating over all frequencies ν, we can relate N_u to the optical depth. By rearranging and changing the integration variable to the velocity instead of frequency $dv = cd\nu/\nu$, we obtain:

$$N_u = \frac{8\pi\nu_0^2}{A_{ul}c^3} \left(\exp\left(\frac{h\nu_0}{k_B T_{\rm ex}}\right) - 1\right)^{-1} \int \tau_\nu\, d\nu, \quad (1.25)$$

here, τ_ν represents the optical depth integrated over the frequency ν. The N_u, is connected to the total column density of the molecules, $N_{\rm tot}$, through the rotational partition function, $Q_{\rm rot}$. The partition function accounts for the relative populations of all possible rotational energy states:

$$\frac{N_u}{N_{\rm tot}} = \frac{Q_{\rm rot}}{g_u} \exp\left(-\frac{E_u}{k_B T_{\rm ex}}\right), \quad (1.26)$$

where E_u represents the energy of the upper level relative to the ground state, g_u denotes the degeneracy of the upper state, and $Q_{\rm rot}$ is a characteristic property of the molecule (Mangum & Shirley, 2015). In the case of optically thin emission lines, with identical excitation temperatures $T_{\rm ex}$, the total column density $N_{\rm tot}$ can be directly derived from the observed emission I_ν using the brightness temperature T_B. By applying Eq. 1.20 and defining the integrated intensity as $W = \int T_B(v)dv$, the total column density is expressed as (Caselli et al., 2002b; Mangum & Shirley, 2015):

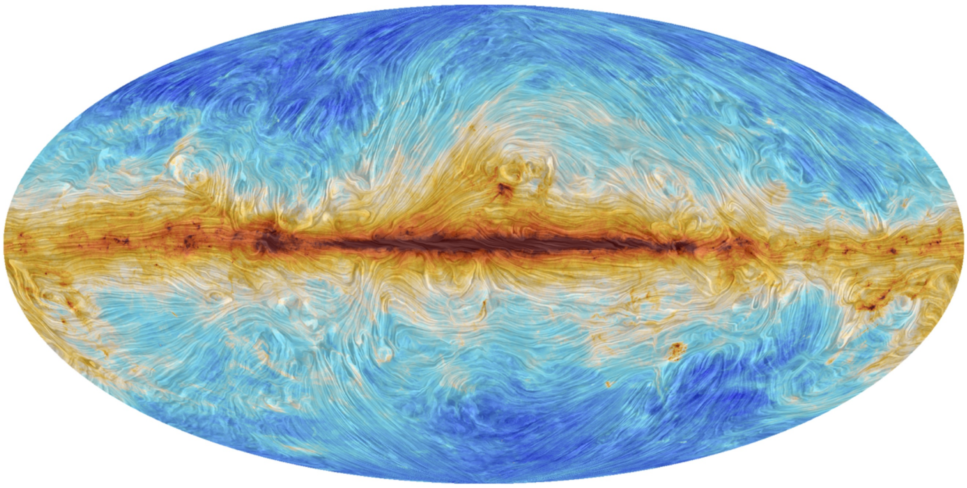

Figure 1.6: An all-sky view of the angle of polarization at 353 GHz, rotated by 90 degree to indicate the direction of the Galactic magnetic field projected on the plane of the sky. The color scale represents total intensity, dominated at this frequency by thermal dust emission (Planck Collaboration et al., 2016d).

$$N_{\rm tot} = \frac{8W\pi\nu^3 Q_{\rm rot}}{fc^3 A_{ul} g_u} \exp\left(\frac{E_u}{k_B T_{\rm ex}}\right)\left(\exp\left(\frac{h\nu_0}{k_B T_{\rm ex}}\right) - 1\right)^{-1} \left(J_\nu(T_{\rm ex}) - J_\nu(T_{\rm bg})\right)^{-1}, \qquad (1.27)$$

where f is the beam-filling factor. This equation allows the determination of the total column density $N_{\rm tot}$ based on spectroscopic parameters such as frequency, Einstein coefficients, and excitation temperature. If the excitation temperature $T_{\rm ex}$ is unknown, which is often the case as it cannot be directly derived, it is typically assumed to be equal to the dust temperature under the assumption that the gas and dust are thermally coupled ($T_{\rm gas} = T_{\rm dust}$). This assumption holds if the coupling is efficient, ensuring that LTE conditions result in $T_{\rm ex} \approx T_{\rm dust}$. However, this approach has significant limitations, as discussed in Chapter 2.

1.2 Interstellar polarization and magnetic fields

Magnetic fields play a crucial role in shaping the structure and dynamics of the interstellar medium (ISM) and regulating star formation processes (Mac Low & Klessen, 2004b; McKee & Ostriker, 2007; Crutcher, 2012a; Hennebelle & André, 2013). Observation of the magnetic fields is vital to the understanding of these processes. The existence of a diffuse Galactic magnetic field was first suggested by the observation of polarized starlight in 1949

(Hall 1949; Hiltner 1949). We now understand that magnetic fields are ubiquitous in the ISM and represent a fundamental component of its energy balance alongside gravity and turbulence. Observations from missions like Planck have shown that molecular clouds are often threaded by ordered magnetic fields (Planck Collaboration et al., 2016d). Planck published the first maps (see Fig. 1.6). These observations show that magnetic fields can efficiently regulate star formation, often competing with or complementing turbulence in driving the dynamics of molecular clouds (Mouschovias & Spitzer, 1976; Nakamura & Li, 2008; Li et al., 2013). Observation made by the Planck Satellite measuring polarization in extinction from background stars and emission from dust revealed the orientation of the magnetic field averaged along the line of sight and projected on the plane of the sky. According to these studies (Planck Collaboration et al. 2016a), regions of higher density, like filaments, have their axis predominately perpendicular to the magnetic field. While regions with lower densities have a magnetic field that appears to be parallel to their axis (see Fig. 1.7).

There are two primary star-formation theories, each differing in how they account for the role of magnetic fields. In strong-field models (Mouschovias, 1991; Mouschovias & Ciolek, 1999), magnetic fields regulate the formation and evolution of molecular clouds, where ambipolar diffusion, a process in which neutral particles drift relative to ions that are tied to magnetic field lines, allows cores to decouple from magnetic support and collapse under gravity to form protostars. These models assume that magnetic pressure is strong enough to counteract gravitational forces until critical conditions are met. Conversely, weak-field models (Padoan & Nordlund, 1999) assume that turbulence dominates cloud and core formation, with magnetic fields providing only a secondary influence. In this scenario, cores either dissipate back into the ISM or collapse to form stars in a free-fall time (Elmegreen, 2000) if they are sufficiently self-gravitating (Mac Low et al., 1998). Magnetic fields not only support clouds against collapse but also play a critical role in removing angular momentum from infalling material, a process known as magnetic braking. This effect is particularly important in the formation of protostars and protoplanetary disks, as it prevents fragmentation and allows the formation of coherent structures (Galli et al., 2006). However, non-ideal magnetohydrodynamic (MHD) effects, such as ambipolar diffusion and the Hall effect, weaken magnetic braking, enabling the formation of larger disks (Mellon & Li, 2008).

Recent advances in polarimetric instrumentation, such as the Planck satellite (Lamarre et al. 2010) and ground-based facilities like the James Clerk Maxwell Telescope (JCMT) with instruments POL-2 and SCUBA-2 (Friberg et al. 2016; Holland et al. 2013) and the Atacama Large Millimeter/submillimeter Array (ALMA, Cortes et al. 2016), have revolutionized our ability to study magnetic fields in the ISM. These instruments have enabled polarization maps that trace the plane-of-sky magnetic field direction over a wide range of densities and scales. Understanding the role of magnetic fields in star formation requires combining observations with theoretical models. MHD simulations have demonstrated the importance of magnetic fields in regulating cloud collapse, launching outflows, and shaping protostellar environments (Tassis & Mouschovias 2005; Galli et al. 2006). Observations of polarized light, combined with molecular spectroscopy to measure turbulence and density,

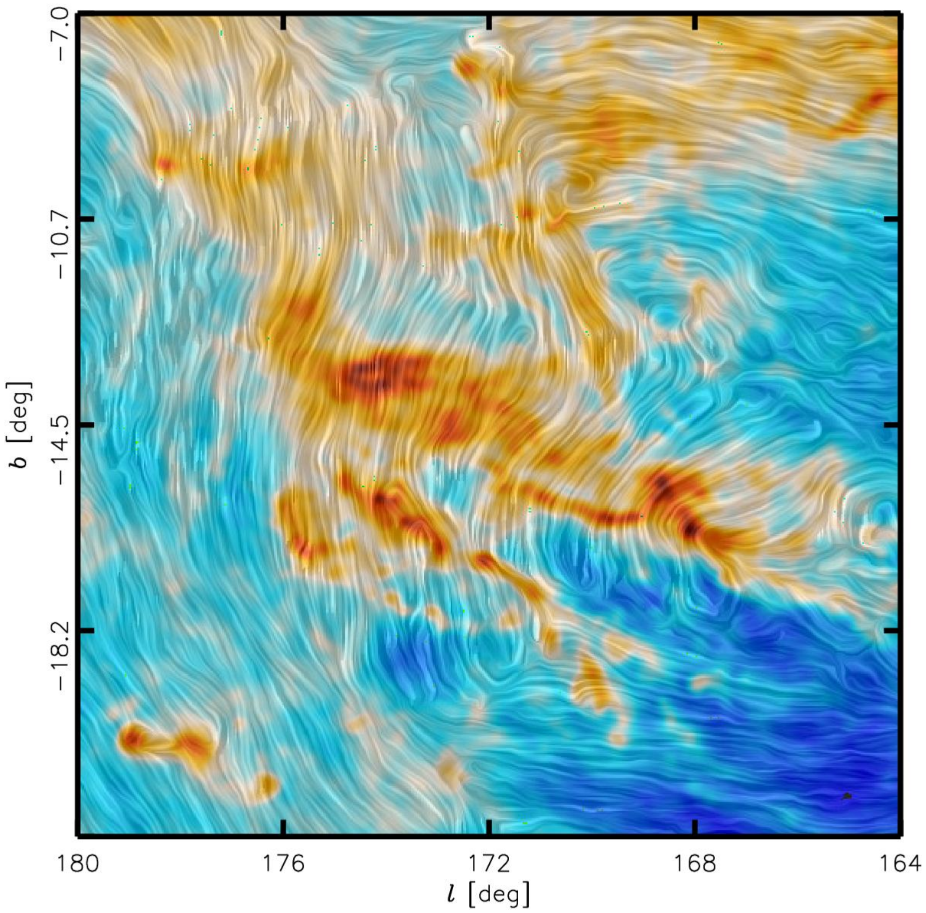

Figure 1.7: The magnetic field and column density toward the Taurus Molecular Cloud, as measured by Planck, are presented (Planck Collaboration et al. 2016a). The color scale represents the column density, while the "drapery" pattern illustrates the orientation of the magnetic field lines, which are perpendicular to the direction of the submillimeter polarization.

provide a comprehensive view of the ISM's magnetic and dynamic properties.

One of the critical parameters to determining the relative importance of magnetic fields in the ISM is the mass-to-flux ratio (M/Φ) (Nakano & Nakamura, 1978), which describes the amount of mass per unit magnetic flux. The critical mass-to-flux ratio is given by (Nakano & Nakamura, 1978):

$$\left(\frac{M}{\Phi}\right)_{\rm crit} = \frac{1}{2\pi\sqrt{G}} \quad \text{(cgs)}, \tag{1.28}$$

where G is the gravitational constant. The observed mass-to-flux ratio is typically expressed in units of the critical value:

$$\lambda = \frac{(M/\Phi)_{\rm obs}}{(M/\Phi)_{\rm crit}} = 2\pi\sqrt{G}\mu m_H \frac{N}{B} \quad \text{(cgs)}, \tag{1.29}$$

where μ is the mean molecular weight, m_H is the hydrogen mass, N is the total hydrogen nuclei column density, and B is the magnetic field strength. A value of $\lambda > 1$ indicates a magnetically supercritical region, where gravity dominates over magnetic pressure, allowing collapse. Conversely, $\lambda < 1$ corresponds to a subcritical state, where magnetic fields can support the region against collapse.

1.2.1 Linear polarimetry

Polarization observations provide a direct approach to studying interstellar magnetic fields. The following section outlines the mathematical framework used to describe polarization emission. Since the primary focus of this thesis is on the polarization caused by interstellar grains, the subsequent discussion expands into the physics of grain alignment within the interstellar medium and the resulting production of polarized light. The Stokes parameters are a set of four parameters that characterize the polarization state of a beam of radiation, which is essentially a superposition of plane waves (via the Fourier transform). The amplitude of the electric field along different basis vectors (perpendicular to the direction of propagation) is given by $\mathbf{e_1} \cdot \mathbf{E}$ and $\mathbf{e_2} \cdot \mathbf{E}$ for linear polarizations along $\mathbf{e_1}$ and $\mathbf{e_2}$. These amplitudes are defined as:

$$E_j = a_j e^{i\delta_j}, \quad E_\pm = a_\pm e^{i\delta_\pm} \tag{1.30}$$

with j= 1,2, then the Stokes parameters are given by:

$$I = |\mathbf{e_1} \cdot \mathbf{E}|^2 + |\mathbf{e_2} \cdot \mathbf{E}|^2 = a_1^2 + a_2^2 \tag{1.31}$$

$$Q = |\mathbf{e_1} \cdot \mathbf{E}|^2 - |\mathbf{e_2} \cdot \mathbf{E}|^2 = a_2^2 - a_1^2 \tag{1.32}$$

$$U = 2\,\mathrm{Re}\left[(\mathbf{e_1} \cdot \mathbf{E})^*(\mathbf{e_2} \cdot \mathbf{E})\right] = 2a_1 a_2 \cos(\delta_2 - \delta_1) \tag{1.33}$$

$$V = 2\,\mathrm{Im}\left[(\mathbf{e_1} \cdot \mathbf{E})^*(\mathbf{e_2} \cdot \mathbf{E})\right] = 2a_1 a_2 \sin(\delta_2 - \delta_1) \tag{1.34}$$

These equations demonstrate that I represents the total intensity of the radiation, independent of the polarization basis. Additionally, U measures linear polarization along axes that are rotated by 45 degrees with respect to e_1 and e_2. It is also straightforward to verify that the total radiation intensity I is related to the other Stokes parameters by:

$$I^2 = Q^2 + U^2 + V^2 \tag{1.35}$$

When circular polarization is absent (i.e., $V = 0$), which is often a reasonable assumption, the polarized component of the electric field can be expressed as:

$$\mathbf{E_p}(x,t) = E_p\left(\mathbf{e_1}\cos\theta + \mathbf{e_2}\sin\theta\right) e^{i(\mathbf{k}\cdot\mathbf{x} - \omega t)} \tag{1.36}$$

which, using our definitions for the Stokes parameters (see equations 1.32 and 1.33), yields

$$Q = I_p \cos(2\theta) \tag{1.37}$$

$$U = I_p \sin(2\theta) \tag{1.38}$$

with the polarized intensity $I_p = E_p^2$.

Polarization measurements, particularly those of linear polarization, are commonly expressed in terms of the polarization fraction p (also referred to as polarization percentage or level) and the polarization angle θ:

$$p = \frac{\sqrt{Q^2 + U^2}}{I} \tag{1.39}$$

$$\theta = \frac{1}{2} \arctan\left(\frac{U}{Q}\right) \tag{1.40}$$

These two parameters can be conveniently combined to represent a polarization vector, where the length of the vector corresponds to the polarization fraction p, and its orientation is determined by the angle θ, though it does not indicate a direction.

After introducing the Stokes parameters, which describe the polarization state of light, it is essential to explore the primary methods used to observe polarization in the interstellar medium. These include polarization from spectral lines and polarization from dust grains, each offering valuable insights into magnetic field structures. Polarization from spectral lines, through mechanisms like the Zeeman and Goldreich-Kylafis effects, provides a way to probe the magnetic field's interaction with atoms and molecules. However, this thesis focuses primarily on polarization from dust, as it allows for a direct study of magnetic fields by observing the alignment of dust grains within the ISM. While we briefly touch upon other polarization methods, the emphasis will be on dust polarization, which forms the core of the observational analysis presented here.

1.2.2 Polarization from dust

Dust grains in the ISM interact with radiation by scattering and absorbing light while emitting radiation at longer wavelengths. Nearly around 75 years ago, it was discovered that light from background stars becomes linearly polarized due to selective absorption by dust in the foreground (Hall, 1949; Hiltner, 1949). Later studies at far-infrared and millimeter/submillimeter wavelengths revealed that radiation emitted by dust is also linearly polarized but typically at an angle of 90 degrees to the polarization observed in the background starlight at shorter wavelengths.

A population of dust grains can only exhibit a net polarization if its individual grains are aligned by an external factor. In this context, the external magnetic field plays a key role in facilitating this alignment. Nowadays, the prevailing theory for dust grain alignment is the Radiative Alignment Torque (RAT) model, as proposed by Lazarian & Hoang (2007a) (see Fig. 1.8). The key elements of RAT theory can be summarized as follows:

- In the context of RAT theory, the irregular shapes of dust grains result in a finite helicity, which causes them to spin when exposed to an external radiation field.

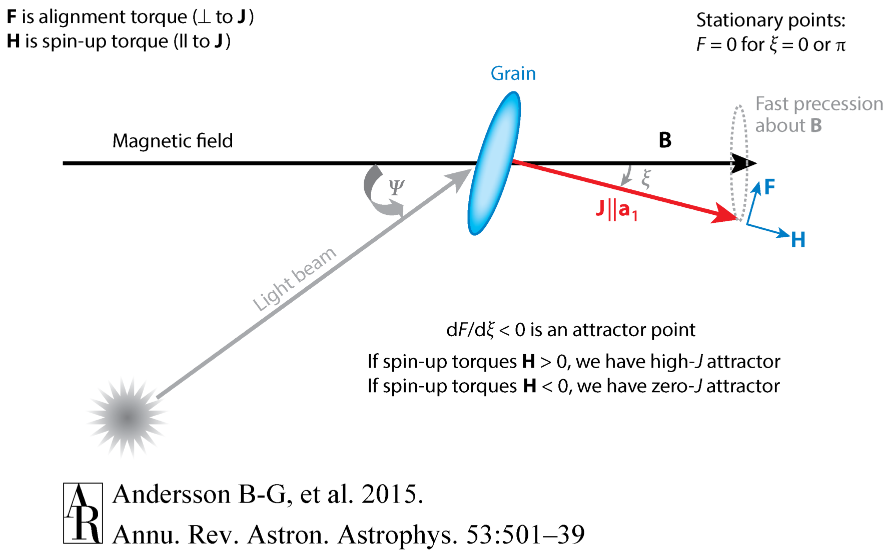

Figure 1.8: The illustration shows how dust grains align under the influence of radiative torques. Within the grain, internal alignment causes its spin axis J to align with the axis of maximum moment of inertia, a_1. The spin axis J then moves around the magnetic field B line at an angle ξ. The incoming radiation (light beam), arriving at an angle relative to B, creates a net torque on the grain, with components along J and perpendicular to it, $J||H$, $F \perp H$. When the spin axis J is parallel to the magnetic field B, the alignment torque F, which changes the angle ξ, disappears. At this point, the grain lies with its long axis perpendicular to B. Diagram from Andersson et al. (2015)

- When a grain begins to spin, it tends to minimize its total energy while conserving angular momentum, leading to rotation around its symmetry axis (the "short" axis with the greatest moment of inertia). This is known as the internal alignment process, made possible by the Barnett effect. In this process, the quantum mechanical unpaired spins in paramagnetic grains realign to compensate for changes in rotational angular momentum.

- As the flipping of spins generates a net magnetization (initially balanced between spins pointing up and down), the grain interacts with the external magnetic field, causing its symmetry axis to procese around it.

- As different areas of the grain's surface are exposed to the external radiation field, the resulting radiative torques act to gradually align the grain's symmetry axis with the external magnetic field.

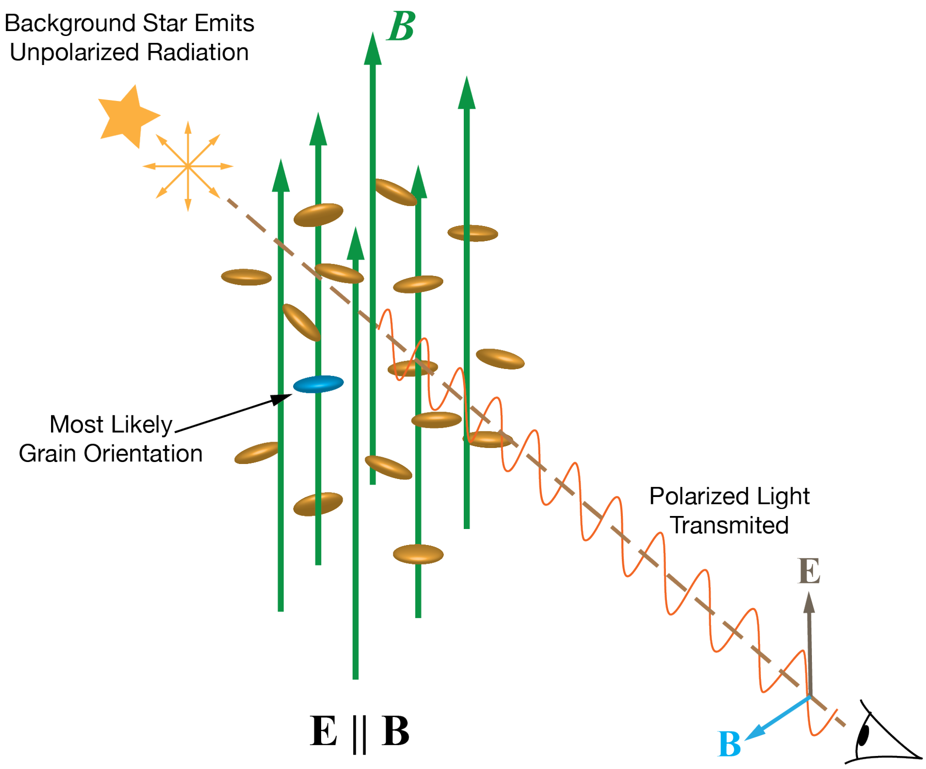

Figure 1.9: Cartoon showing polarized light produced by differential absorption. Unpolarized light from a background star travels through the dense ISM and becomes partially linearly polarized due to the differential absorption of aligned dust grains. Diagram from G. A. Franco

Dust polarization due to differential absorption

A more detailed analysis would still support the conclusion that linear polarization from dust grains reflects the orientation of the magnetic field projected onto the plane of the sky. At shorter wavelengths, such as in the optical range, polarization occurs due to differential absorption, causing the linear polarization to align with the magnetic field. However, at longer wavelengths, like those found in the far-infrared and millimeter/submillimeter ranges, where radiation is emitted by the dust grains themselves, the linear polarization vectors are oriented at a right angle to the direction of the magnetic field. Furthermore, the degree of polarisation does not depend on the strength of the magnetic field.

Initially, light from distant background stars is generally unpolarized. However, as it travels through ISM on its journey to our telescopes, it can become partially linearly polarized. This process, illustrated in Figure 1.9, occurs because the dust grains in the ISM preferentially absorb the component of light polarized along their long axes. Consequently, the scattered light that reaches us is polarized in a direction parallel to the plane-of-the-sky component of the magnetic field, which is responsible for aligning the dust grains. For polarization to be detected, there must be a sufficient amount of dust along the line of

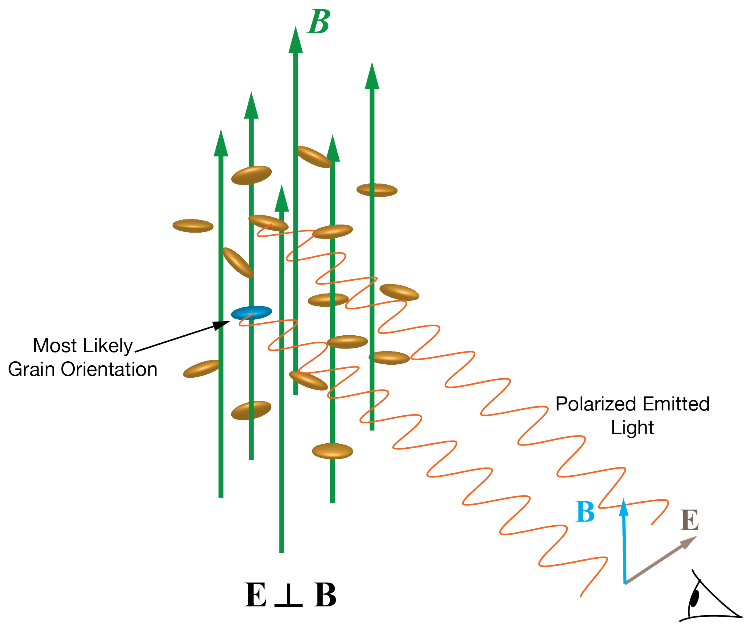

Figure 1.10: Cartoon showing polarized light produced by thermal emission. Dust grains emit photons more efficiently along their longer axis, resulting in an electric field that is partially polarized in that direction. Diagram from G. A. Franco

sight—enough to polarize the radiation but not so dense that it completely absorbs the starlight. Typically, polarization observations at visible and near-infrared wavelengths are limited by visual extinction, with a typical threshold of $A_V < 10$ mag, as higher column densities result in complete absorption of background starlight due to dust extinction. Consequently, only the diffuse gas in molecular clouds and the outer envelopes of dense cores can be probed with these techniques. In regions where visual extinction exceeds a few tens of magnitudes, optical and near-IR background starlight becomes opaque. For these denser regions, dust polarization in emission provides an alternative approach, which will be discussed in detail in the following subsection. This observational technique has long been an essential tool for mapping the plane-pf-sky component of the magnetic fields (e.g. see Goodman et al., 1990; Alves et al., 2008, 2014a).

Dust polarization in emission

When dust grains absorb radiation at shorter wavelengths, they heat up and subsequently re-emit energy at longer wavelengths, such as in the far-infrared and millimeter/sub-millimeter ranges, assuming dust temperature of $9.5K$ (Rathborne et al., 2008). Due to their physical properties, dust grains emit photons more efficiently along their long axes, resulting in a partially polarized electric field in that direction. This polarized signal ends up being aligned perpendicular to the plane-of-the-sky component of the magnetic field, as depicted in Figure 1.10. To infer the magnetic field orientation, we should rotate the observed polarization vectors by 90 degrees.

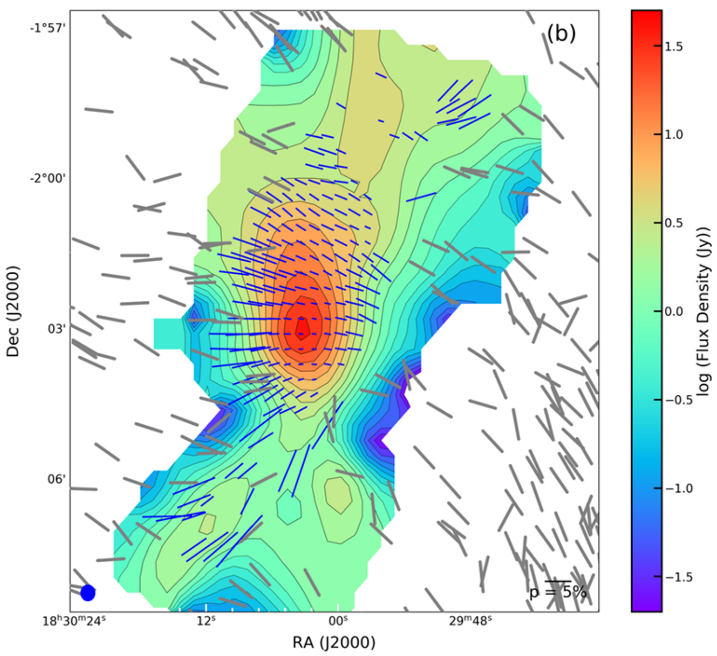

Figure 1.11: The intensity map of Serpens South obtained from HAWC+ is displayed, with gray vectors representing near-infrared polarimetry from SIRPOL and blue vectors indicating polarimetry from HAWC+ at 214 μm (Pillai et al. 2020a). SIRPOL data shows dust polarization due to differential absorption and the HAWC+ shows dust polarization in emission. Both sets of vectors illustrate the orientation of the magnetic field in the plane of the sky.

There is a good agreement between dust polarization measurements at shorter wavelengths, differential absorption, and longer wavelengths, emission (see Fig. 1.11). Both methods effectively reveal the orientation of the magnetic field in the plane of the sky. These measurements are not only consistent but also complementary. Dust emission polarization traces the magnetic field within the inner regions of the source, whereas differential absorption provides a large-scale view of the magnetic field structure (e.g. Alves et al. 2014a; Pillai et al. 2020a).

Magnetic fields detection at radio wavelengths

Magnetic fields can also be studied at radio wavelengths by analyzing their influence on the propagation of electromagnetic waves through plasma. Two important phenomena in polarization studies at these wavelengths are synchrotron radiation and Faraday rotation. Synchrotron radiation occurs when charged particles, such as electrons, are accelerated as they spiral around magnetic field lines, emitting polarized radiation. In contrast, Faraday rotation arises from the interaction of radio waves with a magnetized plasma, causing distinct propagation modes and leading to a measurable rotation of the polarization angle.

We should also note that these two methods provide the line-of-sight component of the magnetic field, in contrast to dust polarization measurements, which reveal the plane-of-sky component of the magnetic field. Together, these processes provide valuable insights into the structure and behavior of magnetic fields in astrophysical environments, complementing observations at other wavelengths.

1.2.3 Polarization from spectral lines

Spectral line polarization arises when the interaction of atoms or molecules with a magnetic field results in polarized radiation, offering a powerful probe of magnetic field structures in the ISM. Two primary mechanisms drive this polarization: the *Zeeman effect* and the *Goldreich-Kylafis effect*.

The *Zeeman effect* occurs when the magnetic dipole interaction splits a spectral line into multiple components in the presence of a magnetic field. This splitting produces π and σ components, where the π component is linearly polarized along the magnetic field direction, and the σ components are circularly or linearly polarized depending on the viewing geometry. The strength of the Zeeman effect depends on the magnetic field and the species of molecule observed. Molecules like CN and OH with unpaired electrons show significant Zeeman sensitivity, making them ideal tracers for measuring the line-of-sight magnetic field strength. The Stokes V parameter, which measures circular polarization, is particularly useful in this context, as it provides direct information about the magnetic field component along the line of sight. However, the weakness of the Zeeman effect in other common molecules, like CO, limits its broader application for mapping magnetic fields. The Zeeman effect is the only technique currently available for directly measuring magnetic field strengths in interstellar clouds (e.g., Crutcher et al. 1993). Zeeman observations in molecular clouds were reviewed and discussed by Crutcher (1999). According to Bourke et al. (2001), 23 additional molecular clouds were observed through the use of the OH Zeeman method, with particular emphasis on the Southern Hemisphere.

When Zeeman sensitivity is low, the *Goldreich-Kylafis effect* becomes critical (Goldreich & Kylafis, 1981; Kylafis, 1983). This effect aligns molecular rotational states with the local magnetic field, leading to linear polarization of rotational molecular transitions, even in cases where the Zeeman effect is too weak to produce observable splitting. The Goldreich-Kylafis effect is especially prominent in environments where the magnetic field influences molecular orientation but does not induce significant Zeeman splitting, such as in CO and other common molecular tracers. By observing the linear polarization of these rotational transitions, the Goldreich-Kylafis effect allows researchers to infer the magnetic field's orientation in the plane of the sky, complementing the information provided by dust polarization studies.

While both the Zeeman and Goldreich-Kylafis effects present unique challenges, particularly due to the often weak polarization signals they generate, they remain crucial tools in the study of magnetic fields in the interstellar medium. These methods, when applicable, provide a detailed picture of the magnetic field structure by probing both the line-of-sight and plane-of-sky components. The Goldreich-Kylafis effect can be used to study magnetic field morphologies in molecular clouds. Linearly polarized molecular lines are particularly useful in regions where dust emission is too faint for polarimetry, as detecting dust emission requires higher total column densities compared to molecular line emission. An example of this method is provided by Greaves et al. (2001), who applied the Goldreich-Kylafis effect to measure the magnetic field direction in the NGC 2024 molecular outflow. Their results indicated that the outflow direction was parallel to the plane-of-sky magnetic field, suggesting that the magnetic field might be channeling the magnetized outflow. This effect is generally very weak and challenging to apply under the density conditions relevant to this thesis, making its detailed discussion beyond the scope of this work.

1.3 Analysis of Polarization Data/Maps

Due to the effects discussed in the previous sections, polarization maps are a way to study magnetic fields in the ISM. This section explains how we analyze these maps in the infrared, optical, and submillimeter regimes, starting with the classical Davis-Chandrasekhar-Fermi (DCF) method, which estimates the strength of magnetic fields. I will also describe the updates to the DCF method and other approaches, like the Hildebrand and Houde (HH09) model. Finally, we discuss some of the challenges with these methodes.

1.3.1 Classical Davis-Chandrasekhar-Fermi method

Polarization maps are crucial tools for investigating the structure of magnetic fields in the ISM, particularly in star-forming regions. One of the primary techniques employed in this analysis is the Davis-Chandrasekhar-Fermi method (Davis 1951; Chandrasekhar & Fermi 1953). This method estimates the strength of the magnetic field in the plane of the sky, (B_{POS}), by utilizing the dispersion in polarization angles (1.40) obtained from dust emission or extinction measurements. The dispersion serves as an indicator of how non-thermal gas motions distort the magnetic field. The DCF method operates under several key assumptions that simplify the complexity of the magnetic field structure. It models the magnetic field as a combination of two vector components:

$$\mathbf{B} = \mathbf{B}_0 + \mathbf{B}_t, \tag{1.41}$$

where $\mathbf{B}_0$ represents the uniform large-scale (or average) magnetic field and $\mathbf{B}_t$ represents the turbulent (or random) field. The DCF method assumes that the magnetic field is frozen into the gas, and that the gas and field lines oscillate in phase. Turbulent gas motions perturb the field lines, inducing small-amplitude fluctuations, B_t, around the mean magnetic field in the form of Alfvén waves. A key assumption is that the turbulent component is weak compared to the ordered field, $\mathbf{B}_t \ll \mathbf{B}_0$. Furthermore, the method assumes $\mathbf{B}_0 \cdot \mathbf{B}_t = 0$, as Alfvén waves are transverse in nature. Finally, it is assumed that an equilibrium exists between the turbulent kinetic energy and the magnetic energy,

$$\frac{\rho v_t^2}{2} = \frac{B_t^2}{8\pi}, \tag{1.42}$$

where δv represents the turbulent velocity dispersion. This quantity can be measured from the turbulent component of the linewidth of a gas species that traces the same material as the dust polarization observations. The turbulent velocity dispersion is given by:

$$\delta v = \left(\frac{B_t}{B_0}\right)\left(\frac{B_0}{\sqrt{4\pi\rho}}\right). \tag{1.43}$$

By further assuming that the dispersion in the polarization angles is linked to the ratio of the turbulent-to-ordered field strength, B_{t}/B_0, the DCF equation for the B-field strength on the plane of the sky can be expressed as:

$$B_0 = \sqrt{4\pi\rho}\frac{\delta v}{\Delta\theta}, \tag{1.44}$$

where ρ represents the gas density and $\Delta\theta$ is the dispersion of polarization angles.

1.3.2 Hildebrand and Houde method

Hildebrand et al. (2009) and Houde et al. (2009), hereafter HH09, proposed an analytical model for polarization data to measure the turbulence-induced spread in the presence of external magnetic field bending. This method is based on the DCF approach but introduces a new technique for evaluating the observed polarization angles. HH09 introduces an alternative approach to measure the ratio $\frac{B_t}{B_0}$. This technique is based on the structure function of the polarization angles, which quantifies how the polarization angle varies over different spatial scales. Specifically, the relevant quantity is the polarization angle difference between two points separated by a distance ℓ, $\Delta\Phi(\ell) \equiv \Phi(\mathbf{x}) - \Phi(\mathbf{x}+\ell)$. By taking the average over a polarization map for a separation ℓ, one obtains:

$$1 - \langle\cos[\Delta\Phi(\ell)]\rangle \simeq \frac{1}{2}\left\langle(\Delta\Phi(\ell))^2\right\rangle, \tag{1.45}$$

which is valid for small $\Delta\Phi << 1$. The right-hand side of the equation is the second-order structure function of the polarization angle. The telescope beam and autocorrelation function of the turbulence can be modeled by a Gaussian function with widths W and δ. The equation will reduce to (for more details check Houde et al. 2009):

$$1 - \langle\cos[\Delta\Phi(\ell)]\rangle = \sqrt{2\pi}\left(\frac{B_t}{B_0}\right)^2 \delta^3 \frac{(\delta^2 + 2W^2)\,\Delta'}{\sqrt{2\pi}\delta^3}\left[1 - e^{-\frac{\ell^2}{2(\delta^2+2W^2)}}\right] + m^2\ell^2, \tag{1.46}$$

where m is a constant related to the large-scale structure of the magnetic field, Δ' is the effective cloud depth. This relationship only applies to spatial scales $\delta \leq \ell \leq d$, where δ represents the correlation length of the turbulent B-field (B_t), and d represents the highest distance at which B_0 remains uniform. Equation 1.46 is used to estimate the $\Delta\theta = B_t/B_0$ term, which is then inserted into the DCF formula 1.44 to obtain B on the plane of the sky:

$$B_{\text{pos}} = \sqrt{4\pi\mu_{H_2} m_H n_{H_2}} \frac{\delta v}{\Delta\theta}, \tag{1.47}$$

where m_{H} is the hydrogen mass, $\mu_{\mathrm{H_2}}$ is the gas mean molecular weight per hydrogen molecule, and $n_{\mathrm{H_2}}$ is the gas volume density.

1.3.3 Caveats of the method and alternatives

The DCF method relies on several key assumptions, including that turbulence is Alfvénic, nonthermal velocity dispersion traces turbulent motions, and the mean magnetic field is uniform. However, the ISM is highly compressible (Heiles & Troland, 2003), which means that δv includes contributions from both Alfvénic and compressible modes. Consequently, δv will always be higher than it would be if only Alfvén waves were present. To apply the DCF method accurately, mode decomposition is required. Nevertheless, performing mode decomposition on observational data is highly challenging and not straightforward. Various modifications to the DCF method have been proposed, beyond the one from HH09 discussed in the previous subsection (e.g., Ostriker et al. 2001; Cho & Yoo 2016; Lazarian et al. 2020; Skalidis & Tassis 2021). In general, it has been suggested that the original DCF method overestimates magnetic field strength (Pattle et al. 2022a; Ostriker et al. 2001; Pattle & Fissel 2019; and Skalidis & Tassis 2021 for a thorough comparison).

Recent advancements in the application of the Davis-Chandrasekhar-Fermi method have resulted in renewed interest in testing various DCF modifications against theoretical simulations. To show the differences, we used one of the modification methods suggested by Skalidis & Tassis (2021). Skalidis & Tassis (2021) introduced an alternative DCF equation that emphasizes the dominance of non-Alfvénic (compressible) modes over Alfvénic (incompressible) modes, Following their methodology, the equation for the B-feild strength becomes:

$$B_{POS} = \sqrt{2\pi\rho} \frac{\delta v}{\sqrt{\Delta\theta}}, \tag{1.48}$$

and validated this approach using a range of ideal magnetohydrodynamic (MHD) simulations. In contrast, Li et al. (2022) argued that although compressible modes have a significant impact, the effects of compression and rarefaction largely cancel each other out. They suggest a derivation that supports modifying the classical DCF equation by replacing $\Delta\theta$ with $\tan\Delta\theta$ in the equation 1.44. This adjustment effectively removes the limitations caused by the small-angle approximations traditionally linked with the DCF method (Heitsch et al. 2001, Falceta-Gonçalves et al. 2008). Such modifications enhance the robustness of magnetic field strength estimates derived from polarization data.

1.4 Observations of star-forming region

Observations presented in this thesis were conducted using two types of telescopes: radio telescopes and optical telescopes. For the purposes of this study, radio telescopes were utilized to observe spectral lines, taking advantage of their sensitivity to millimeter and submillimeter wavelengths. Optical telescopes, on the other hand, were employed to obtain polarization data essential for this work. Each type of telescope operates within distinct transparent windows of the atmosphere in their respective wavelength regimes, allowing photons to pass through (see Fig. 1.12). Fortunately, the atmosphere provides transparency windows in the millimeter/submillimeter and visible wavelength ranges, enabling observations in these regions. For polarization data, all observations were conducted at the Pico dos Dias Observatory (OPD), located in southern Minas Gerais, Brazil, at an altitude of 1864 meters. The OPD is operated by the Brazilian National Laboratory of Astrophysics (LNA). The 1.60-m Perkin-Elmer telescope is the primary instrument, used extensively for photometry, polarimetry, direct imaging, and spectroscopy. For molecular line data, observations were obtained from several radio telescopes, including the Atacama Pathfinder EXperiment (APEX) single-dish antenna in Chile, the James Clerk Maxwell Telescope (JCMT), and the 30m telescope at Pico Veleta in Spain, operated by IRAM. The following sections describe in detail how molecular line and polarization data were acquired using these different types of telescopes.

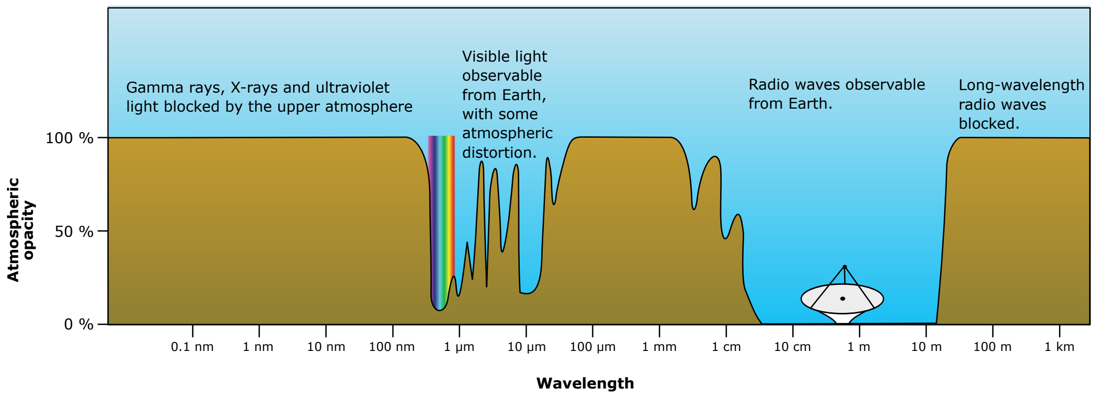

Figure 1.12: The atmospheric opacity as a function of wavelength, with the corresponding spectral bands marked. Credit: NASA.

1.4.1 Single-dish telescopes

Single-dish telescopes have been used to measure spectroscopic lines used in this thesis. Spectral line observations allow us to trace the distribution, dynamics, and physical conditions of molecular gas, which are crucial for understanding the processes governing star formation. Such studies require specialized instruments capable of detecting the faint radiation emitted at millimeter and submillimeter wavelengths. Single-dish telescopes are equipped with a large parabolic reflector that gathers incoming radiation. In most cases, a secondary mirror, known as a subreflector, redirects the collected wavefront to the secondary focus, where the receivers are positioned. One of the most prominent characteristics

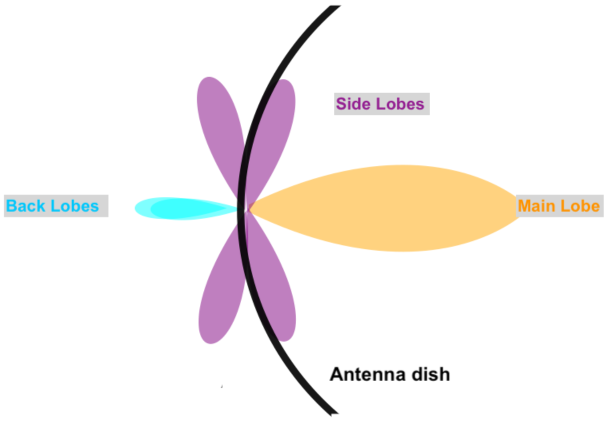

Figure 1.13: Diagram of antenna beam pattern for a single dish telescope.

of a dish telescope is its beam pattern in the sky, which is composed of a main lobe and several side lobes, and represents the directional receiving power of the telescope. A main lobe refers to the solid angle where the telescope responds the most (see Fig. 1.13). The angular resolution of a single-dish telescope is determined by its beam width, $\theta_{\rm MB}$:

$$\theta_{\rm MB} \approx \frac{\lambda}{D}, \tag{1.49}$$

where λ is the wavelength, and D is the diameter of the dish. The total power received by the telescope, P, is expressed in terms of the system temperature, $T_{\rm sys}$, equal to the Rayleigh-Jeans temperature of the object that is emitting that power (Thompson et al., 2017):

$$P = k_B T_{\rm sys} G_\nu \Delta\nu, \tag{1.50}$$

where G_ν is the antenna gain, and $\Delta\nu$ is the bandwidth of the observation. The systemic temperature $T_{\rm sys}$ has contributions from different sources, giving:

$$T_{\rm sys} = T_{\rm A} + T_{\rm Rx}, \tag{1.51}$$

where $T_{\rm A}$ represents the antenna temperature contributed by the astronomical source of interest, while $T_{\rm Rx}$ denotes the receiver temperature, which accounts for contributions from the background sources, receiver noise, and Earth's atmosphere. $T_{\rm Rx}$ is determined based on the properties of the receivers and the atmospheric conditions at the time of observation. Based on the radiometer equation, this noise can be calculated (Wilson et al., 2009):

$$\sigma = k\frac{T_{\rm sys}}{\sqrt{\Delta\nu\tau}}, \tag{1.52}$$

where k is a constant that depends on the observing mode, $\Delta\nu$ represents the frequency bandwidth, and τ denotes the integration time. The antenna temperature, $T_{\rm A}$, is linked to the source brightness temperature, T_{B}. After correcting the antenna temperature for atmospheric absorption, quantified by the atmospheric opacity τ_{atm}, the corrected antenna temperature is given by:

$$T'_A = T_A e^{-\tau_{\mathrm{atm}}}. \tag{1.53}$$

The main-beam temperature, T_{MB}, which is the power coming from the main lobe, is then calculated as:

$$T_{\mathrm{MB}} = \frac{T'_A}{\eta_{\mathrm{MB}}}, \tag{1.54}$$

where η_{MB} is the main beam efficiency. This parameter measures the fraction of power concentrated in the main lobe of the beam. When the angular size of the source is comparable to the beam resolution, $T_{\mathrm{MB}} \sim T_{\mathrm{B}}$, meaning the main-beam temperature scale is the same as the source brightness temperature in ideal condition. If this is not the case, one has to take into account the beam-filling factor of the source.

Two observational modes are commonly employed: single-pointing and mapping. Single-pointing observations measure the flux from a specific source position, while mapping involves scanning the telescope across a region to produce a data cube with spatial and spectral dimensions. The on-the-fly (OTF) mapping technique, for instance, allows efficient coverage of large areas by continuously moving the telescope while recording data.

1.4.2 Polarimeters utilized at OPD

In this section, we describe the polarimeter utilized at OPD. The instrumentation used consists primarily of a reflector telescope equipped with a polarimeter (used to analyze the transverse characteristics of the electromagnetic wave) and a detector capable of generating an image of the area of interest. This instrument essentially consists of a sequence of optical elements positioned along the path of the light beam before it reaches the detector, as shown in the schematic diagram of Fig. 1.14. A complete description of the instrument can be found in Magalhaes et al. (1996). Below is a concise discussion of the physical effects generated by each of the polarimeter's optical elements:

1. **Half-Wave Retarder Plate:** This optical device consists of a calcite crystal that splits light into two beams with different speeds, depending on the direction of the light within the crystal. The thickness of the crystal is such that a beam incident normally on its surface experiences a phase shift of π for the component of light parallel to the optical axis, relative to the perpendicular component, resulting in an advancement or delay of $\lambda/2$ for this component. For a linearly polarized incident beam, this effect corresponds to a rotation of the polarization plane of the light (Fig. 1.14a). Considering that the initial polarization plane of the light and the optical axis of the retarder form angles θ and ψ with the Celestial North Pole (CNP), the effect is a rotation of $2\psi - \theta$ of the polarization plane. The $\lambda/2$ plate can be rotated in discrete steps of 22.5°. In this way, after eight steps, a 180° rotation of the polarization plane is completed, representing a full modulation cycle.

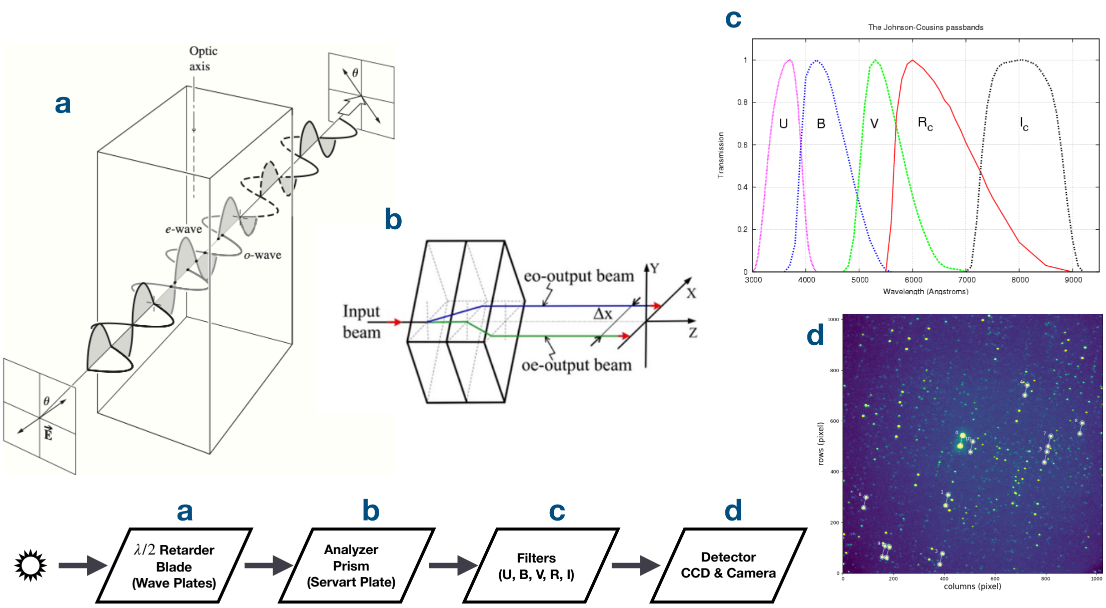

Figure 1.14: Optical components present in the polarimeters of OPD. Before reaching the detector, the light passes sequentially through the $\lambda/2$ retarder, the analyzer, and the filter. a) The effect of a $\lambda/2$ retarder on a linearly polarized beam is to cause a rotation of the polarization plane (Hecht, 2017). b) The analyzer used is a Savart prism, composed of two calcite plates joined in such a way that their optical axes are perpendicular to each other. The analyzer is responsible for splitting the incoming beam into two components with orthogonal polarization planes. Upon passing through the first calcite plate, the ordinary beam becomes the extraordinary beam and vice versa, causing a relative displacement between the two beams along the diagonal in the final image. c) Typical efficiency curves for UBVRI filters are based on the Johnson-Cousins photometric system. d) An example of an image obtained with the polarimeter is shown (from our latest observation of the Pipe Nebula region).

2. **Analyzer (Savart Prism):** This element consists of a birefringent calcite crystal, as shown in Fig. 1.14b. It is used to split the incident beam into two components with orthogonal polarization planes. Both calcite plates that compose the Savart prism are joined in such a way that their optical axes are perpendicular to each other. The effect is the subdivision of the initial beam into two orthogonally polarized components, displaced relative to the original propagation direction. Both beams are simultaneously collected by the light detector at each position of the $\lambda/2$ plate. Thus, by analyzing the intensities of the beams in all generated images, it is possible to calculate the degree and angle of polarization.

3. **Filter and Detector:** Before reaching the detector, the beam passes through a filter to select a specific spectral range (Fig. 1.14c). For OPD observations, depending on

the observational mission, either an optical CCD detector or an infrared camera was used, capable of generating images in the optical UBVRI band. In Fig. 1.14d, we show an example of an image where the sequence of polarization steps is displayed.

Calculation of Polarimetric Parameters

To derive the polarimetric data set, including the degree of polarization (P) and polarization angle (θ), for each star in the mapped fields, the IRAF astronomical data reduction software[2] is commonly used. The Solvepol package (Ramírez et al., 2017) is specifically designed to reduce and analyze polarimetric data. During data collection, as the $\lambda/2$ plate is rotated, the relative intensity between the two beams generated in the analyzer varies according to a quantity defined as the modulation amplitude z_i (for each position angle ψ_i of the retarder):

$$z_i = \hat{Q}\cos 4\psi_i + \hat{U}\sin 4\psi_i = \frac{1-(N_i^A/N_i^B)k}{1+(N_i^A/N_i^B)k}, \quad i = 1,2,3,\ldots,n, \tag{1.55}$$

where $i = 1,2,3,\ldots,n$ represents the position angles of the retarder plate.

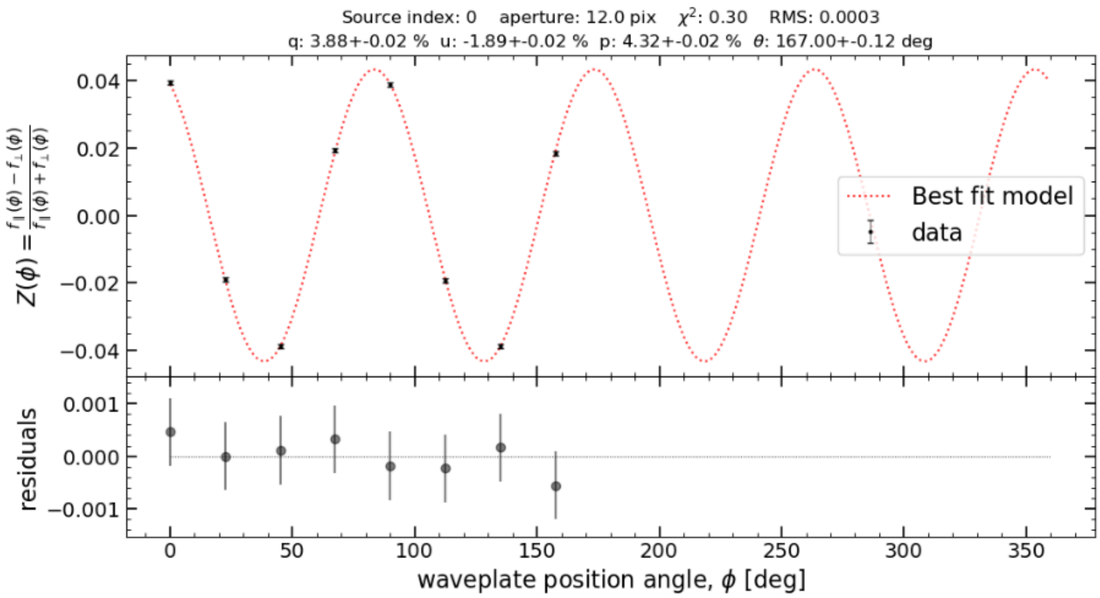

Figure 1.15: Example of modulation amplitude adjustment z_i for one of the objects in our sample. For this specific case, observations were performed at the first 8 positions of the half-wave plate. The least squares adjustment provides the values of Q and U, from which $P = (4.35 \pm 0.02)\%$ and $\theta = 167°$ (instrumental angle) were calculated.

In this equation, N_i represents the photon counts for each beam, and k is a normalization factor close to unity. The number n of images obtained was 8 for the fields of interest

[2]https://iraf.noao.edu/

and 16 for the standard stars (which provides a lower value for polarimetric errors). The important quantities here are the *Stokes Parameters* Q and U, both normalized by the total intensity I ($\hat{Q} = Q/I$ and $\hat{U} = U/I$). To calculate them, the value of z is obtained for each position i based on the relative intensities between the beams, using the right-hand side of Eq. 1.55. Subsequently, a least-squares fit is performed for the function

$$z_i = \hat{Q}\cos 4\psi_i + \hat{U}\sin 4\psi_i, \tag{1.56}$$

thereby providing the value of Q and U that minimize the scatter of the points. An example of the fit for one of the objects in our sample is shown in Fig. 1.15. From this, the degree and angle of polarization can be calculated as (see Sect. 1.2.1):

$$p = \frac{\sqrt{Q^2 + U^2}}{I}, \quad \theta = \frac{1}{2}\arctan\frac{U}{Q}. \tag{1.57}$$

Note that in Eq. 1.55, the value of z_i depends only on the intensity ratio (or photon count ratio) between the beams. This implies that the calculation is analogous to differential photometry (i.e., it is based on magnitude differences) and, therefore, independent of atmospheric variations.

1.5 Layout of this thesis

Having introduced various aspects of theoretical and practical concepts necessary for this thesis, the following chapters present the results and analysis of three observational projects. I summarize each chapter here:

- Chapter 2 explores the kinematics of the magnetized protostellar core IRAS15398-3359. This chapter focuses on understanding how magnetic fields interact with gas dynamics at the early stages of star formation. Through observations of molecular lines and polarization, we analyze the alignment between magnetic fields and the rotation axis of the core, providing insights into the role of magnetic fields in regulating gravitational collapse.

- Chapter 3 examines the influence of magnetic fields on an isolated filament near the Barnard 59 clump in the Pipe Nebula. The study analyzes magnetic field configurations and kinematic properties to understand how magnetic fields guide the accretion process onto a young protocluster. Observational data combined with theoretical modeling provide insights into the dynamics of filamentary structures in star-forming regions.

- Chapter 4 investigates the magnetic field geometry and gas dynamics of the Snake filament in the Pipe Nebula. This study combines optical, near-infrared, and submillimeter polarization data with molecular line observations. The findings reveal a coherent magnetic field alignment and a stable mass-to-length ratio, highlighting the interplay between magnetic fields and gas kinematics in quiescent filamentary regions.

- Chapter 5 provides a concise summary of the findings presented in this work, along with potential directions for future research to build upon the results of these projects.

Chapter 2

The Kinematics of the Magnetised Protostellar core IRAS15398-3359

The contents of this chapter were published in Astronomy & Astrophysics. Credit: Tabatabaei et al., A&A 672, A72, 2023

2.1 Introduction

Observing protostellar envelopes around very young protostars is fundamental to gaining a better understanding of the progression of the collapse of protostellar cores toward planetary systems. Class 0 objects are known to represent the youngest stage of protostellar evolution (André et al. 1993b; Andre et al. 2000). Most of their mass is contained in a dense envelope that accretes to the central protostar during the main accretion phase (Maury et al. 2011, Evans et al. 2009). Protostars are deeply embedded in their parent cores, which may cause interactions between protostellar outflows and surrounding gas, leading to complex morphologies. Detailing these structures will allow us to learn about the dynamics of protostellar evolution at an early stage. In light of these circumstances, it becomes essential to investigate in detail the earliest stages of star formation for specific sources.

The study of the extent and contribution of magnetic fields in star formation and the competition between magnetic and turbulent forces is still a highly debated topic in modern astronomy (e.g., Mac Low & Klessen 2004b; McKee & Ostriker 2007; Crutcher 2012a). However, in the star formation process, especially during the early stages, magnetic fields (B) are expected to play a crucial role, providing a source of non-thermal pressure against the gravitational pull (McKee & Ostriker, 2007). In light of the fact that interstellar gases are often mildly ionized (Caselli et al., 1998), the matter is likely to be coupled with the magnetic field lines at envelope scales. Due to gravity, magnetic lines bend inward, thus producing an hourglass shape, and in low-mass star-forming regions, this effect is not detected frequently (detected in 30 percent of young stellar objects in polarization; Hull & Zhang 2019a, Pattle et al. 2022a).

IRAS15398-3359 (hereafter IRAS15398) is a low-mass Class 0 protostar at a distance of 156 pc (Dzib et al., 2018a), embedded in the Lupus I molecular cloud, $\alpha_{2000} = 15^{\mathrm{h}}43^{\mathrm{m}}02^{\mathrm{s}}.2$, $\delta_{2000} = -34°09^{'}07.7^{''}$. It has a bolometric temperature of 44 K (Jørgensen et al., 2013). The protostellar mass is $0.007^{+0.004}_{-0.003}\mathrm{M}_{\odot}$ (Okoda et al., 2018). Lupus I is the least evolved component of the Lupus complex (Rygl et al., 2013), and optical polarization studies have demonstrated that Lupus I is threaded by a very ordered magnetic field that is perpendicular to its filamentary extension (Franco & Alves, 2015a). Therefore, it is an ideal place to study the kinematics of the early stages of low-mass star formation and the connection between the source kinematics and the strong large-scale magnetic field. By observing its CO emission line with the single-dish and interferometric observation, a molecular outflow was detected from this source (Tachihara et al. 1996; Bjerkeli et al. 2016; van Kempen et al. 2009). The core is embedded in a less dense ($N(H_2) \sim 10^{22}\mathrm{cm}^{-2}$) filamentary structure, which extends toward the northwest.

Based on magnetic field studies in protostellar core simulation analysis, more magnetized cores show strong alignments of the outflow axis with the magnetic field orientation, whereas less magnetized cores display more random alignment (Lee et al., 2017). Observational results present a mixture of cases. Galametz et al. (2018) used a sample of 12 low-mass Class 0 protostars to investigate the submillimeter polarized emission at scales of $\sim$ 600 - 5000 au, and demonstrated a relation between the field morphology, the core rotational energy, and the multiplicity of the protostellar system. According to that paper's analysis, the envelope scale magnetic field tends to be either aligned or perpendicular to the outflow direction, but for single sources the magnetic field is aligned along the outflow direction. Yen et al. (2021) studied 62 low-mass Class 0 and I protostars in nearby (<450 pc) star-forming regions with the orientations of the magnetic fields on 0.05–0.5 pc scales. They suggest that the outflows are likely to be misaligned with B-fields by 50 degrees in 3D space. While Hull & Zhang (2019b) used Atacama Large Millimeter/submillimeter Array (ALMA) observations with spatial resolutions of up to $\sim$ 100 au, and conclude that magnetic fields and outflows are randomly aligned in low-mass protostellar cores. The discrepancy between simulations and observations can be due to the limitations of the simulation setup. As an example, Lee et al. (2017) applied an ideal magnetohydrodynamic (MHD) simulation when in reality non-ideal MHD effect might be important (Wurster, 2021).

Redaelli et al. (2019b) used polarimetric observations of the dust thermal emission at 1.4THz obtained with the Stratospheric Observatory for Infrared Astronomy (SOFIA) telescope to investigate the magnetic field properties at the core scales toward IRAS15398. The authors found a uniform magnetic field consistent with the large-scale field derived from optical observations (Franco & Alves, 2015a). They suggested the core experienced a magnetically driven collapse and the core inherited the B-field morphology from the parental cloud during its evolution. The field lines pinch inward toward the central object, leading to the characteristic hourglass shape that is predicted by models of magnetically driven collapse. They showed that the mean direction of the magnetic field is aligned with the large-scale B-field and with the direction of outflow. Their prediction for a magnetic field strength of B = 78 μG is expected to be accurate within a factor of two. They calculated the mass-to-flux ratio, $\lambda = 0.95$, which means that the core is in a state of transition between supercritical and subcritical states.

In this paper we present new observational data that allow us to study the gas kinematics, which we compare to the magnetic field direction. The aim is to assess the importance of magnetic fields in the dynamical evolution of low-mass star-forming regions. The outline of the paper is as follows. The observations and results are described in detail in Sects. 2 and 3. In Sect. 4 we analyze the observed line profiles of $C^{18}O$ (2-1) and DCO^+ (3-2) emission lines. The results are summarized in Sect. 5.

2.2 Observations

2.2.1 APEX

IRAS15398 was observed using the Atacama Pathfinder EXperiment (APEX) single-dish antenna located at Llano de Chajnantor in the Atacama desert of Chile on 2019 September 14, 16, 17, 21, and 23. We used the PI230 receiver coupled with the FFTS4G backend in the on-the-fly mode. We used the highest spectral resolution that the FFTS4G could provide, 62.5 kHz (≈ 0.08 km s^{-1} at the frequency of the DCO^+(3-2) line). The data were reduced to a pixel size of 9 arcsec. The broad bandwidth of the PI230 receiver can be set up to observe simultaneously $C^{18}O$ (2-1) and the DCO^+(3-2) transitions at 219.560 GHz and 216.113 GHz, respectively, the target lines of this research. The angular resolution at these frequencies is ~ 28 arcsec, corresponding to 0.02 pc at the source distance 156 pc (Dzib et al., 2018a). The data reduction was performed based on the standard procedure of the CLASS software, GILDAS.[1] The antenna temperature, T_A, was converted to main-beam brightness temperature using the forward efficiency ($\eta_{\rm fw}$) and main beam efficiency, $T_{\rm mb} = T_{\rm A} \frac{\eta_{\rm fw}}{\eta_{\rm mb}}$, given a main beam efficiency $\eta_{\rm mb} = 0.8$.[2]

2.2.2 Herschel

We used archival data from the Gold Belt Survey, obtained with the *Herschel* space telescope to obtain the gas column density and the dust temperature (Bontemps et al. 2010, Rygl et al. 2013, Benedettini et al. 2018). The N(H_2) column density map has a resolution of ~ 38 arcsec.

2.3 Result

Figure 2.1 presents the moment 0 (integrated intensity) maps of $C^{18}O$ (2-1) and DCO^+ (3-2) overlaid with the contours of H_2 column density. The mean rms in $T_{\rm mb}$ scale is 0.1 K and 0.08 K for $C^{18}O$ (2-1) and DCO^+ (3-2), respectively. On the basis of emission-free

[1] https://www.iram.fr/IRAMFR/GILDAS/
[2] www.apex-telescope.org/telescope/efficiency/

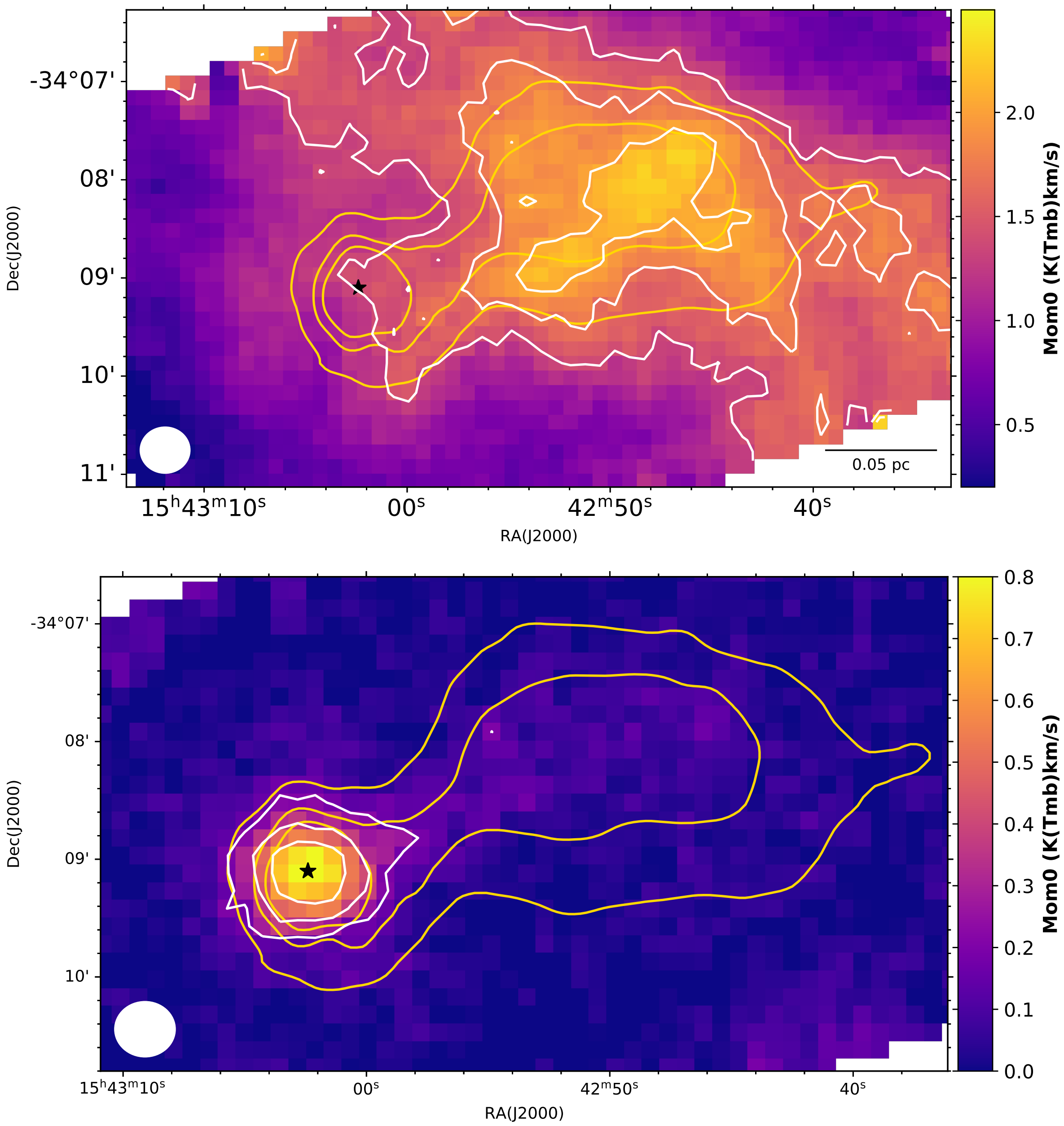

Figure 2.1: Integrated intensity of $C^{18}O$(1-2) (top) and DCO^{+}(3-2) (bottom) toward IRAS15398. The white contour levels are 10, 20, and 30 times the mean rms value for the DCO^{+} line and 40, 50, and 60 times the mean rms value for the $C^{18}O$ (2-1) line. The beam size is shown in the bottom left corner. The yellow contours in both images show H_2 column density (levels:[1.0, 1.5, 2.0] 10^{22} cm^{-2}). The black star gives the position of the protostar.

channels only, we derived the mean rms per channel for each transition. This rms is used to associate uncertainties at each pixel to the integrated intensity, the mean value for $C^{18}O$(2-1) and DCO^+(3-2) being 0.03 K km s^{-1} and 0.02 K km s^{-1}, respectively. These lines are optically thin and do not present crowded hyperfine structures. In order to confirm this hypothesis, we evaluate the opacity as

$$\tau = -\ln\left[1 - \frac{T_{\rm MB}}{J_\nu(T_{\rm ex}) - J_\nu(T_{\rm bg})}\right], \tag{2.1}$$

where $T_{\rm ex} = 12$ K is the excitation temperature (obtained from the *Herschel* dust temperature map, see also Sect. 4.1), $T_{\rm MB} = 3.5$ K is the peak main beam temperature, the function J_ν is the equivalent Rayleigh–Jeans temperature, and $T_{\rm bg} = 2.73$ K is the cosmic background temperature. Therefore, we obtain $\tau = 0.66$. For the DCO^+ (3-2) line we obtain $\tau = 0.44$ using $T_{\rm MB} = 1.0$ and $T_{\rm ex} = 7$ K. Through a combination of excitation and abundance, distinctive species give complementary information on gas conditions. Due to its relatively high abundance and low critical density $n_{\rm cr}(C^{18}O(2\text{-}1)) \sim 10^4 \rm cm^{-3}$, computed with numbers in the LAMDA database,[3] $C^{18}O$ (2-1) is a sensitive tracer of relatively low-density material in the cloud, which traces the more extended gas in the filamentary structure. The DCO^+(3-2) molecule, on the other hand, presents a higher critical density $n_{\rm cr}(DCO^+(3-2)) \sim 10^6 \rm cm^{-3}$, which makes it more selective of dense gas closer to the central protostar. DCO^+ (3-2) emission is also known as a remarkably sensitive tracer for gas properties during the early stages of protostellar evolution (e.g., Gerner et al. 2015). In the location of the protostar, we see a decrease in the $C^{18}O$ (2-1) integrated intensity, suggesting that the molecule is partially depleted onto the dust grains (Caselli et al. 1999, Bacmann et al. 2002). Figure 2.2 shows the channel maps of the $C^{18}O$ (2-1) line. The figure presents the signal emission at velocity intervals of ≈ 0.2 km s^{-1}.

2.4 Analysis

2.4.1 Column density maps

To calculate the column density map of these two molecules we used the same procedure as used in Redaelli et al. (2019a) and Caselli et al. (2002a) for an optically thin transition. The DCO^+ (3-2) and $C^{18}O$ (2-1) lines are both optically thin, as we show in the previous section. The expression of the total column density derived by an optically thin transition is given by

$$N_{\rm col} = \frac{8\pi W \nu^3}{c^3 A_{\rm ul}} \frac{Q(T_{\rm ex})}{J_\nu(T_{\rm ex}) - J_\nu(T_{\rm bg})} \frac{e^{\frac{E_u}{k_B T_{ex}}}}{g_{\rm u}(e^{\frac{h\nu}{k_B T_{ex}}} - 1)}, \tag{2.2}$$

where $T_{\rm ex}$ is the excitation temperature, the function J_ν is the equivalent Rayleigh–Jeans temperature, $T_{\rm bg} = 2.73$ K is cosmic background temperature, $E_{\rm u}$ is the upper state energy,

[3] https://home.strw.leidenuniv.nl/~moldata/

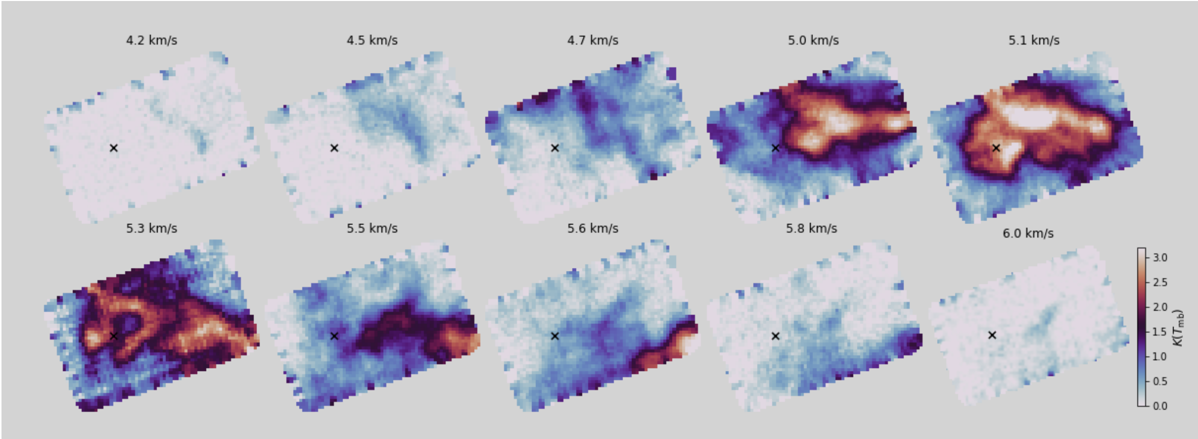

Figure 2.2: Channel maps of $C^{18}O$ (2-1) emission. The black cross indicates the position of the protostar core. The velocity of each channel is shown above each panel.

g_u is the degeneracy, A_{ul} is the Einstein coefficient, Q is the partition function, ν is the line frequency, h is the Planck constant, k_B is the Boltzmann constant (see Table 1 for details),[4] and W is the integrated intensity of the line. Since the DCO^+ (3-2) transition shows only one velocity component, we use the result of the Gaussian fit to compute the integrated intensity of this line (see Sect. 4.2 for more details) by calculating the area under the Gaussian profile. The $C^{18}O$ (2-1) emission, instead, shows signs of multiple velocity components along the line of sight. We, therefore, compute the integrated intensity from the data cube, integrating emission over the velocity range [4 - 6.5]$\mathrm{km\,s^{-1}}$, which contains the whole line profile.

Table 2.1: Spectroscopic parameters used to derive the molecular column density.

Transition	ν (GHz)	g_u	$E_u/10^{-22}$ (J)	$A_{ul}/10^{-3}$ (s^{-1})	Q(7^a)
$C^{18}O$(2-1)	219.56	5	2.18	6.01 10^{-4}	-
DCO^+(3-2)	216.112	7	2.86	7.65	4.40^b

Note: All the data are from the Cologne Database for Molecular Spectroscopy (CDMS) documentation.[4]
[a] The excitation temperature of $C^{18}O$ (2-1) is 7K. [b] Calculated via interpolation of the Partition function available at CDMS, for different temperatures.

We use the dust temperature map to approximate the excitation temperature for the $C^{18}O$ (2-1) line, obtained from *Herschel* data (Benedettini et al. 2018, Rygl et al. 2013) since we expect this line to be thermally excited. This assumption may induce some

[4] https://cdms.astro.uni-koeln.de/cgi-bin/cdmssearch

small errors as at the volume densities traced by the $C^{18}O$ (2-1) line the gas and dust are not thermally coupled (Goldsmith, 2001). We therefore use the dust temperature as a proxy for the gas kinetic temperature. On the contrary, the DCO^+ (3-2) line is the 3–>2 transition, which has a high critical density; therefore, the dust temperature is not a good approximation for excitation temperature because we expect the line to be subthermally excited, so we use excitation temperature equal to 7 K with a variation of 2 K for this line. The column density peak for the DCO^+ and H_2 is found at the protostar position. For the protostar position, the $C^{18}O$, DCO^+, and H_2 column densities are $(7.8 \pm 0.1) \times 10^{14}\mathrm{cm}^{-2}$, $1.4^{+2.24}_{-0.5} \times 10^{12}\mathrm{cm}^{-2}$, and $(4.2 \pm 1.8) \times 10^{22}$ cm^{-2} (Roy et al., 2014a), respectively. The column density for H_2 is obtained based on the *Herschel* map.

2.4.2 Spectral line analysis

In order to derive the kinematics parameter maps (e.g., V_{lsr}, σ_V), we perform a Gaussian fitting of the transitions using the PYSPECKIT package of python (Ginsburg & Mirocha, 2011a). For the DCO^+ (3-2) data cube, we use a single-Gaussian component fit. The initial guesses are then 2.5 K, 5.2 $\mathrm{km\,s^{-1}}$, and 0.2 $\mathrm{km\,s^{-1}}$ for the amplitude, velocity dispersion, and width, respectively.

Instead, $C^{18}O$ (2-1) presents more complex kinematics. It often shows two velocity components in its profiles. Since the line is optically thin, as shown in Sect. 3, we are confident that these are multiple velocity components and they are not due to self-absorption. In order to fit two Gaussian profiles on the $C^{18}O$ (2-1) data we perform a simple S/N cut, we mask those pixels where $\frac{T_{\rm MB}^{\rm peak}}{rms} < 20$, then fit one Gaussian profile to all the unmasked pixels (65% of the pixels). Then we fit two Gaussians for those pixels that had a residual larger than $2 \times rms$ and those Gaussian fits with a width broader than 0.25 $\mathrm{km\,s^{-1}}$ in the previous step. By visual inspection we find that lines broader than 0.25 $\mathrm{km\,s^{-1}}$ show profiles consistent with two velocity components on the line of sight. For the second time we check the Gaussian fit profiles and for those pixels that have residuals bigger than $2 \times rms$ we do the fitting one more time with different initial guesses (60% of the pixels with S/N cut), which means they always have residuals less than two times the rms. As a final step, if the error on the velocity dispersion or velocity and on the amplitude is larger than 1 $\mathrm{km\,s^{-1}}$ and 1 K, respectively, we remove the fit. By doing this, we remove fits with unreasonably large uncertainties, which indicates that they have been poorly fitted. Figure 2.3 shows the fit results overlapped with the data.

The grid of spectra of $C^{18}O$ (2-1) and DCO^+ (3-2) lines for 40 positions at 18 arcsec intervals from each other around the core is shown in Fig. 2.3 (for more details about the position of each spectrum, see Appendix A). The red histogram represents the DCO^+ (3-2) spectrum and the black histogram is the $C^{18}O$ (2-1) spectrum. The blue curves represent the fit when the code uses a two-Gaussian and the green curves are the fit when the code used one Gaussian for the $C^{18}O$ (2-1) line. The vertical line is $V_{\rm sys} = 5.2$ $\mathrm{km\,s^{-1}}$, which is the systematic velocity computed from $C^{18}O$ (2-1) line which was reported in Yen et al. (2017) ($V_{\rm sys} = 5.24 \pm 0.03$ $\mathrm{km\,s^{-1}}$), which is consistent with the systematic velocity seen in

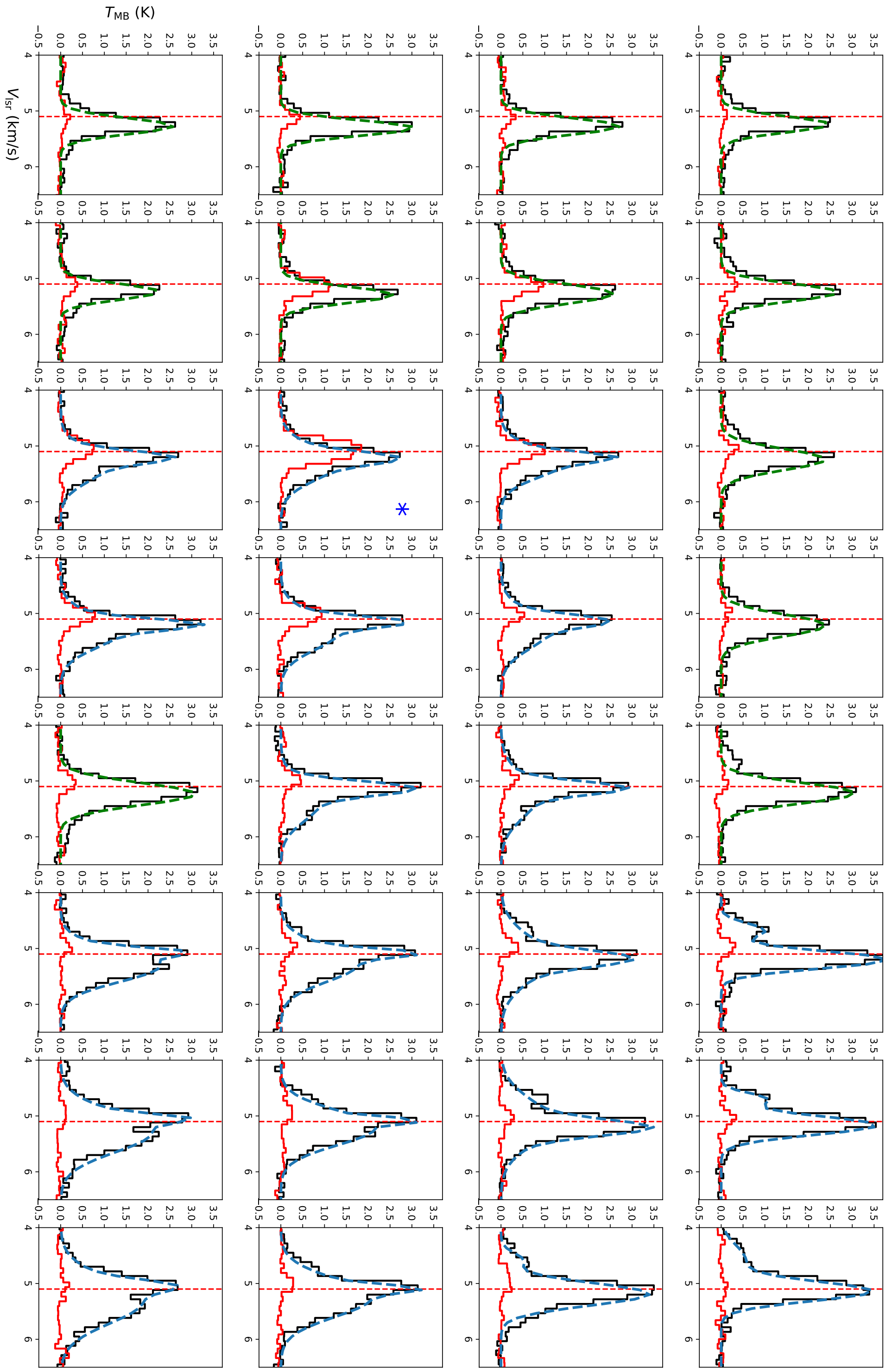

Figure 2.3: Spectrum grid of $C^{18}O$ (2-1) (black histogram) and DCO^{+} (3-2) (red histogram) for 40 random positions around the core. Shown are the two Gaussian fits (blue curves) and one Gaussian fits (green curves) to the $C^{18}O$ (2-1) line. The vertical line is V_{lsr}=5.2 km s^{-1}. The blue star shows the spectrum for the position of the central protostar.

our data.

The DCO^+ (3-2) spectra always show a single velocity component with a Gaussian profile. This line traces only one velocity component that is associated with the high-density material. On the other hand, as already mentioned, $C^{18}O$ (2-1) shows two velocity components in their profiles. The brightest component is the one close to the velocity of the DCO^+ (3-2) line, and it hence arises from the high-density material. The fainter component of $C^{18}O$ (2-1) can appear on the red or blue side of the stronger component, depending on the location in the cloud. In total, there are three different velocity components, the main one at 5.2 km/s (in all panels on all DCO^+ (3-2) spectra locations), a lower velocity component seen in the northwestern panels, and a higher velocity component seen in the southwestern panels. In the first two rows of Fig. 2.3 the faint component appears on the blue side, and in the two bottom rows of the spectrum grid it appears on the blue side of the stronger component.

In Fig. 2.3, we can see the line profiles change across the grid. The multiple velocity components of $C^{18}O$ (2-1) along the line of sight appear to merge from east to west (moving toward the position of the protostar). $C^{18}O$ (2-1) is a lower-density tracer than DCO^+ (3-2); these fainter velocity components, seen only in the former tracer, are likely additional nearby low-density filamentary clouds along the line of sight. The core envelope then appears to be found in the correspondence of the merger of these structures. In the following subsections, we discuss the maps of the kinematics parameters for each tracer individually.

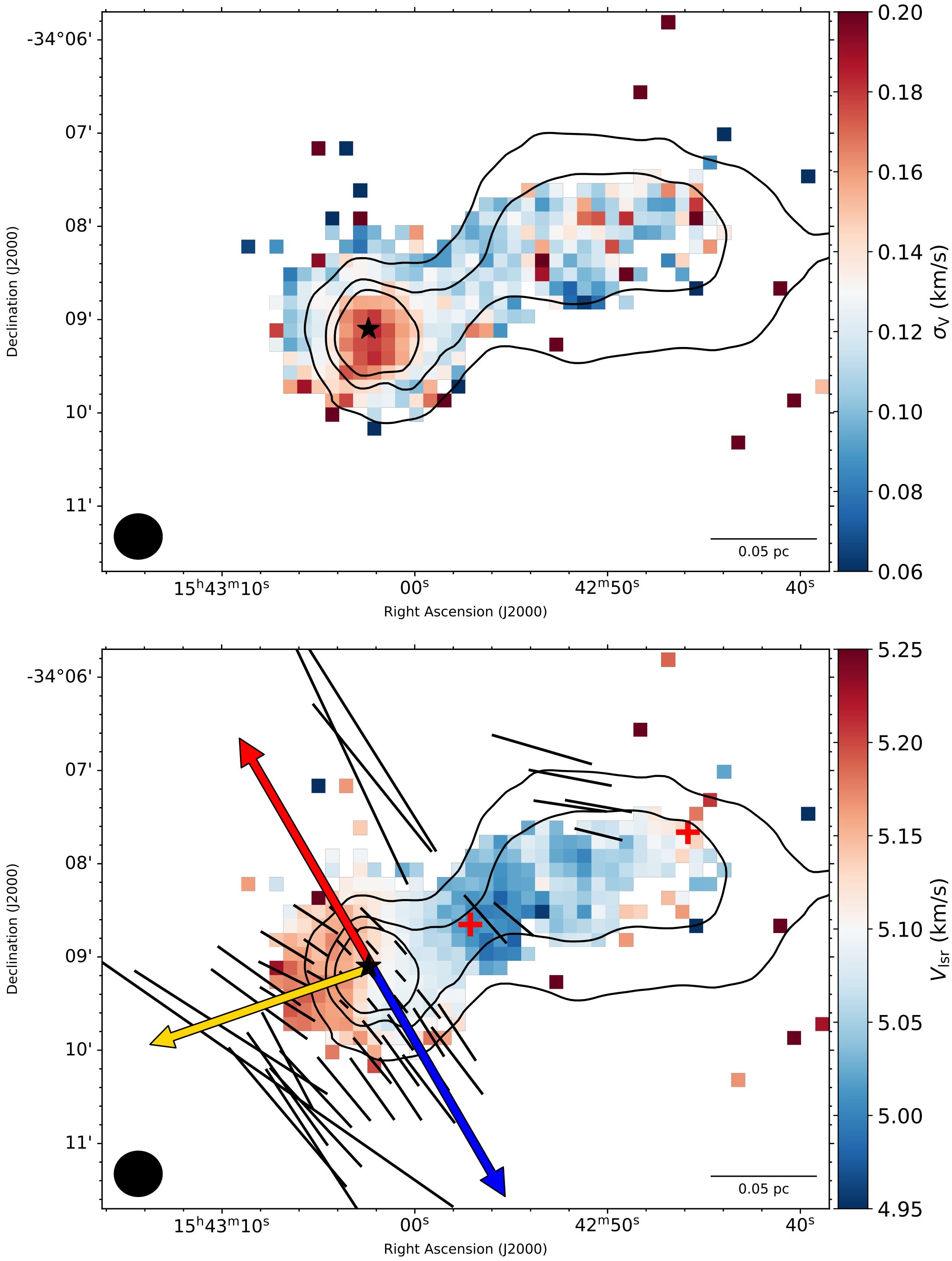

Figure 2.4: Maps of kinematic parameters. Top: Gas velocity dispersion of the cloud traced using the DCO^+ (3-2). Bottom: Centroid velocity map obtained fitting the observed DCO^+ (3-2). The black vectors represent the polarization angles, tilted by 90 degrees to trace the magnetic field direction (Redaelli et al., 2019b). The blue and red arrows show the direction of the outflow ($PA = 35°$, from Bjerkeli et al. 2016), and the yellow arrow presents the mean velocity gradient direction around the core. The star shows the position of the protostar. The contours represent $N(H_2)$ column density levels, as derived from *Herschel* data: [1.0, 1.5, 2.0] 10^{22} cm^{-2}.

2.4.3 DCO$^+$ (3-2) line

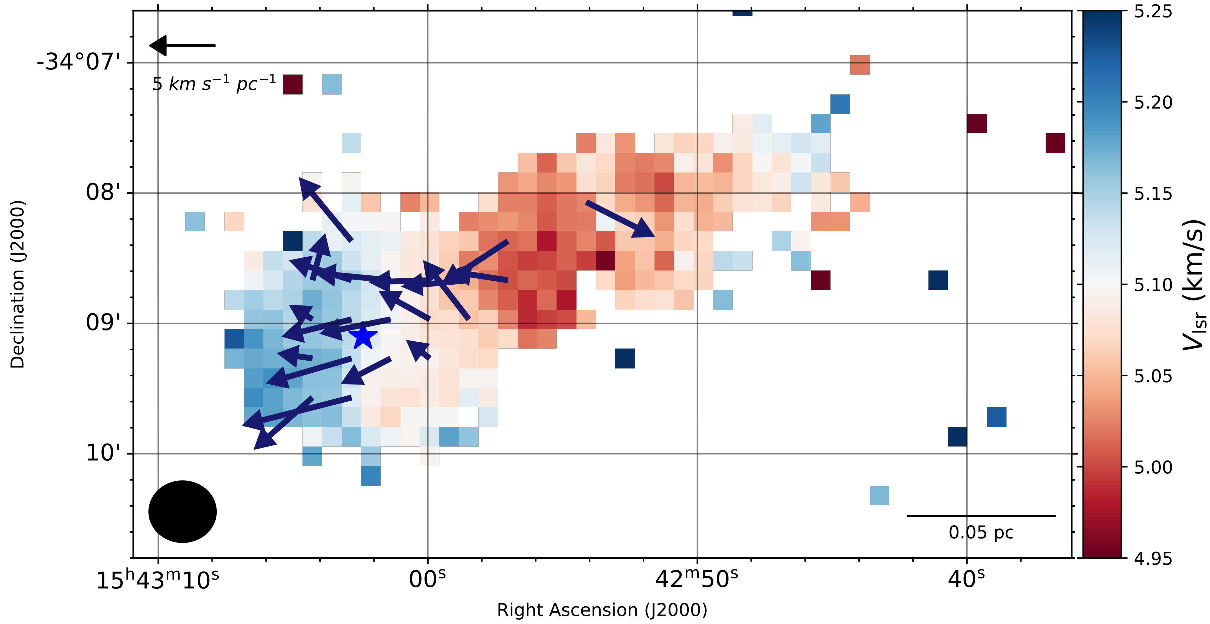

Figure 2.5: Centroid velocity map of the DCO$^+$ (3-2) line overlaid with the gradient arrows (only vectors with $S/N > 3$ are shown). The arrow length represents the relative vector magnitude of the gradient, according to the scale shown in the top left corner, and the direction of the arrows points to the steepest velocity field change.

In Fig. 2.4 (top panel) we show the velocity dispersion map, which presents a clear increase toward the center of the protostar envelope, starting with very narrow lines in the outer region (around the filament). The mean velocity dispersion derived from DCO$^+$ (3-2) of the gas in the filament is in fact $\langle\sigma_V\rangle = 0.12 \pm 0.02$ km s^{-1}, but it becomes broader toward the center; for the positions where N(H_2) $> 3.2 \times 10^{22}$ cm^{-2} (inner contour in the Fig. 2.4), we derive $\langle\sigma_V\rangle = 0.175 \pm 0.006$ km s^{-1}. This increase is linked to the protostellar activity, injecting turbulence, and it could also be caused by the rotation of the core.

We also observe oscillatory motions in the velocity field (visible in the C^{18}O data as well, see Fig. 2.7, the green dots), which have been seen before in the large-scale velocity patterns. This velocity pattern is consistent with core-forming motions (Hacar & Tafalla, 2011). A small velocity gradient can be seen along the filament, which could be linked to the ongoing accretion material toward the central object.

The filament extends over ~ 0.1 km s^{-1} in velocity toward the protostar from 5.1 km s^{-1} in the west side to 5.0 km s^{-1} at the eastern edge. These positions are shown with red plus signs in Fig. 2.4. We determine a conservative estimate of the length of the filament of 0.11 pc. This value is computed based on the H_2 column density from *Herschel* data, an area with a higher value than 1.5×10^{22} cm^{-2}. In this border, we find almost all of the filament (second contour in Fig. 2.4). Thereby the velocity gradient is $\nabla V = \Delta V/\Delta R = 0.91 \pm 0.23$

$\mathrm{kms^{-1}pc^{-1}}$. To compute the mass of filament, we employ this relation:

$$M_{\mathrm{fil}} = \sum_{i=1} N(\mathrm{H_2})_{\mathrm{i}} \times \mu \times \mathrm{m_H} \times \mathrm{A}. \tag{2.3}$$

In this case, we obtain $M_{\mathrm{fil}} = 1.04\mathrm{M_\odot}$, where $\mathrm{N(H_2)}$ is gas column density of the i_{th} pixel and A is the area of the pixel; $\mu = 2.8$ and m_{H} are gas mean molecular weight per hydrogen molecule and hydrogen mass, respectively. Therefore, we quantify the mass accretion rate along the filament, $\dot{M}_{\mathrm{acc}} = M_{\mathrm{fil}} \times \nabla V = 9.7 \times 10^{-7}\mathrm{M_\odot yr^{-1}}$. This value is affected by some sources of uncertainty. We consider a 2% error on the distance (Dzib et al., 2018a), a 12% error on the calibration, and a 40% error due to the assumption of the dust opacity index (Benedettini et al. 2018, Roy et al. 2014a). The uncertainty on the mass estimation with all these three errors is a total of 42%. With the 26% error on the velocity gradient, we get a final relative error of 49% for the value of the mass accretion rate. In addition, the inclination of the filament with respect to the plane of the sky is unknown, and it has an influence on the value of $\dot{M}_{\mathrm{acc}}$ by a factor of tan i (see, e.g., Chen et al. 2019). The derived value of the accretion rate changes by up to 70% if the inclination varies between 30 and 60 degrees. Therefore, considering these factors, we assume that the derived $\dot{M}_{\mathrm{acc}}$ value is accurate within a factor of two. This mass accretion rate is comparable to the value that Pineda et al. (2020) found for a streamer of material connecting a protostar, Per-emb-2 (IRAS 03292+3039), to the surrounding cloud ($\dot{M}_{\mathrm{acc}} = 10^{-6}\mathrm{M_\odot yr^{-1}}$). The accretion rate that we calculate here is for a filament, not a streamer. However, this filament is diffuse and not very dense. Furthermore, the value we found is comparable to the mass infall rate of protostellar envelopes estimated in other young objects $\sim 3 \times 10^{-6}$ (Evans et al., 2015).

We detect another velocity gradient around the protostar in the west–east direction, which could be due to the rotation of the core. In this scenario, the rotation axis would lay in the north–south direction (PA = 16°; see last paragraph of the section), close to the direction of the detected bipolar outflows found by Bjerkeli et al. (2016), which are shown with the blue and red arrows in the bottom panel of Fig. 2.4 (PA = 35°). Redaelli et al. (2019b) also showed that this outflow direction is almost parallel to the mean magnetic field, which has the direction of PA=45±7°. The black vectors in the bottom panel of Fig. 2.4 represent the polarization angles, tilted by 90 degrees to trace the magnetic field direction. The rotation axis and magnetic field lines are moderately well aligned (with an offset of 29°). According to the magnetohydrodynamic (MHD) collapse models, magnetic braking should be effective in this cloud (Joos et al. 2012, Li et al. 2013, Krumholz et al. 2013, Seifried et al. 2015), which is consistent with the absence of a resolved Keplerian disk (down to 30 AU, Yen et al. 2017). Okoda et al. (2018) observed IRAS15398-3359 with better resolution (0.2" angular resolution). A disk of no more than 30 au in size was detected in their analysis with a mass between 0.006 and 0.001 $\mathrm{M_\odot}$. This is a very small disk that is consistent with magnetic braking. Magnetic braking is in fact an efficient way to remove angular momentum from infalling and rotating material, suppressing envelope fragmentation and the formation of large disks (Li et al., 2014b).

The velocity gradient over the protostar shows gas motions likely consistent with the rotation of the core. To analyze the gas motions further, we employ a two-dimensional representation of the velocity gradients. Figure 2.5 shows the centroid velocity of DCO^+ (3-2), overlaid with the gradient velocity arrows. The arrow length represents the relative vector magnitude of the gradient and the direction of the arrows point in the direction of increasing velocity. The method used here followed the analysis of Goodman et al. (1993), and developed by Caselli et al. (2002a), to find the velocity gradient based on a linear fit between offset declination and the velocity. By assuming that the core rotates as a solid body, $V_{\rm LSR}$ would only depend on the coordinates in the sky and not on the distance along the line of sight. In this approximation, the centroid velocity of the line is a linear function of the offset on the plane of the sky

$$V_{\rm LSR} = V_0 + a\Delta\alpha + b\Delta\delta, \tag{2.4}$$

where $\Delta\alpha$ and $\Delta\delta$ represent offsets in right ascension and declination, and V_0 is the systemic velocity of the cloud with respect to the local standard of rest. The coefficients a and b, together with V_0, can be obtained by least-squares fitting. The velocity gradient magnitude is then (Goodman et al., 1993)

$$\nabla V_{\rm LSR} = \sqrt{(a^2 + b^2)}, \tag{2.5}$$

and its direction toward increasing velocity $\Theta_{\nabla V}$ is given by

$$\Theta_{\nabla V} = \tan^{-1}\frac{a}{b}. \tag{2.6}$$

We use this method and obtain the velocity gradient and the position angle with their uncertainties. The number of pixels used to carry out the fit is 9, which is appropriate for single-dish data that is Nyquist sampled (Caselli et al., 2002a).

We only consider values with S/N > 3 in the final result for each velocity gradient value; the mean signal-to-noise ratio around the protostar position is 7. The mean velocity gradient magnitude distribution around the core peaks at 5.1 ± 0.7 km s^{-1} pc^{-1} and has a mean position angle of $(106 \pm 7)^\circ$ (counterclockwise from the north toward the east), which is shown as a yellow arrow in Fig. 2.4. We can see that this mean velocity gradient is consistent at the $3\times\sigma$ level to be perpendicular to the direction of the bipolar outflow found by Bjerkeli et al. (2016) (PA=35°). We assume that the total gradient is the rotational direction of the core. This method is implemented in a Python code which is available via open access on GitHub.[5]

2.4.4 $C^{18}O$ (2-1) line

Figure **??** represents the centroid velocity map obtained fitting the observed $C^{18}O$ (2-1) spectra. The left panel of Fig. **??** represents the brightest components of the Gaussian fitting, and as we discussed in Sect. 4.2, in some locations of the cloud $C^{18}O$ (2-1) gas reveals two velocity components. The right panel of Fig. **??** shows the second component,

[5] https://github.com/jpinedaf/velocity_tools

the one with lower intensity. Depending on the location on the map, this less bright component has red or blue velocities compared to the main component. The right panel of Fig. ?? shows that by moving from north to south the faint component is going to the red side of the brightest components. The red velocities appear mostly on the south of the filament and the west side of the protostar position. This is similar to our discussion in Sect. 4.2, where there are three components along the line of sight: the bright one associated with the core and two fainter ones, one in the north and one in the south of the filament.

A small velocity gradient can also be seen in the brightest component of the $C^{18}O$ (2-1) emission around the protostar in the east–west direction, in agreement with what we discuss in Sect. 4.3 for the DCO^+ (3-2) line, which is likely associated with the rotation of the core. For positions where $N(H_2) > 2 \times 10^{22}$ cm^{-2}, the mean value of the centroid velocity is $\langle V_{\rm lsr} \rangle = 5.22$ km s^{-1} with an uncertainty 0.04 km s^{-1}. The $V_{\rm lsr}$ value at the west side of the core is 5.169 ± 0.005 km s^{-1} and increases toward the east side of the core up to the value 5.290 ± 0.003 km s^{-1}. These two values are calculated at the edge of the core, where the $N(H_2)$ is equal to 2×10^{22} cm^{-2} (the inner contour in Fig. ??).

Frau et al. (2015) proposed for the Pipe nebula that the sharp changes in the magnetic field is produced by shocks between two clouds and, in comparison to the non-shocked gas, the column density and magnetic field strength double. Redaelli et al. (2019b) observed a sharp change in the magnetic field toward dust extension in the northwest direction of this cloud with respect to the core magnetic field. We predict that this is produced by merging two distinct clouds, two components of the $C^{18}O$ (2-1) line. These polarization vectors, which show different directions concerning the vectors in the core position, could result from the cloud collision.

2.4.5 Comparison between the $C^{18}O$ (2-1) and DCO^+ (3-2) kinematic

The result of the fitting procedure is shown in Fig. 2.7, where we present an image depicting a 3D position-position-velocity (PPV) diagram highlighting the distributions of DCO^+ (3-2) and $C^{18}O$ (2-1) gas throughout the cloud. Each data point illustrates the location and centroid velocity of an independent Gaussian component. The color of each data point relates to each spectral component (discussed in Sect. 4.2). Orange refers to DCO^+ (3-2) emitting gas, and the others refer to $C^{18}O$ (2-1) emitting gas. The velocity structure of the $C^{18}O$ (2-1) emission is quite complex. Four velocity components are displayed in total. Overall, for $C^{18}O$ (2-1) we used only two-component fitting, but here we display it in different categories. The blue data correspond to the brightest components of the $C^{18}O$ (2-1) gas, and the red and cyan points instead are related to the secondary fainter component, when it is located at lower and higher velocities, respectively, with respect to the brightest one.

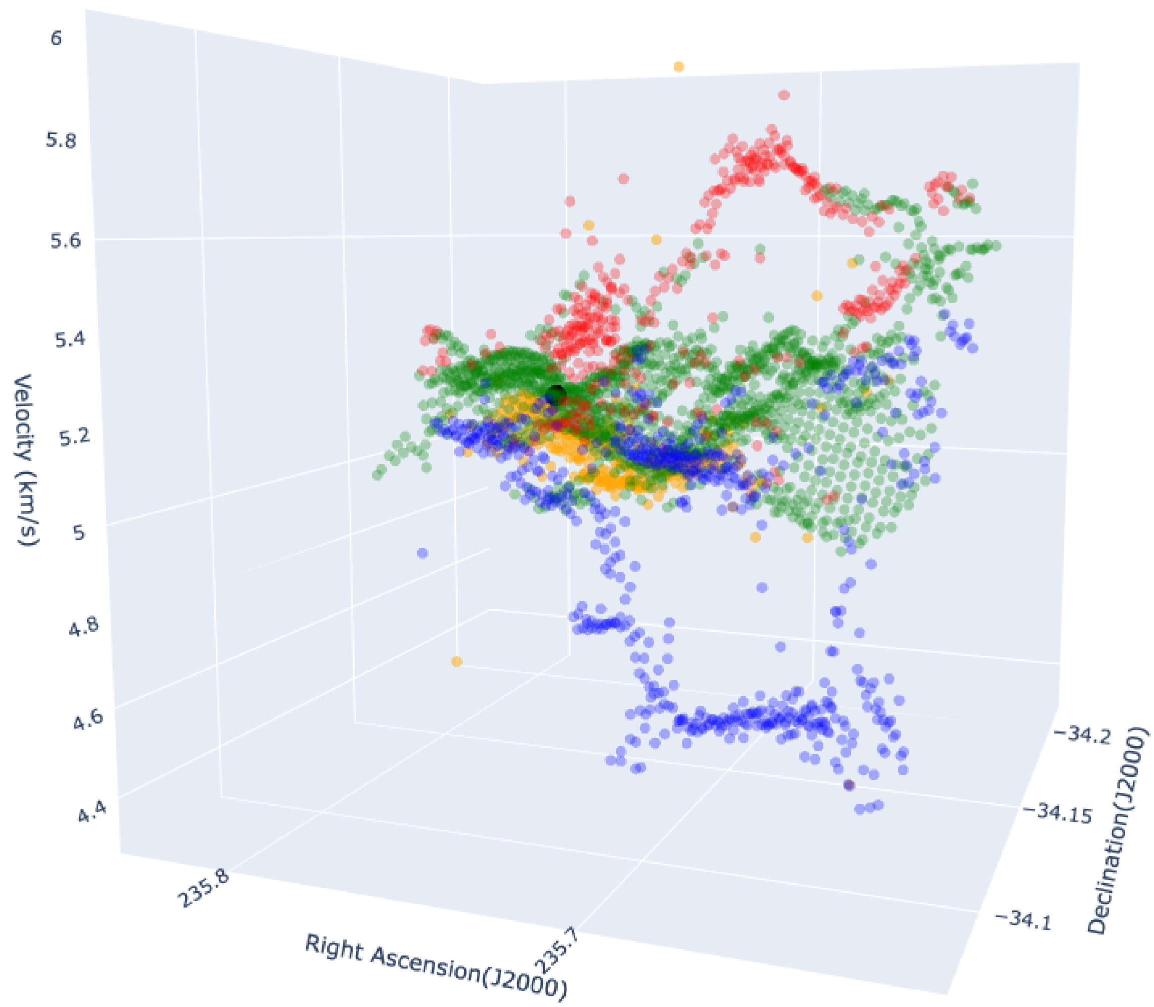

Figure 2.7: PPV image of $C^{18}O$ (2-1) and DCO^+ (3-2) gas. Each data point denotes the location and centroid velocity of a Gaussian component and each color refers to a different Gaussian fit. The centroid velocity is shown for the DCO^+ (3-2) line (in orange), and the green data points represent the brightest component of the $C^{18}O$ (2-1) line. The red and blue data points indicate the two lower-intensity velocity components. The black circle represents the position of the protostar.

We observe a systematic difference between the centroid velocity of DCO^+ (3-2) and the main component of $C^{18}O$ (2-1), suggesting that they are not tracing exactly the same gas. We speculate that this is related to the fact that one is an ion and the other is a neutral species, and they behave differently concerning the magnetic fields, or it could be because of the difference between their gas densities. It is important to note that if ions and neutrals behave differently at the same density, this indicates a violation of the flux-freezing assumption. We discuss this point in more detail in Sect. 5.

Figure 2.7 shows that the main velocity component of the $C^{18}O$ (2-1) data and the DCO^+ (3-2) line present a systematic velocity shift. The $C^{18}O$ (2-1) data always appear at a higher velocity than the DCO^+ (3-2) spectra. In order to investigate this point further, we show in Fig. 2.8 the velocity difference $V_{\rm lsr}(C^{18}O)$ - $V_{\rm lsr}(DCO^+)$ with the H_2 column density overlaid on top. In addition, we did not find any correlation between the velocity shift and the H_2 column density map. In this figure the shift between $C^{18}O$ (2-1) and DCO^+ (3-2) is clearly visible. We report a mean velocity shift of 0.13 $\mathrm{km\,s^{-1}}$ across the whole source. The largest velocity shift values are found on the west side of the protostellar core, where the infalling material from the envelope reaches the core, under the assumption that the small velocity gradient seen along the filament represents an accretion flow. On the southeast and northwest sides of the core there is a very low-velocity shift, equal to $\sim$ 0.06 $\mathrm{km\,s^{-1}}$ and these values are increasing toward the protostar position up to 0.10 $\mathrm{km\,s^{-1}}$. To calculate these low-velocity shifts we use the pixels indicated with a black plus sign in Fig. 2.8.

2.5 Discussion

Star-forming regions can be more completely understood by analyzing the distribution of different molecular species in the velocity. We compare the velocity shift between these two tracers in the cloud. The velocity shift between a neutral and an ionized species was observed in the past. For instance, Henshaw et al. (2013a) studied the large-scale velocity field throughout the cloud in G035.39-00.33, and found a velocity shift between the two tracers of N_2H^+(1-0) and $C^{18}O$ (1-0), in agreement with a model of collision between filaments that is still ongoing. It follows that the velocity structure of the core does not have intrinsic properties but is a product of large-scale motions on filamentary scales. They proposed that the velocity difference in the cloud occurs because of filament merging, implying that higher velocity filaments are interacting with a lower velocity, less massive filament, increasing the density of an intermediate velocity filament (Barnes et al., 2018).

Another scenario is that the velocity shift between the $C^{18}O$ (2-1) and DCO^+ (3-2) reveals relative motions between the dense gas, traced by DCO^+ (3-2), and the surrounding less dense envelope, traced by $C^{18}O$ (2-1). DCO^+ (3-2) is simply tracing higher densities, which may not necessarily have the same velocities as the gas traced by $C^{18}O$ (2-1), especially because the $C^{18}O$ (2-1) emission is much more extended, so the kinematics derived from the line profile is affected by lower density material not seen in DCO^+ (3-2). According to Zhang et al. 2017, velocity shifts between high-density and low-density tracers within a cloud are indicative of gas expanding and contracting. It is based on the assumption that the higher critical density molecules trace the dense gas closer to the inner of a core, while lower critical density molecules trace the more extended gas in the outer envelope.

Magnetic braking might have had a great impact in this cloud. We determined that the rotation axis of the core and magnetic field lines are almost aligned. According to the magnetohydrodynamic (MHD) collapse models, magnetic braking should be effective in this cloud, which is in agreement with the absence of a resolved Keplerian disk. Magnetic braking is an effective way to remove angular momentum from infalling and rotating material, suppressing envelope fragmentation and the formation of large disks.

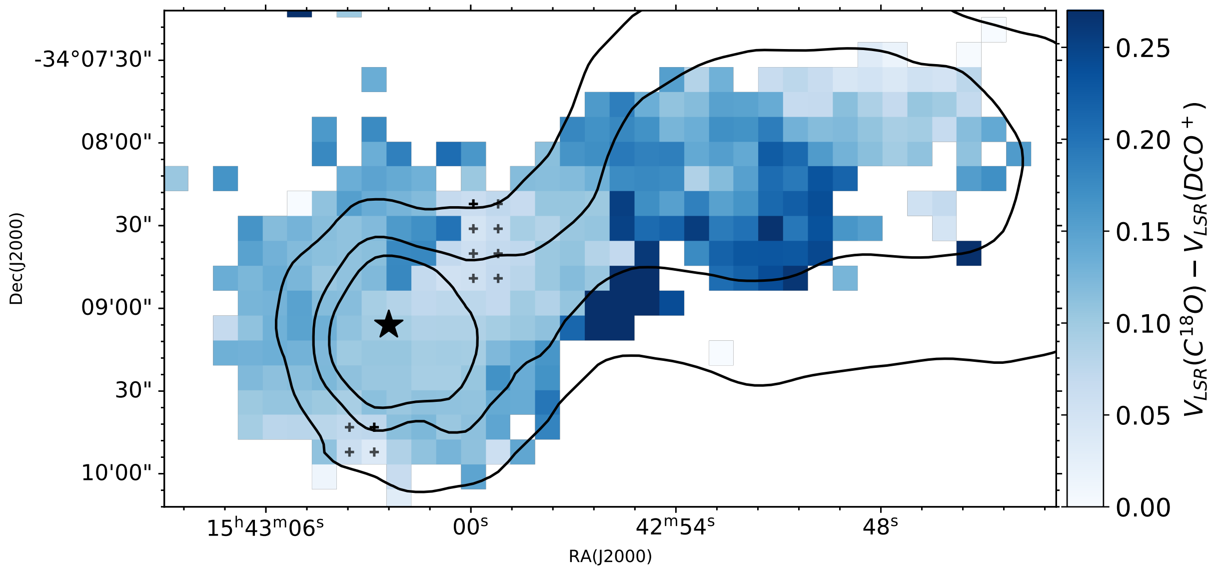

Figure 2.8: Map of velocity shift between $C^{18}O$ (2-1) and DCO^+ (3-2). Overlaid in black contours is the H_2 column density (levels:[1.0,1.5,2.0] 10^{22} cm^{-2}). The black star represents the position of the protostar and the black plus signs are positions of the lowest velocity shifts, which are used for the mean value.

2.6 Conclusions

We studied the region around the young low-mass Class 0 source IRAS15398 using APEX. The kinematic analysis performed with the $C^{18}O$ (2-1) emission line as a low-density material tracer (extended gas) and with the DCO^+ (3-2) line as a tracer of dense gas closer to the protostar. The measured kinematics parameters revealed several properties by performing Gaussian fitting, using the PYSPECKIT package. Our main conclusions can be summarized as follows:

- From the spectral line profiles we conclude that the two velocity components of $C^{18}O$ (2-1) in the west side of the region have merged together toward the position of the protostar. $C^{18}O$ (2-1) is a lower-density tracer than DCO^+ (3-2); the fainter velocity component seen only in the former tracer is likely low-density filamentary material associated with the cloud. The core envelope appears to be located in correspondence of the merger of these filamentary structures.

- We see a velocity gradient along the filament in the DCO^+ (3-2) gas. Therefore, we measured the ongoing accretion material toward the protostar core in this gas, $\dot{M}_{acc} =$

$9.7 \times 10^{-7} M_{\odot} yr^{-1}$, where the accretion rate is expected to be accurate within a factor of 2.

- The mean velocity gradient is roughly 5.1 $km\,s^{-1}$ pc^{-1} measured in DCO^+ (3-2) around the protostar core, which is linked to the rotation of the core. This velocity gradient at the position of the protostar is in the east–west direction, oriented approximately perpendicular to the bipolar outflow previously found.

- Line widths of DCO^+ (3-2) increase toward the position of the protostar, probably due to protostellar feedback.

- We observed a velocity shift between neutral and ionized species. A higher velocity is always present in the $C^{18}O$ (2-1) data compared to the DCO^+ (3-2) data. The mean velocity difference, $V_{lsr}(C^{18}O)$ - $V_{lsr}(DCO^+)$, is equal to 0.13 $km\,s^{-1}$ across the full filament. This is consistent with a model of collision between filaments that is still ongoing. The velocity shift between the $C^{18}O$ (2-1) and DCO^+ (3-2) illustrates the relative motion of the dense gas, traced by DCO^+ (3-2), and the surrounding less dense envelope, traced by $C^{18}O$ (2-1).

Further observational investigations are needed to determine in more detail the connections within the kinematics and magnetic field in this source.

Acknowledgements Elena Redaelli acknowledges the support from the Minerva Fast Track Program of the Max Planck Society. The authors would like to thank Jaime Pineda Fornerod for his support and discussion about the code to calculate the velocity gradient. This research has made use of data from the Herschel Gould Belt survey (HGBS) project (http://gouldbelt-herschel.cea.fr). The HGBS is a Herschel Key Programme jointly carried out by SPIRE Specialist Astronomy Group 3 (SAG 3), scientists of several institutes in the PACS Consortium (CEA Saclay, INAF-IFSI Rome, and INAF-Arcetri, KU Leuven, MPIA Heidelberg), and scientists of the Herschel Science Center (HSC)(André et al., 2010a).

Chapter 3

Unveiling the role of magnetic fields in a filament accreting onto a young protocluster

The contents of this chapter were published in Astronomy & Astrophysics. Credit: Tabatabaei et al., A&A, 688, A98, 2024

3.1 Introduction

The process of low-mass star formation is initiated by the fragmentation of molecular clouds into cold, dense cores. These cores are usually identified by subsonic gas motions, in contrast with the supersonic turbulence of their surrounding clouds (Goodman et al. 1998). The formation of a protostar is determined by a competition between gravity, thermal pressure, external pressure, and magnetic field strength. The precise role of the magnetic field (B-field) in the star formation process is still controversial, highlighting the importance of studying the configuration of B-field lines in regions where stars are formed.

According to *Planck* data analysis, clouds are generally magnetized (Planck Collaboration et al. 2016b). The B-field tends to be aligned parallel to the density structures for visual extinction (A_V) values less than or equal to $2 - 3.5$ mag. However, beyond this A_V threshold, the B-field orientation becomes perpendicular to the density structures (Soler et al. 2017a; Planck Collaboration et al. 2016b). Studies show that the B-field may take on a pinched morphology perpendicular to the long axis of the filament (e.g., Tomisaka 2015; Burge et al. 2016). For example, higher-resolution observations strongly indicate a significant pinch of the B-field inside the filament of NGC 1333 (Doi et al. 2021).

In the low-mass star formation regime, pre-stellar cores are the dense cores where star formation is about to take place (i.e., prior to the formation of a protostar in the center), and they are embedded in larger structures that often exhibit filamentary shapes. The origin of these filamentary structures is still debated. Two main hypotheses have been proposed to explain their formation. The first suggests that filaments are formed due to compressions in turbulent clouds (Padoan et al. 2001 and Auddy et al. 2016). The second proposes that filaments arise from the global gravitational collapse of a molecular cloud as a whole, and consequently, filaments accrete material from their parent clouds and feed it into the bottom of the potential well (Heitsch 2013a, Heitsch 2013b, and Hennebelle & André 2013).

Observational evidence suggests that there are organized gas flows along filaments toward the cores in both high-mass and low-mass star-forming regions (see Henshaw et al. 2013b for an example of filamentary structure in high-mass star-forming regions and Hacar et al. 2013 for low-mass star-forming regions). This is supported by studies by Kirk et al. (2013) of gas flows along the southern filament of the Serpens South embedded cluster (see also Peretto et al. 2014). To gain a better understanding of star formation, it is crucial to comprehend the physical relationship between cores and the filaments they are associated with.

The Pipe Nebula, located at a distance of $d_{\rm cloud}$ = 163 pc (Dzib et al. 2018b), is one of the closest known star-forming regions. The star formation rate within the Pipe cloud is notably low (only ∼0.06% efficiency; Forbrich et al. 2009). Lombardi et al. (2006) identified 159 dense cores across the Pipe Nebula, each with estimated masses ranging from 0.5 to 28 $M_\odot$. However, it appears that the only area within this cloud where star formation is currently taking place is limited to its northwestern extreme, known as Barnard 59 (hereafter B59; Brooke et al. 2007; Forbrich et al. 2009; Forbrich et al. 2010). B59 contains a young protocluster with approximately 20 young stellar objects (Brooke et al. 2007, Redaelli et al. 2017).

Alves et al. (2008) and Franco et al. (2010) proposed that the magnetic properties of the Pipe Nebula may be responsible for the fact that only B59 has active star formation. Studies of the morphology of the B-field with optical polarimetric observations revealed the filamentary structure to be threaded by a B-field, aligned perpendicular to the cloud's axis, that is possibly preventing or slowing down its global collapse (Alves et al. 2008; Franco et al. 2010).

As Peretto et al. (2012) suggested, B59 is located in the center of what resembles a hub-like clump with apparently converging filaments. Nevertheless, from the kinematics of the region, Duarte-Cabral et al. (2012) determined that a significant fraction of the filaments around the B59 clump are shaped by the outflows of the forming protocluster pushing the cloud material, rather than by infalling filaments of gas. The one clear exception is the filament to the northeast of the clump, which is the target of this work. This filament, although situated in the immediate vicinity of the B59 star-forming clump, is relatively isolated and seems to be extremely quiescent (Fig. 3.1). As such, it is a good candidate for our modeling (see Sect. 3.5).

This paper is organized as follows. In Sect. 3.2 we present the data collected from different telescopes and describe how we processed them. In Sect. 3.3 we explain how we analyzed the data and discuss our results in terms of the kinematic properties of the filament. In Sect. 3.4 we discuss the polarization and B-field properties through the filament, and lastly, we present our modeling of a hydrostatic filamentary cloud based on our observational parameters of the filament within B59 in Sect. 3.5. Our main findings

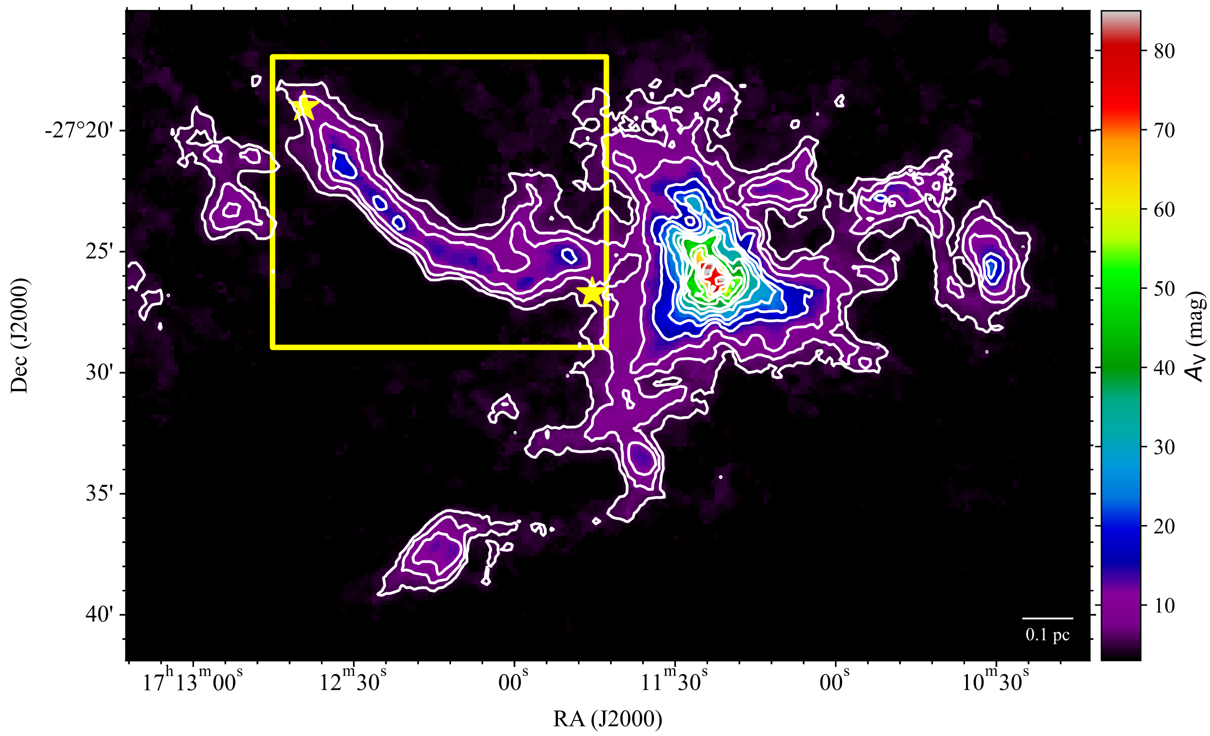

Figure 3.1: Dust extinction map of the B59 region at a spatial resolution of 20″ (Román-Zúñiga et al. 2010). The solid white line contours represent levels of visual extinction at $A_V = [5, 7, 10, 15, 20, 25, 30, 35, 40, 50, 60, 70, 80, 90]$ mag. The yellow square marks the filament studied in this work. Two yellow stars indicate the approximate length of the filament. The scale bar is at the bottom right side of the panel.

and conclusions are summarized in Sect. 3.6.

3.2 Observations

3.2.1 Near-infrared observations

The polarimetric data were obtained at Observatório do Pico dos Dias/Laboratório Nacional de Astrofísica (OPD/LNA, Brazil) using IAGPOL, the IAG imaging polarimeter mounted on the 1.6 m telescope. Observation runs were completed in June 2013. A special infrared (IR) detector was used to collect these data for polarimetric measurements. A precise description of the polarimeter is provided in Magalhaes et al. (1996). We obtained linear polarimetry in the H band using deep imaging for three fields, each with a 4′ by 4′ field of view. The images were obtained with an IR camera, CamIV, which has a HAWAII detector of 1024 by 1024 pixels and 18.5 μm/pixel, resulting in a plate scale of 0.25″/pixel. For each of the eight waveplate positions separated by 22.5°, sixty dithered images were obtained following a five-dot pattern (12 by 5 positions). Each image was exposed for

10 seconds, adding up to 600 seconds per wave-plate position. Observations of polarized standard stars were used to determine the reference direction of the polarizer.

From the Stokes Q and U, we derived degree to the linear polarization, $P = \sqrt{Q^2 + U^2}$ and the polarization angle, $\theta_{\rm p} = 0.5\tan^{-1}(U/Q)$. Assuming that the polarization is produced by magnetically aligned dust grains, we show polarization segments that outline the direction of the B-field in all the figures. Since near-infrared (NIR) polarization is produced by dichroic extinction, polarization segments give the B-field direction directly. The data are filtered by a $P/\sigma_{\rm P} \geq 3$ where correspond to an uncertainty in θ ($\sigma_\theta < 10°$) and $\sigma_{\rm P}$ represents the standard deviation of the measurement. The data are length-scaled by the polarization degree, with the longest vectors with $\sim 3\%$ polarization and a mean value of $\sim$1% (segments in Fig. 3.2 and Fig. 3.4).

Our analysis of gas column density and dust temperature is based on data from the Gould Belt Survey obtained with the *Herschel* Space Telescope (SPIRE/PACS instrument; Peretto et al. 2012, Roy et al. 2014b). We utilized the visual extinction map created from a deep near-infrared (NIR) imaging survey conducted with various telescopes, including the New Technology Telescope (NTT), the Very Large Telescope (VLT), and the 3.5-meter telescope at the Centro Astronómico Hispano Alemán (CAHA) as well as 2MASS data (Román-Zúñiga et al. 2010, Fig. 3.1).

3.2.2 *James Clerk Maxwell* Telescope

The molecular line data used in this work are presented in Duarte-Cabral et al. (2012), where a detailed description of the observations and data reduction can be found. In brief, here we use the maps of ^{13}CO (3-2) and C^{18}O (3-2) at 330.6 and 329.3 GHz, respectively, covering the entire B59 star-forming region (~ 0.11 deg^2). The data were obtained from the *James Clerk Maxwell* Telescope (JCMT) using HARP (Buckle et al. 2009) in May and June 2010. This dataset contains an rms noise level of 0.22 K (in $T_{\rm A}^{\star}$) with 0.25 km s^{-1} channels. The main beam efficiency of the telescope ($\eta_{\rm mb} = 0.66$) was taken into account for all data (Buckle et al. 2009; Curtis et al. 2010)

3.3 Kinematical analysis of the filament

To interpret the gas kinematic behavior in the filament, we estimated the centroid velocity ($V_{\rm lsr}$) and velocity dispersion ($\sigma_{\rm v}$) by fitting a single Gaussian profile to the C^{18}O and ^{13}CO line emission, using the Python package *pyspeckit* (Ginsburg & Mirocha 2011b). All fitted spectra have residuals of less than 2 × rms and widths of less than 0.35 km s^{-1}. Almost all spectra with S/N > 3.5 for C^{18}O and S/N > 4.5 for ^{13}CO are well fitted using only one Gaussian, as seen in Fig. 3.3, as proved by the low residuals (see Appendix B.1). As a result, and for simplicity, we adopted the single-velocity component fit for the whole filament. The best-fit parameters of $V_{\rm lsr}$ and $\sigma_{\rm v}$ are shown in Fig. 3.2. The $V_{\rm lsr}$ map of C^{18}O shows the velocity gradient of gas toward the location of the hub, ranging from 3.3 km s^{-1} to 3.6 km s^{-1}. To estimate the velocity gradient, we determined an approximate

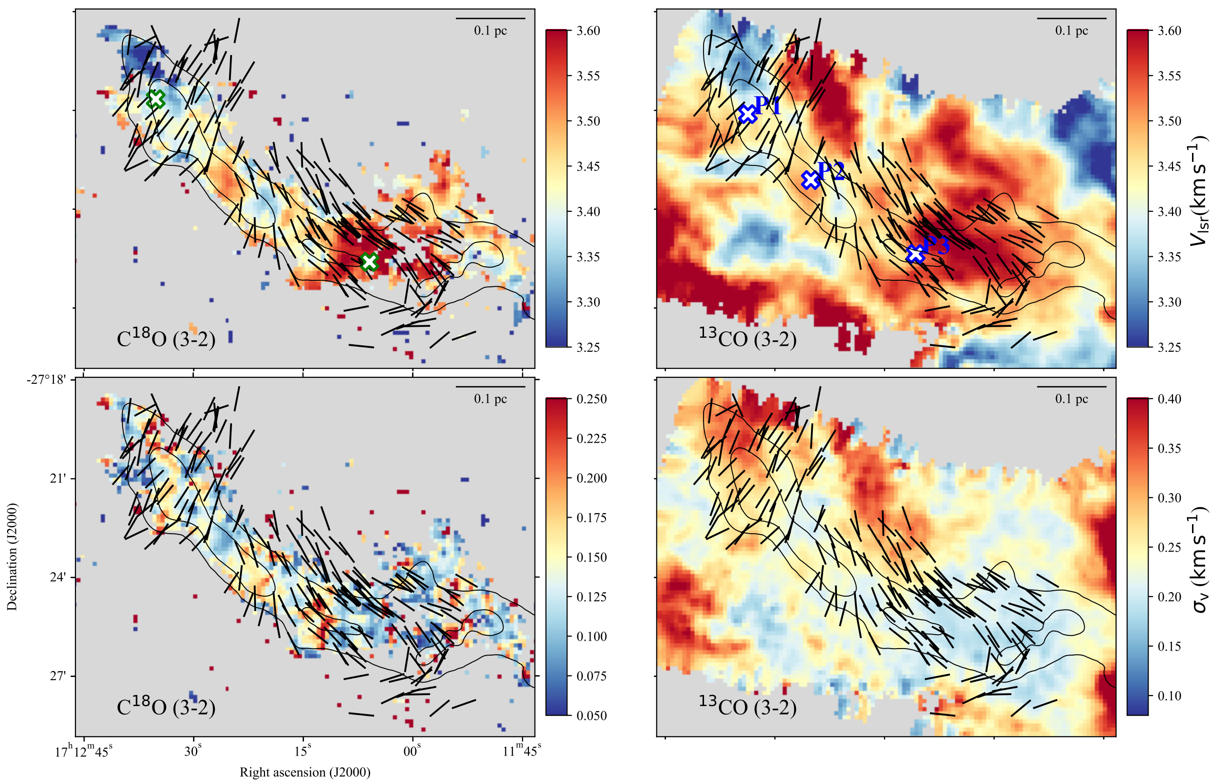

Figure 3.2: Maps of kinematic parameters. Top panels: Centroid velocity maps of ^{13}CO (3-2) and C^{18}O (3-2) obtained from the Gaussian fitting procedure described in Sect. 3.3, Bottom panels: Velocity dispersion maps of ^{13}CO and C^{18}O. Contours show the column density of H_2 with levels [4,6] $\times 10^{22}$ cm^{-2}, as derived from *Herschel* data (Peretto et al. 2012). The black segments represent the polarization angles in the NIR band. The blue crosses in the top-right panel present the locations of spectra in Fig. 3.3. The green crosses represent the locations where the velocity gradient is estimated. Scale bars are at the top right of each panel.

estimate of two positions at a distance of $\Delta R \sim 0.4$ pc (see the green crosses in Fig. 3.2). Therefore, the velocity gradient for C^{18}O is $\nabla V = \Delta V/\Delta R = 0.69{\pm}0.01$ km s^{-1} pc^{-1}. This value is comparable with that of a smaller filament, ~ 0.1 pc, in Lupus I. In comparison, Tabatabaei et al. (2023) report $\nabla V = 0.9 \pm 0.2$ km s^{-1} pc^{-1} for a filament associated with a low-mass Class 0 stellar object IRAS15398-3359.

3.3.1 Velocity dispersion and nonthermal motions

The total observed broadening of any optically thin line profile is the sum of the contributions of thermal and nonthermal motions. We can obtain some insight into the gas kinematics properties by comparing the thermal sound speed with the Gaussian velocity dispersion.

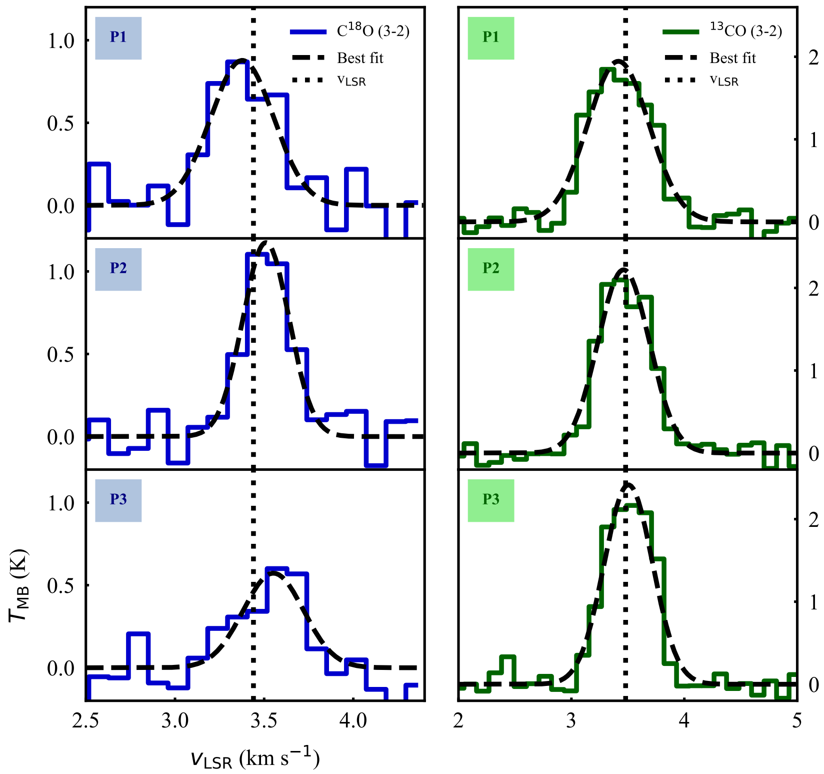

Figure 3.3: $C^{18}O$ (3-2) and ^{13}CO (3-2) spectra at three selected locations within the filament (locations are shown with blue crosses in Fig. 3.2). $C^{18}O$ (3-2) spectra are in the left column, and ^{13}CO (3-2) spectra are in the right column. Blue and green lines show the observed spectra for the $C^{18}O$ and ^{13}CO, respectively, whereas dashed black curves show the best-fit Gaussian for each. As displayed by the vertical dotted lines, $C^{18}O$ (3-2) and ^{13}CO (3-2) have average $V_{\rm lsr}$ of 3.4 and 3.5 km s^{-1}, respectively.

To estimate nonthermal velocity dispersion, we subtracted the thermal velocity dispersion from the observed velocity dispersion in quadrature:

$$\sigma_{\rm nt} = \sqrt{\sigma_{\rm obs}^2 - \sigma_{\rm th}^2}, \tag{3.1}$$

where $\sigma_{\rm obs}$ is equal to $\sigma_{\rm v}$ (see Sect. 3.3). We used the mean value of $\sigma_{\rm v}$ for the filament area as defined by $A_{\rm V} > 8$ mag. The thermal velocity dispersion is

$$\sigma_{\rm th} = \sqrt{\frac{k_{\rm B} T_{\rm kin}}{m_{\rm obs}}}, \tag{3.2}$$

where $T_{\rm kin}$ is the kinetic temperature of the gas, $k_{\rm B}$ is Boltzmann constant and $m_{\rm obs}$ is the mass of observed molecule. Hence, the effect of $\sigma_{\rm nt}$ is quantified by the turbulent Mach number, which is calculated as the ratio of nonthermal dispersion to isothermal sound speed $\mathcal{M} = \sigma_{\rm nt}/c_{\rm s}$. The isothermal sound speed was obtained from

$$c_{\rm s} = \sqrt{\frac{k_{\rm B}T_{\rm kin}}{\mu m_{\rm H}}}, \tag{3.3}$$

where $\mu = 2.37$ (Kauffmann et al. 2008) is the mean molecular weight per free particle and $m_{\rm H}$ is the mass of the hydrogen atom. We used the dust temperature, $T_{\rm d}$, as a proxy for the gas kinetic temperature. We obtain $T_{\rm d} = 14$ K from the *Herschel* map. We obtain $c_{\rm s} = 0.2$ km s^{-1} and the corresponding $\sigma_{\rm nt}$ are 0.12 ± 0.02 km s^{-1} and 0.22 ± 0.01 km s^{-1} for $C^{18}O$ and ^{13}CO, respectively. For this filament, Duarte-Cabral et al. (2012) estimated an excitation temperature of 9 K for ^{13}CO. The thermal velocity dispersion, $\sigma_{\rm th}$, is reduced by $\sim 20\%$ when $T_{\rm kin} = 9$ K is used in Eq.3.2. According to the $C^{18}O$ data, nonthermal motions are subsonic ($\mathcal{M} = 0.54 < 1$). This suggests that the filamentary cloud is in a quiescent state where the nonthermal gas motions are smaller than the sound speed. We highlight that for this filament, for the ^{13}CO emission, we obtain $\mathcal{M} = 1.0$, implying that the gas motions are transonic. The difference between the Mach number of these two molecules comes from the difference in their velocity dispersion. The emission of ^{13}CO traces the lower-density gas, which is more turbulent and likely to be affected by larger optical depth, causing more line broadening than for the $C^{18}O$ lines.

3.3.2 Mass per unit length

From a theoretical point of view, a self-gravitating isothermal cylinder has an infinite radius but a finite mass per unit length. The critical value of this parameter at 10 K is

$$\left(\frac{M}{L}\right)_{\rm cr} = \frac{2c_{\rm s}^2}{G} = 16 \left(\frac{T}{10{\rm K}}\right) {\rm M}_\odot\ {\rm pc}^{-1}, \tag{3.4}$$

where G is the gravitational constant $M_\odot$ and is the mass of the sun. If $\left(\frac{M}{L}\right)_{\rm fil} > \left(\frac{M}{L}\right)_{\rm cr}$, the filament collapses radially. To estimate the filament mass, we used

$$M_{\rm fil} = A \times \sum_{i=1}^{n} \left(\frac{N({\rm H_2})}{{\rm cm}^{-2}}\right)_i \left(\frac{\theta}{''}\right)^2 \left(\frac{d_{\rm cloud}}{\rm pc}\right)^2 \mu_{\rm H_2}\, m_{\rm H}\, M_\odot, \tag{3.5}$$

where $\sum_{i=1}^{n}(N({\rm H_2})_i)$ adds the contribution of n pixels within the area of the filament selected with $A_{\rm V} > 8$ mag, $m_{\rm H} = 1.67 \times 10^{-24}$ g is the hydrogen mass, $\mu_{\rm H_2} = 2.8$ (from Kauffmann et al. 2008) is the gas mean molecular weight per hydrogen molecule, $d_{\rm cloud}$ is the distance to the cloud, $A = 1.13 \times 10^{-7}$ is a numerical factor to adjust units, and θ is the pixel size. In our case, $d_{\rm cloud} = 163$ pc and $\theta = 7.28''$. We obtained the gas column density of the filament, $N({\rm H_2})$, in two ways. First, we used the visual extinction, $A_{\rm V}$, a parameter that can be converted into molecular hydrogen column density using Bohlin et al. (1978)'s relation, $N({\rm H_2}) = 9.4 \times 10^{20} \times A_{\rm V}$ cm^{-2} mag^{-1}. We also obtained $N({\rm H_2})$ from the *Herschel* map for the same exact area of the filament that was selected for the

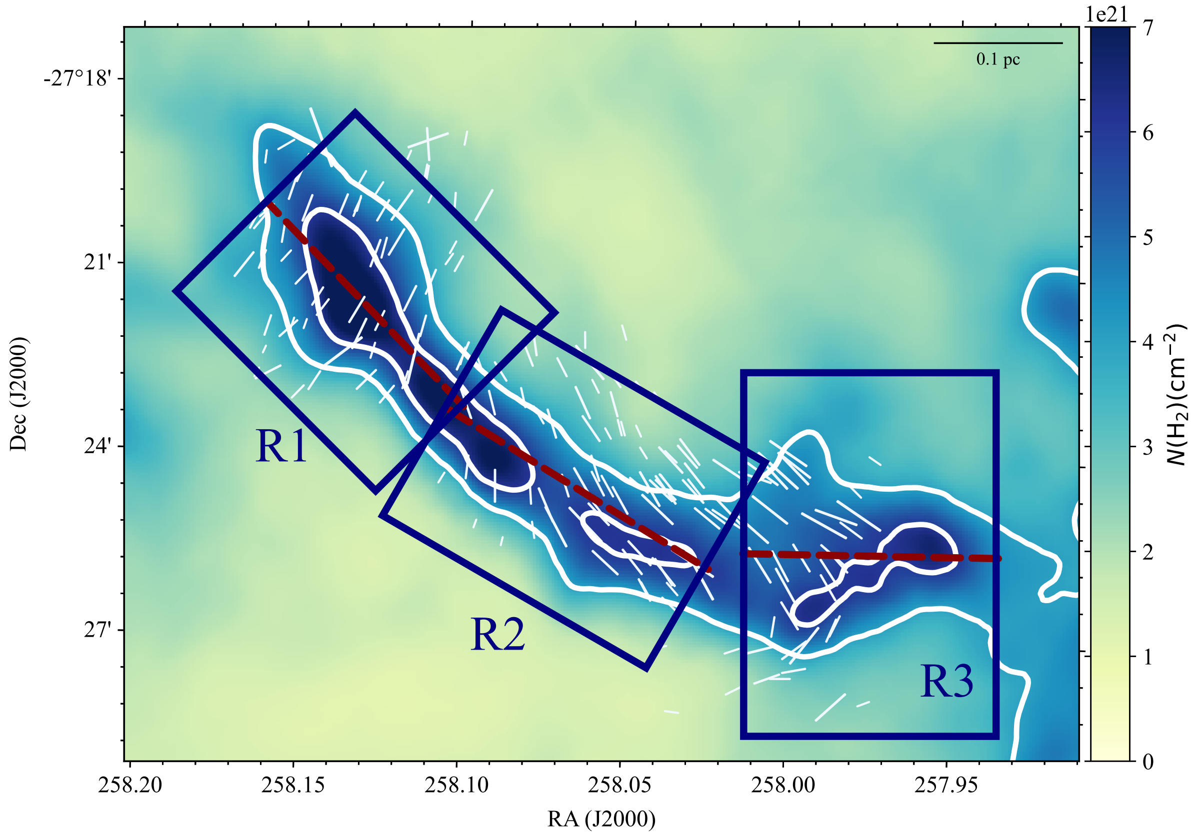

Figure 3.4: The column density map of the filament in B59 (from *Herschel* data) overlaid with the polarization segments from Pico dos Dias Observatory. The blue rectangles divide the filament into three regions labeled R1, R2, and R3. The red dashed lines represent the axis of each region. Contours show column density of H_2 with levels: [4,6] $\times 10^{22}$ cm^{-2}. The scale bar is on the top right side of the panel.

extinction map in the previous method. As a result, the mass calculated based on *Herschel* column density[1], $M_{\rm Herschel}$, and the mass calculated from the extinction map, $M_{\rm Ext}$, are 6.7 $M_\odot$ and 12.2 $M_\odot$, respectively. The resultant uncertainty is $\sim$ 42% (Tabatabaei et al. 2023, Roy et al. 2014b, Dzib et al. 2018b) and $\sim$ 11.7% (Román-Zúñiga et al. 2010) for $M_{\rm Herschel}$ and $M_{\rm Ext}$, respectively. The two values are consistent at 3σ level. We estimate $L \sim 0.7$ pc for the filament length, which corresponds to the distance between the two yellow stars in Fig. 3.1. We adopted both $M \sim 6.7$ $M_\odot$ and 12.2 $M_\odot$ of the filament to obtain the observational value of the mass per unit length. Table 3.1 shows the critical and observation values for the whole filament.

In Sect. 3.5 we discuss the stability of the filament based on the cylindrical polytropic

[1]The column density map was constructed via pixel-by-pixel gray-body fitting from 160 μm to 500 μm, fixing the dust opacity such that $\kappa_\lambda = 0.1 \times \left(\frac{\lambda}{300\mu m}\right)^{-2}$ cm^{2}g^{-1}; for more details, see Roy et al. (2014b).

hydrostatic models by Toci & Galli (2015a, hereafter TCa), and Toci & Galli (2015b, hereafter TCb). We also calculated the mass per unit length for different polytropic indexes of the cylindrical model. The mass per unit length is lower than the critical value for the whole filament in all the analyses (see Table 3.1), indicating that the filament is stable.

Table 3.1: Values of mass per unit length for the filament.

	cr	$\mathrm{obs}^{(a)}_{\mathrm{Herschel}}$	$\mathrm{obs}^{(b)}_{\mathrm{Ext}}$	Region	$n^{(c)} = -1$	$n = -2$	$n = -3$	$n = -4$
M/L ($\mathrm{M}_\odot$/pc)	22.4	9.6	17.4	R1	17.8	9.8	6.3	4.4
M/L ($\mathrm{M}_\odot$/pc)	22.4	9.6	17.4	R2	15.1	8.7	5.7	4.0

Note: The columns labeled cr, $\mathrm{obs}_{\mathrm{Herschel}}$, and $\mathrm{obs}_{\mathrm{Ext}}$ contain values corresponding to the whole filament region. $^{(a)}$ $\mathrm{obs}_{\mathrm{Herschel}}$ is the mass per unit length value obtained from mass of filament calculated from *Herschel* $N(\mathrm{H}_2)$ and $^{(b)}$ $\mathrm{obs}_{\mathrm{Ext}}$ is from the mass of filament calculated with A_{V} (see Sect. 3.3.2). $^{(c)}$ n is the polytropic index; see Sect. 3.5.

3.4 Polarization and magnetic field properties of the filament

We divided the filament area into three regions, R1, R2, and R3, as shown in Fig. 3.4. Although they belong to the same filament, each region has distinct polarimetric characteristics. Our method involves cutting the filament into three parts in which the B-field is approximately uniform in direction, as well as doing the cuts perpendicular to the filament's spine for each region (see the dashed red lines in Fig. 3.4). It is worth noting that the angles of the spine for the R1, R2, and R3 regions are precisely 45°, 60°, and 90°, respectively, from the north to the east. This allowed us to approximate the three regions as cylinders to which we can apply the model described in Sect. 3.5. A detailed analysis of the distribution of the observed polarization angle as a function of Right Ascension over the core filament is presented in Fig. 3.5. The distribution of polarization angles is rather complex. In region R1, we see a distribution of polarization angles ranging from $\sim$ 120° to 170°, which tends to concentrate around 149°± 20°(mean position angle ± standard deviation, dashed green line). All angles are measured from north to east. In region R2 in Fig. 3.5, we can see that polarization angles range from $\sim$ -30° to 60° with a mean value of 34°±19°(dashed red line). In the small region southeast of the filament, region R3 (blue dots in Fig. 3.5), we obtain a wide range of polarization angles, 30° to 170° with a mean value of 75°± 38°. We present the 1σ interval around the mean as two vertical gray lines in the bottom panel of Fig. 3.5. This analysis shows two sharp changes in the B-field orientation: the first change from R1 to R2 and another one inside of R3, the second presenting a U-shaped B-field where the filament is close to connecting to the core region. These properties are more clearly illustrated in the histograms shown in Fig. 3.5, where

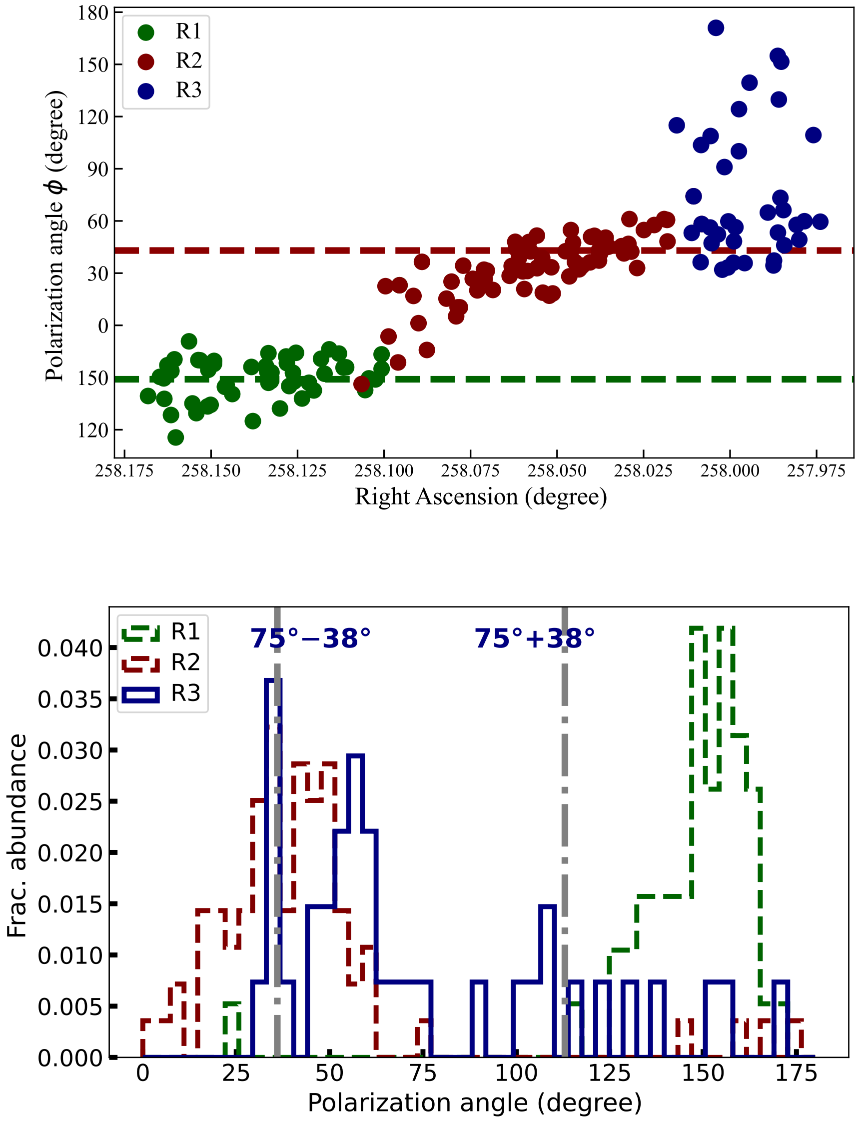

Figure 3.5: Distribution of polarization angles. Top panel: Distribution of polarization angles as a function of the right ascension of the field. Dashed green and red lines show the mean polarization angle values for R1 and R2, 147°, and 43°, respectively. bottom panel: Histogram of the distribution of magnetic polarization angles. Green, red, and blue data points refer to R1, R2, and R3, respectively. Gray dash-dot lines illustrate the 1σ interval around the mean for region R3.

two distributions of polarization angles are visible as two peaks. In the top panel of Fig. 3.5 a curved structure can be observed from the R2 region to the R3 region, where the position angle increases as the RA decreases. The curvy structure of the filament likely causes it and tracks the change in the direction of the filament. The change in the B-field orientation from perpendicular to the filament spine in the eastern region to parallel toward the west, where this dense filament connects to the hub, suggests a coupled evolution of the B-field and the filament. The reorganization of the B-field along filaments could be caused by local velocity flows of matter in-falling toward the hubs, where the B-field is dragged by gravity and flows along the filaments, which is also observed in magnetohydrodynamic (MHD) simulations (e.g., Gómez et al. 2018). Pillai et al. (2020b) studied the Serpens hub-filament with polarimetric data from NIR and terahertz regimes. They found that the transition in relative orientations between the B-field and the filament elongation at about $A_\mathrm{V} = 21$ mag. Those authors claim that this configuration results from the B-field lines being dragged by the infalling material, feeding the central hub. To determine the relation between kinematics and the magnetic direction of the filament (especially the bending part of the B direction), further observations of $C^{18}O$ with better sensitivity and spectral resolution are needed.

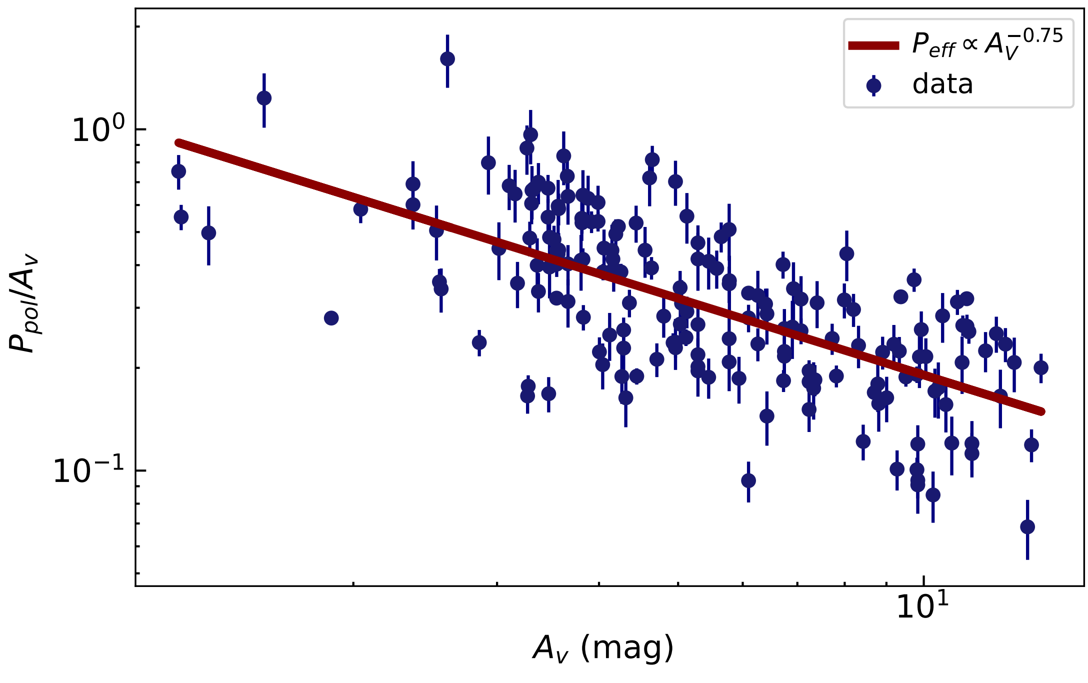

Figure 3.6: Scatter plots of the polarization efficiency ($P_\mathrm{pol}/A_\mathrm{V}$) as a function of the visual extinction (A_V) in magnitudes in logarithmic scale. Measurement uncertainties are displayed as an error bar for each data point. The solid line is the best fit for the dataset, as explained in the main text. The best fit is shown in the top-right corner.

Figure 3.6 shows the scatter plot of the polarization efficiency, which is described as the polarized fraction normalized by the visual extinction ($P_\mathrm{eff} = P_\mathrm{pol}/A_\mathrm{V}$), as a function of visual extinction (A_V) in log-log space. As a result of fitting a linear relationship between P_{pol}/A_V and A_V (red curve in Fig. 3.6), we obtain the slope of the relation $P_{eff} \propto A_V^{-\alpha}$ (see Fig. 3.6; the error bars on each data points are calculated from the least square solution).

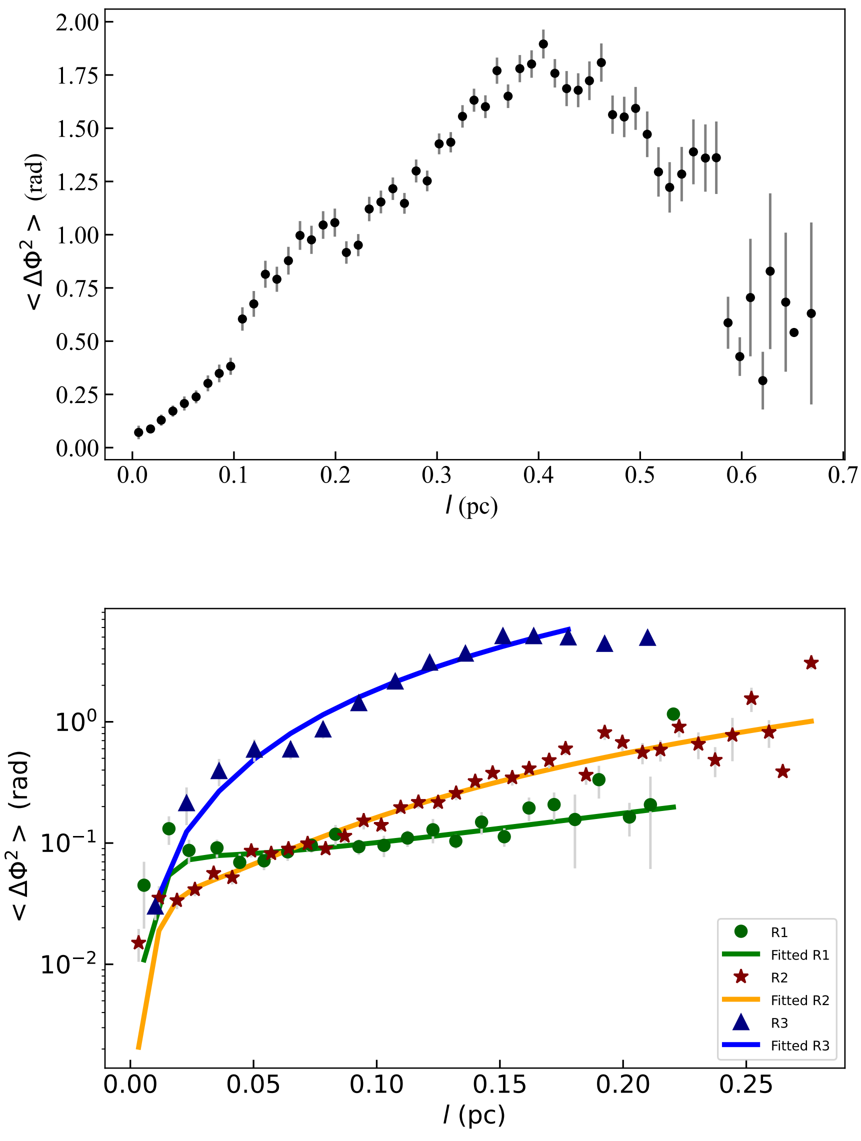

Figure 3.7: ADF versus distance, l. Top panel: ADF for the whole filament. Bottom panel: Same but for the three filament regions. The best fits to the data points using Eq. (3.9) for R1, R2, and R3 are shown with the green, orange, and blue curves, respectively. Measurement uncertainties are displayed as error bars, which are not visible for small values of l due to the higher statistics.

For our NIR data, we find a slope of $\alpha = 0.75 \pm 0.07$, which is consistent with radiative torque alignment (Lazarian & Hoang 2007a) theory and previous studies. According to Alves et al. (2014a), for NIR polarization, the values of α in the starless object Pipe-109 in the Pipe Nebula are 1 and 0.34 for $A_V < 9.5$ mag and $A_V > 9.5$ mag, respectively. Redaelli et al. (2019c) calculated a very steep slope, $\alpha = 1.21$, for far-infrared (FIR) polarization data on the protostellar core IRAS 15398-3359. These slopes indicate depolarization at high column densities. Consequently, if dust grains are aligned by radiative torque originating from the interstellar radiation field at higher visual extinction, less radiation penetrates the cloud, and, therefore, grain alignment is less efficient. In addition, the dust grain size distribution has a great impact on alignment efficiency (Brauer et al. 2016; Pelkonen et al. 2009).

3.4.1 Dispersion of polarization angles and the magnetic field strength

Various methods have been proposed to estimate the B-field strength from dust polarization data. According to Davis (1951) and Chandrasekhar & Fermi (1953), hereafter DCF, the kinetic energy of turbulent motions is equal to the fluctuating magnetic energy density:

$$\frac{1}{2}\,\rho\,\delta v^2 = \frac{\delta B^2}{8\pi}, \tag{3.6}$$

The mean B-field (B_0) is

$$B_0 = \sqrt{\frac{4\pi\rho}{3}}\frac{\delta v}{\delta\theta}, \tag{3.7}$$

where ρ is the gas density, δv is the velocity dispersion, and $\delta\theta$ is the dispersion of the polarization angle equal to the ratio of the turbulent B-field over the mean B-field ($\delta\theta = \delta B/B_0$). Hildebrand et al. (2009) and Houde et al. (2009) developed the angular dispersion function (ADF) approach as an alternative way to estimate the $\delta B/B_0$ ratio (known as the HH09 method). The method was formulated to eliminate inaccurate estimates of the B-field generated by factors other than MHD waves, such as large-scale bending caused by differential rotation and gravity. We calculated the autocorrelation function of the position angles, $\Delta\Phi$. This refers to the variation in angle between every pair of vectors separated by a distance of l (see Houde et al. 2009),

$$\langle\Delta\Phi^2(l)\rangle = \frac{1}{N}\sum_{i=1}^{N}[\Phi(x) - \Phi(x+l)]^2, \tag{3.8}$$

which results in the following analytical relation,

$$\begin{aligned}\langle\Delta\Phi^2(l)\rangle = 2\sqrt{2\pi}\left(\frac{\delta B}{B_0}\right)^2 &\frac{\delta^3}{(\delta^2+2W^2)\Delta'} \\ \times &\left[1-\exp\left(-\frac{l^2}{2(\delta^2+2W^2)}\right)\right] + m^2 l^2,\end{aligned} \tag{3.9}$$

where m is a constant related to the large-scale structure of the B-field and is not influenced by turbulence, Δ' is the effective cloud depth, and W is the telescope beam size. This relationship only applies to spatial scales $\delta \leq l \leq d$, where δ represents the correlation length of the turbulent B-field (δB), and d represents the highest distance at which B_0 remains uniform. The effective angular resolution of absorption dust polarization data is treated as zero (Franco et al. 2010). As a result, the angular resolution term in the equation is $W = 0$. To obtain $\delta B/B_0$ by fitting Eq. (3.9), we calculated $\Delta\Phi^2(l)$ for all available pairs of points. The spatial scale, l, is divided into 24, 38, and 16 bins corresponding to $\sim$ 0.009 pc, 0.007 pc, and 0.013 pc for the R1, R2, and R3 regions, respectively. The values of the parameters $\Delta' = 0.1$ pc and $\delta = 10$ mpc that were used in Eq. (3.9) are obtained from Franco et al. (2010). They employed $\Delta' = 0.3$ pc for the whole region of B59, but since we only focused on the filament area, and each part of the filament has the length of $\sim$ 0.1-0.3 pc, we used $\Delta' = 0.1$ pc. A $\Delta' = 0.3$ pc will decrease the magnetic strengths on the plane of the sky (PoS) ($B_{\rm pos}$) of each region by $\sim 24\%$ ($B_{\rm pos}$ values in Table 3.2).

By employing the Scipy package, specifically using the scipy.optimize.curve_fit module with least squares optimization, we found the best-fit solution of Eq. (3.9) in the three regions along with their associated errors, by leveraging the standard deviation of the fitted parameters obtained from the covariance matrix returned by the curve_fit function. We estimated the strength of the B-field in each region (see Table 3.2) using a further expansion of Eq. (3.7) (which is valid if $\delta\phi < 25°$; Crutcher 2012a):

$$B_{\rm pos} = \sqrt{4\pi\, \mu_{\rm H_2}\, m_{\rm H}\, n_{\rm H_2}}\frac{\delta v}{\delta\theta}, \tag{3.10}$$

where $m_{\rm H}$ is the hydrogen mass, $\mu_{\rm H_2}$ is the gas mean molecular weight per hydrogen molecule, and $n_{\rm H_2}$ is the gas volume density. We employed the $n_{\rm H_2} = 3 \times 10^3\,{\rm cm}^{-3}$ from Alves et al. (2008). They evaluated the gas volume density associated with the optical polarization in the different parts of the Pipe Nebula region. We computed the gas velocity dispersion by fitting one Gaussian profile to the $C^{18}O$(3-2) molecular line, obtaining the mean value of $\delta v = 0.14 \pm 0.02$ km s^{-1} in the filament region (see Sect. 3.3).

We calculated these parameters for all pairs of data points, obtaining the results shown in Fig. 3.7 (top panel). Our scatter plot does not show the expected increase in the ADF with distance l. In fact, due to the sampling of the data, we see peaks in the profile of the ADF. The entire field of view was sampled at 0.08 degrees per tile, equivalent to 0.2 pc, which corresponds to a peak every $\sim$ 0.2 pc in Fig. 3.7, top panel (see Soler et al. 2016 for more details on this effect). To reduce these spurious effects, we did our calculation for each region separately, obtaining the fit parameters for every region of the filament (see Fig.3.7, bottom panel). It is evident that the distribution of $\Delta\Phi^2$ along the filament follows a clear trend. In Fig. 3.7 the R3 region has a steeper slope compared to other regions. A steep slope is evidence that the B-field orientation in the plane of the sky changes significantly. As the slope increases from R1 to R3, the dispersion of position angles becomes larger. Table 3.2 shows the best-fit parameters for Eq. (3.9) and the plane of the sky magnitudes of the B-field for each region. The B-field strength increases from R1 to R3 (see the fourth column of Table 3.2), ranging from 151 to 234 μG.

Table 3.2: Physical parameters for the three regions of the filament from Eq. (3.9).

Region	$\delta B/B_0$	m [rad/pc]	$B_{\rm pos}$ [μG]	$B^{*(a)}_{\rm pos}$ [μG]	$N(H_2)$[cm^{-2}]	$\lambda^{(b)}$
R1	0.39 ± 0.02	1.6 ± 0.2	151 ± 6	66 ± 1	4.1×10^{21}	0.27 ± 0.04
R2	0.26 ± 0.01	3.57 ± 0.06	222 ± 9	80 ± 1	3.9×10^{21}	0.13 ± 0.02
R3	0.25 ± 0.06	13.5 ± 0.2	234 ± 6	83 ± 8	3.9×10^{21}	0.13 ± 0.02

Note: $^{(a)}$ $B^*_{\rm pos}$ is the B-field strength calculated from Skalidis & Tassis (2021). $^{(b)}$ λ is cloud stability; see Sect. 3.4.3. In all computations, we considered $\delta = 10$ mpc, obtained from Franco et al. (2010).

3.4.2 The influence of assumed parameters and used methods

The previous analysis relied on specific key parameters. In this section we examine if altering these assumptions can influence our findings. Specifically, the initial focus is be on the turbulence correlation scale, δ. For the calculation in Sect. 3.4.1, we used $\delta = 10$ mpc, considering that Franco et al. (2010) reported a turbulence correlation scale of a few milliparsecs for the Pipe nebula. The values found align well with previous estimates of this parameter in other areas where star formation occurs. For example, Coudé et al. (2019) measured a value of $\delta = 7$ mpc in the Barnard 1 region. In contrast, in the high-mass star-forming region NGC 7538, Frau et al. (2014) calculated a range of values for δ between 13 and 33 mpc, and Redaelli et al. (2019c) investigated four values of 5, 10, 15, and 20 mpc for IRAS 15398-3359, showing an increase in the B-field by increasing δ. We therefore used Eq. (3.9) again, but this time obtaining the best solutions for three free parameters, m, $\delta B/B_0$, and δ (the same method as explained in Sect. 3.4.1). The B-field strength is calculated for each region based on these updated parameters. Table 3.3 shows the best-fit parameters and B-field strengths. We obtain the same turbulence correlation value ($\delta = 10$ mpc) and B-field strength ($B = 151$ μG) for the R1 region, while for the R2 region is lower than before (with two free parameters; see Table 3.2), and for R3 region the fit routine does not converge, due to the limited number of independent data points available.

Table 3.3: Best-fit parameters with three free parameters, using Eq. 3.9.

Region	$\delta B/B_0$	m (rad/pc)	δ (mpc)	$B_{\rm pos}$ (μG)
R1	0.4 ± 0.1	1.6 ± 0.2	10 ± 4	151 ± 9
R2	0.46 ± 0.05	3.6 ± 0.1	3.0 ± 0.01	127 ± 4

Next, we discuss the impact of assumption on the methods we used to calculate the B strength. In this work, we used the combination of DCF and HH09 methods to calculate the B-field strength of the filament. Various modifications to the DCF method have been proposed (e.g., Ostriker et al. 2001; Houde et al. 2009; Cho & Yoo 2016; Lazarian et al. 2020; Skalidis & Tassis 2021). There are several assumptions made by DCF, including the fact that turbulence is Alfvénic, as well as that $\sigma_{\rm nt}$ traces turbulent motions and that the mean B-field is uniform. In general, it has been suggested that the original DCF method overestimates B-field strength (Pattle et al. 2022b; Ostriker et al. 2001; Houde et al. 2009; see Pattle & Fissel 2019 and Skalidis & Tassis 2021 for a thorough comparison). To show the differences, we used one of the modification methods suggested by Skalidis & Tassis (2021). Their modified equation includes non-Alfvénic (compressible) modes and Alfvénic (incompressible) modes and leads to

$$B^{*}_{\rm pos} = \sqrt{2\,\pi\,\rho}\,\frac{\delta v}{\sqrt{\delta\theta}}. \tag{3.11}$$

Those authors claim that this method is more accurate in retrieving $B_{\rm pos}$, and has lower error than DCF and HH09 methods. Table 3.2 shows calculated values for each region. As expected, the $B_{\rm pos}$ for all regions has values lower than those obtained with the DCF and HH09 methods.

3.4.3 Cloud stability

Determining the importance of B-fields for cloud gas dynamics and cloud balance is one of the main motivations for studying the B-field in the cloud. However, determining how the B-field affects a cloud's dynamic behavior remains challenging. One parameter that helps us quantify this importance is the mass-to-flux ratio normalized to the critical value, λ. Observed mass-to-flux ratios exceeding the critical value of 1 indicate that the cloud is supercritical, and the B-field cannot prevent it from collapsing. On the other hand, clouds are subcritical if their ratio is $\lambda < 1$ and the B-field stabilizes gravity. We calculated λ from (Crutcher, 2012a)

$$\lambda = \frac{(M/\Phi)_{\rm observed}}{(M/\Phi)_{\rm crit}} = 7.6 \times 10^{-21}\,\frac{N(\mathrm{H_2})}{B}\left(\frac{\mu G}{\mathrm{cm^{-2}}}\right), \tag{3.12}$$

where $N(\mathrm{H_2})$ is the column density of the filament in units of $\mathrm{cm^{-2}}$, and B is the total B-field strength given in μG. We used $B = B_{\rm pos}$ derived from Eq.3.10. We note that this introduced a source of uncertainty, as the inclination of the total B field with respect to the PoS. We used the $N(\mathrm{H_2})$ values present in Table 3.2, obtained from the *Herschel* column density map, which represents the average $N(\mathrm{H_2})$ for each region. In the last column of Table 3.2, we report our derived values of λ for each region. The results for all three regions in the filament indicate that their inferred mass-to-magnetic flux ratios are subcritical (see Table 3.2).It is worth emphasizing that, despite employing $B^{*}_{\rm pos}$ <$B_{\rm pos}$), the parameter λ consistently remains below 1. This means that B-fields are dynamically relevant and are expected to support the filament against its own gravity, especially for the region R3. The B-field in R3 is probably distorted by the gravity of the nearby central hub. However, one should keep in mind that these considerations do not take into account corrections for the geometry of the filament and the B-field. Strictly speaking, the mass M in Eq. 3.12 should be that contained in a flux tube characterized by a B-flux Φ. The derived values of the mass-to-flux ratio should therefore be taken as indicative.

3.5 Modeling of the filament

We used the model developed by TCa and TCb in order to interpret the properties of the filament of B59. TCb considers the stability of a self-gravitating, polytropic cylinder threaded by a helical B-field as a function of the relative strength of the axial and azimuthal components of the field (see also Fiege & Pudritz 2000). Although our polarization maps suggest the presence of a twist in the B-field (see Fig. 3.2 or Fig. 3.4), our data are insufficient for a detailed comparison with the models of TCb, and we defer this analysis to subsequent work. Here, we present a preliminary analysis following TCa, where the extra support provided by B-fields (and possibly turbulence) against gravity is modeled by assuming a polytropic relation between the gas pressure, p, and the gas density, ρ,

$$p = K\,\rho^{\gamma_{\mathrm{p}}}, \tag{3.13}$$

where γ_{p} is the polytropic exponent and K is a constant.

In this case, we assumed that the filament is perpendicular to the line of sight and is cylindrically symmetric. In a polytropic cylinder, the temperature $T_{\mathrm{p}} \propto (dp/d\rho)^{1/2}$ (hereafter the polytropic temperature) is a measure of the radial support against gravity. The comparison of the measured gas temperature T_{g} with T_{p} therefore reveals whether or not the thermal pressure gradient is sufficient to provide support to the cloud. In all calculations, we used polytropic index n, defined as $\gamma_{\mathrm{p}} = 1 + 1/n$. We implemented the TCa models to describe the filament in B59. TCa speculated about the support given by a superposition of low-amplitude Alfvén waves, which behave as a polytropic gas with $n = -2$, resulting in density profiles in agreement with observations. Fully developed MHD turbulence is another possibility, although these filaments are not very turbulent, as shown in Sect. 3.3. Considering the curved shape of the filament, we divided the filament into three regions (R1, R2, and R3; see Fig. 3.4), as explained in Sect. 3.4. In the R1 region, most of the polarization orientations are generally perpendicular to the cylinder spine, while in the R2 region, the orientation tends to align with the cylinder spine. Lastly, the R3 region has a more complex polarization pattern resembling a U-shape. In each segment, the observed column density $N(\mathrm{H_2})$ was evaluated as a function of cylindrical radius, averaging the two sides from the center to the edges (0 to x_{max} and 0 to x_{min}; see Fig. 3.8). Figure 3.9 shows the results for the R1 and R2 regions of the filament.

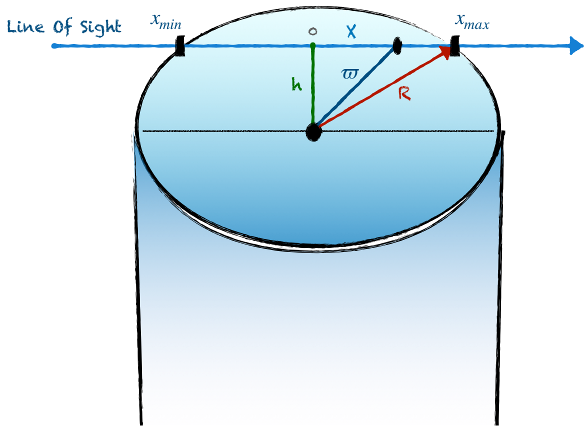

Figure 3.8: Simplified model of a cylindrical filament illustrating all parameters used for modeling. The cylinder is assumed to have an infinite length and radius R (see Eq. 3.14 and Eq. 3.15). The blue arrow indicates the direction of the observer's line of sight.

The column density profile obtained in this way from *Herschel* data was compared to the column density profiles of unmagnetized polytropic filaments computed by TCa for various cylindrical polytropes index (see Fig. 3.9). To compare the observation data with the model from TCa, we converted the density of the model to column density $N(h)$. As a means of making the calculation more straightforward, we used the standard nondimensional density, θ, and radius, ξ, parameters defined as

$$\varpi = \varpi_0 \xi, \quad \rho = \rho_0 \theta^n, \tag{3.14}$$

where $\varpi_0 = \sqrt{c_s^2/(4\pi G \rho_0)}$ and ρ_0 is the density at the center of the filament (for more details about the model, see TCa). We assumed volume number density on the axis $n_c = 2 \times 10^4$ cm^{-3} to calculate $\rho_0 = \mu\, m_{\rm H}\, n_c$. In the models, the column density,$N(h)$, was computed from the tabulated density profile $n(\varpi)$, as

$$N(h) = \int_h^R \frac{n(\varpi)\varpi}{\sqrt{\varpi^2 - h^2}}\, d\varpi = \frac{2\,\rho_0\,\omega_0}{\mu\, m_{\rm H}} \int_{h/\varpi_0}^{R/\varpi_0} \frac{\theta^{\rm n}\, \xi}{\sqrt{\xi^2 - h^2/\varpi_0^2}}\, d\xi, \tag{3.15}$$

where R is the radius of the filament's "surface," where the filament merges into the ambient medium (also called the "truncation radius"; see Fig. 3.8 for more details). A radial column density profile of observed and polytropic cylinder models for various n is shown in Fig. 3.9. Column densities are normalized to on-the-axis values, $N(0)$, to eliminate biases due to arbitrary choice of n_c. The averaged column density profiles of the R1 and R2 regions are well reproduced by cylindrical polytropes with $-4 \lesssim n \lesssim -2$. In general, a single value of $n = -3$ is able to provide a good fit to the data in regions R1 and R2. We used $n = -3$ as the best-fit value in the rest of the analysis. The fitted parameters for these regions are listed in Table 3.4. In R3, the fit is not good because it is difficult to consider this part of the filament as cylindrically symmetric. Furthermore, the R3 region lies close to the central hub, and is possibly characterized by strong gas flows, which makes it more challenging to fit with our simplified model.

According to the set of parameters for R1 and R2 regions (see Table 3.4), the stability parameter $\xi_{\rm s} = R/\varpi_0 = 4.16$ and 3.9 is smaller than the critical value $\xi_{\rm cr} = 4.28$ for R1 and R2 regions, respectively (see Table 1 of TCa). Given that ξ_s and ξ_{cr} are very close, and considering the various assumptions made in the model, we conclude that ξ_s is not significantly larger than ξ_{cr}, and there is no sign of instability in the filament. Therefore, the filament is stable to radial collapse.

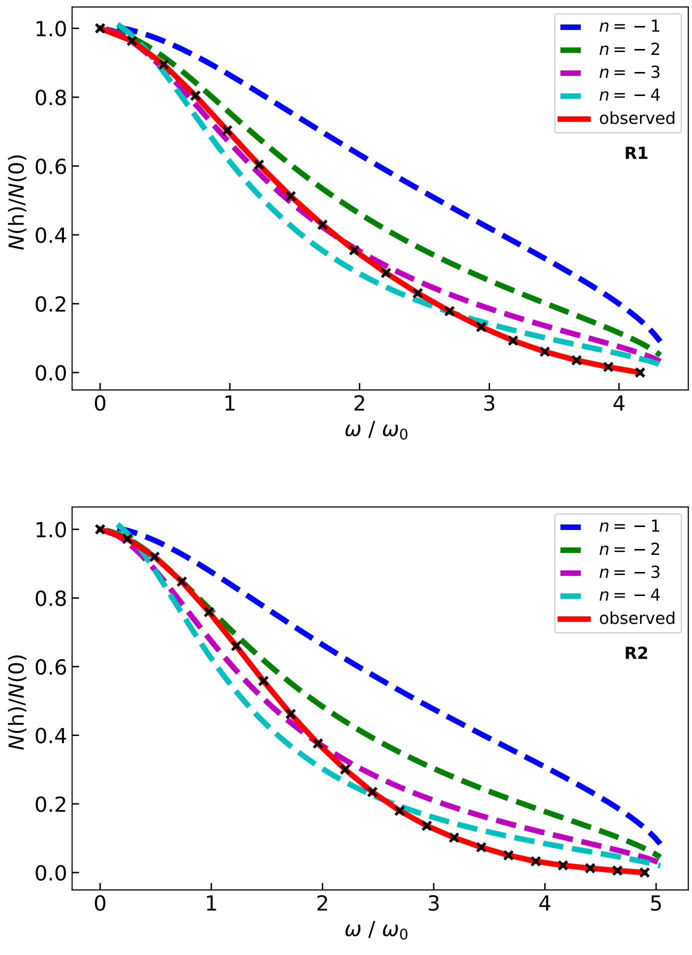

Figure 3.9: Radial column density profiles (with background subtraction and normalized to the central column density, $N(0)$) of both observations (solid red curves) and polytropic cylinder models with $n = -1, -2, -3, -4$ (dashed curves). The radius is normalized to ϖ_0. The black crosses indicate the observation data points. The top and bottom panels describe regions R1 and R2 of the filament, respectively.

Table 3.4: Model parameters.

Regions	n	γ_p	ϖ_0 (cm)	$\varpi = R$ (cm)	$\xi_{cr}^{(a)}$	$\xi_s = R/\varpi_0$
R1	-3	2/3	7.25×10^{16}	3.02×10^{17}	4.28	4.16
R2	-3	2/3	7.25×10^{16}	2.84×10^{17}	4.28	3.92

Note: [a] from Toci & Galli (2015a).

Cylindrical polytropes have a different mass per unit length depending on the polytropic index. We calculated the mass per unit length for various polytropic indexes using the following integral:

$$\frac{M}{L} = 2\pi\rho_0\varpi_0^2 \int_0^{R/\varpi_0} \theta^n \xi d\xi. \tag{3.16}$$

The estimated $\frac{M}{L}$ for each model are listed in Table 3.1. In Sect. 3.3.2 we show that the $\left(\frac{M}{L}\right)_{\rm fil}$ from the observation data is smaller than the critical value, which indicates the filament is in a stable state. We show in Table 3.1 that $\frac{M}{L}$ (from Eq. 3.16) for $n = -3$ is smaller than the critical value in agreement with observations.

We used the data of Fig. 2 from the TCa model to plot radial profiles of the polytropic temperature $T_{\rm p}$ of a polytropic cylinder. In Fig. 3.10 the dashed lines show the temperature as a function of radius from the models. In contrast, the solid red curves show dust temperature as a function of radius for the filament, obtained from *Herschel* data for R1 and R2. The dust temperature $T_{\rm d}$ increases outward from ~ 13.9 K on the axis to ~ 15.5 K at $\varpi \sim 0.09$ pc in the region R1 of the filament (see Table 3.5; the dust temperature map is shown in Appendix B.2). As for the gas temperature $T_{\rm g}$, similar (or even steeper) gradients are expected. Gas and dust are expected to be coupled at high densities above $\sim 10^5$ cm^{-3} (Goldsmith 2001), whilst gas temperatures in the outer more diffuse regions are expected to be higher than the dust temperature (Keto & Caselli 2008; Galli et al. 2002). Figure 3.10 presents radial profiles of the observed dust and polytropic temperature $T_{\rm p}$ for the same polytropic indexes shown in Fig. 3.9. The polytropic temperature (a measure of the polytropic pressure, which includes all contributions to the support of the filament, not just thermal pressure) at the surface of the filament is a factor of ~ 2 larger than on the center of cylinder for regions R1 and R2 (see Table 3.5). The measured dust temperature for the same regions of the filament, from the center to the surface, increases by 12% and 14%, respectively (from *Herschel* dust map). The gas temperature is not known; however, it is unlikely to increase by a factor as large as 1.90 or 1.84. Assuming $T_{\rm g}(0) = T_{\rm d}(0) = 14$ K, for thermal pressure alone to support the R1 part of the filament, the gas temperature at the surface of the filament must be $T_{\rm g}(R) = 25.3$ K, which is unrealistic (and the same reason for the R2, $T_{\rm g}(R) = 24.3$ K, Table 3.5). Even if the profile for the *Herschel* temperatures is flatter than the real profile, due to the averaging of different temperatures along the line of sight (which tends to overestimate the temperatures in the densest and coldest regions), a sharper increase toward the outskirts should be observable. Therefore, the filament must be supported radially by some other agent(s) than thermal pressure, like B-fields or (albeit less likely, as previously discussed) turbulent support.

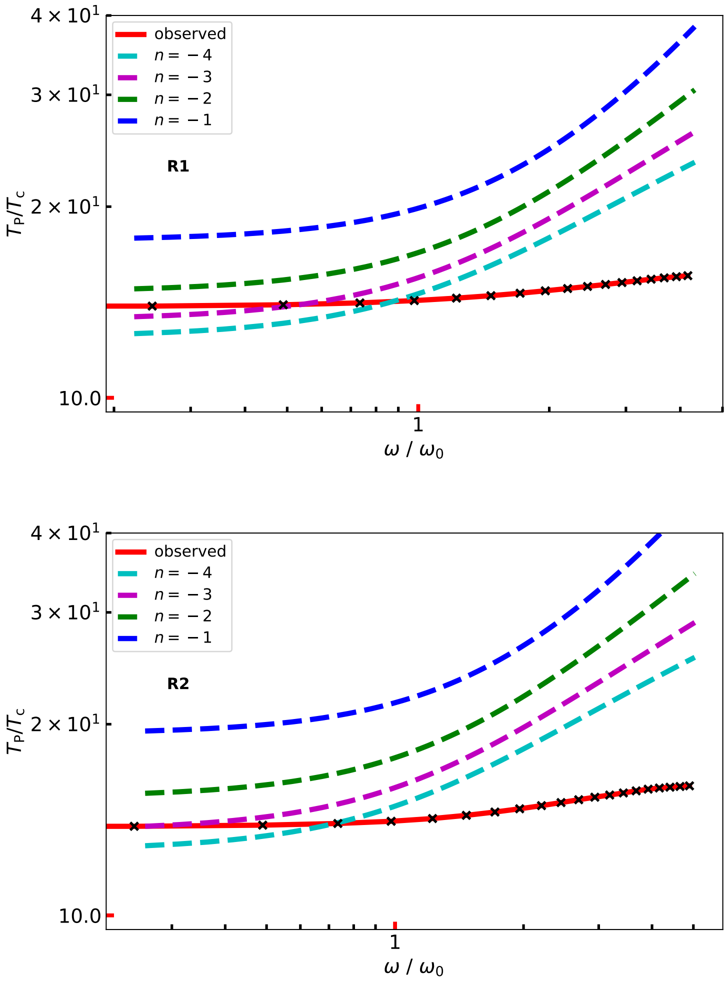

Figure 3.10: Radial profiles of the observed temperature and the polytropic temperature, T_P (normalized to the central temperature value, T_c, for the same polytropic indexes, n, as in Fig. 3.9). Solid and dashed lines represent observations and models, respectively. The black crosses indicate the observation data points. The top and bottom panels represent regions R1 and R2 of the filament, respectively.

Table 3.5: Temperatures at the center and surface of a cylinder from models and observations (T_d).

	$R1_{obs}$	$R1_{mod}$	$R2_{obs}$	$R2_{mod}$
$T_c^{(a)}$ (K)	13.9	13.3	13.8	13.2
$T_R^{(b)}$ (K)	15.5	25.3	15.7	24.3
R (pc)	3.9	3.9	4.2	4.2

Note: $^{(a)}$ Temperature at the center of the cylinder, $^{(b)}$ Temperature at the surface of the cylinder.

3.6 Conclusions

We used $C^{18}O$ and ^{13}CO (3-2) transition data from JCMT to reveal the kinematics toward one filament in B59, and NIR polarization observations to investigate the polarization properties of this isolated filament. We modeled the filament as a self-gravitating hydrostatic cylinder, as in TCa. Our results are as follows:

- According to the nonthermal motion strength derived from the $C^{18}O$ line, the filamentary cloud appears to be in a quiescent state where the nonthermal gas motions are smaller than or on the order of the sound speed of the gas ($\mathcal{M} = 0.54 < 1$). On the contrary, for the ^{13}CO emission, which traces the larger-scale gas, we obtain $\mathcal{M} = 1.0$, indicating transonic motions.

- Based on the V_{lsr} map of $C^{18}O$, we determine a gas flow toward the location of the hub with a velocity gradient of about $\sim 0.69 \pm 0.01$ km s^{-1} pc^{-1}.

- The orientation of the polarization angles changes from perpendicular to the filament spine in the eastern region to parallel to it going toward the west. This could be caused by local velocity flows of matter infalling toward the hub, with the B-field being dragged by gravity along the filaments.

- The distribution of the polarization angles shows two peaks. One Gaussian profile corresponds to polarization angles in the R3 region, while the other Gaussian distribution suggests a broader distribution due to the merger of the R1 and R2 regions.

- Using the DCF and HH09 methods, we calculated the strength of the B-field on the plane of the sky for three different regions of the filament; they range from 150 to 230 μG (see Table 3.2).

- Our analysis shows that the mass-to-flux ratio is lower than the critical value (i.e., the filament is subcritical), which means that the B-field is nominally sufficient to stabilize gravitational collapse due to its own gravity.

- The observed radial density profiles of filaments are, in general, well represented by polytropic indexes in the range $-3 < n < -3/2$ (see Fig. 1 in TCa). This rules out isothermal gas pressure as a supporting agent for $n = \pm\infty$. In principle, an outward increasing gas temperature can provide the required pressure gradient, but the observed dust temperature gradient is too shallow (see Fig. 3.10). It is unlikely that the gas temperature gradient is much steeper at these densities. The observed radial profiles of the density and temperature profiles of the filamentary cloud, compared to theoretical models of polytropic self-gravitating cylinders, show that the filament is stable to radial collapse and is supported radially by agents other than thermal pressure.

Our findings suggest that the filament remains stable against radial collapse and is supported radially by factors beyond thermal pressure. The B-field is nominally sufficient to stabilize gravitational collapse due to its own gravity. The B-field we derived is adequately strong to counteract gravitational pull from the filament. Our result of a magnetically subcritical condition implies that the filament is stable and not prone to fragmentation.

Acknowledgements E. Redaelli acknowledges the support from the Minerva Fast Track Program of the Max Planck Society. G. Franco acknowledges the partial support from the Brazilian agencies CNPq and FAPEMIG. A. Duarte-Cabral acknowledges the support from a Royal Society University Research Fellowship (URF/R1/191609). This research has used data from the *Herschel* Gould Belt survey (HGBS) project (http://gouldbelt-herschel.cea.fr). The HGBS is a *Herschel* Key Programme jointly carried out by SPIRE Specialist Astronomy Group 3 (SAG 3), scientists of several institutes in the PACS Consortium (CEA Saclay, INAF-IFSI Rome, and INAF-Arcetri, KU Leuven, MPIA Heidelberg), and scientists of the *Herschel* Science Center (HSC), André et al. (2010b). The authors thank Juan Diego Soler for his support and discussion about magnetic field morphology and Claudia Toci for several interesting discussions of the modeling work used in this study.

Chapter 4

The Snake Filament: A study of polarization and kinematic properties

The contents of this chapter are submitted for publication in Astronomy & Astrophysics. Credit: Tabatabaei et al., 2025

4.1 Introduction

The formation and evolution of dense filamentary structures in the interstellar medium (ISM) are critical for understanding star formation (André et al. 2014). A central focus in star formation is understanding the processes that govern the creation of filaments and regulate the star formation within them. Magnetic fields are widely recognized as playing a key role in the formation of these filaments, the cores within those filaments, and the eventual stars within them (Pattle et al., 2023; Arzoumanian et al., 2019). However, the relative contributions of magnetic fields, turbulence, and gravity to filamentary structure formation remain poorly understood (Li et al. 2014a, Crutcher 2012b). Gravity and turbulence are two key factors that can influence both the structure and strength of the magnetic field (Hennebelle & Inutsuka 2019), suggesting that these fields exert considerable influence on the gas within filaments, helping channel material into filaments and facilitating star formation. Therefore, observing the magnetic field in quiescent filaments before star formation is essential for understanding its dynamic role in shaping these widespread structures.

Dust polarization observations, notably from the Planck satellite, have revealed ordered magnetic field structures in molecular clouds, particularly in the Gould Belt clouds of the Solar neighborhood (Planck Collaboration et al. 2016c). These observations show that in regions of low column density, the gas structure tends to align parallel to the magnetic field. In contrast, the gas is often oriented perpendicular to the magnetic field in higher-density regions. This alignment transition, observed at visual extinctions of $A_{\rm V} \sim 2.7 - 3.5$ mag, underscores the role of magnetic fields in shaping filamentary structures in star-forming regions (Planck Collaboration et al. 2016c, Soler et al. 2017b). Similar behaviors are observed in filaments at lower column densities using optical and near-infrared (NIR) polarization data (Sugitani et al. 2011, Palmeirim et al. 2013b, Franco & Alves 2015b), indicating that magnetic fields play a significant role in the alignment of dust grains within these regions (Soler 2019, Santos et al. 2016). Recent HAWC+ observations of the Serpens South cloud reveal a second transition in the alignment of gas structures with magnetic fields at $A_V \sim$ 21 mag, where the alignment shifts back to being parallel (Pillai et al. 2020a). This transition indicates the onset of magnetic supercriticality, allowing gravitational collapse and star cluster formation even in the presence of strong magnetic fields.

All molecular clouds contain filamentary structures, as demonstrated in the *Herschel* Gould Belt Survey (André et al. 2010c). Furthermore, the majority of gravitationally unstable cores, known as prestellar cores (Ward-Thompson et al. 2007), which are on the brink of star formation, are located within these filaments (André et al. 2010c, Könyves et al. 2015). This suggests that dense cores form within the filamentary structures of molecular clouds.

In this study, we focus on the Snake filament (also known as Barnard 72), employing both polarization data and molecular line observations to investigate the role of magnetic fields in shaping its filamentary structure. Molecular line observations were performed using the IRAM telescope, where we observed the J = 1 −> 0 transitions of $C^{18}O$ and ^{13}CO. Additionally, we obtained polarimetric observations from the 1.6 m and 60 cm telescopes at the Observatório do Pico dos Dias, spanning optical and near-infrared wavelengths. Through the analysis of polarization properties and gas behavior within the Snake filament, we aim to understand how magnetic fields influence its structure and dynamics, thereby advancing our knowledge of star formation in filamentary regions.

This paper is structured as follows: in Sect. 4.2, we detail the observational data obtained from multiple telescopes, including submillimeter polarimetry from Planck, molecular line observations using the IRAM 30m telescope, and optical and NIR polarimetric data from the OPD/LNA telescopes. The methods for data reduction and calibration are also described. In Sect. 4.3, we present the result of data processing. Sect. 4.4 investigates the filament's polarimetric and kinematic properties, examining the relationship between the magnetic field geometry and the filament's structure, finally, in Sect. 4.5, we summarize the key findings of this work.

4.2 Data

4.2.1 Molecular line data

The Snake filament was observed using the 30m telescope at Pico Veleta (Spain) from IRAM, under project 038-11, in August of 2011. The ground-state transition of $C^{18}O$ (1-0) and ^{13}CO (1-0) at a rest-frame frequency of 110.201354 MHz and 109.782173 MHz was observed, respectively. The observations were made using EMIR E090 receiver, the VErsatile SPectrometer Assembly (VESPA), with a resolution of 20 kHz. The data were

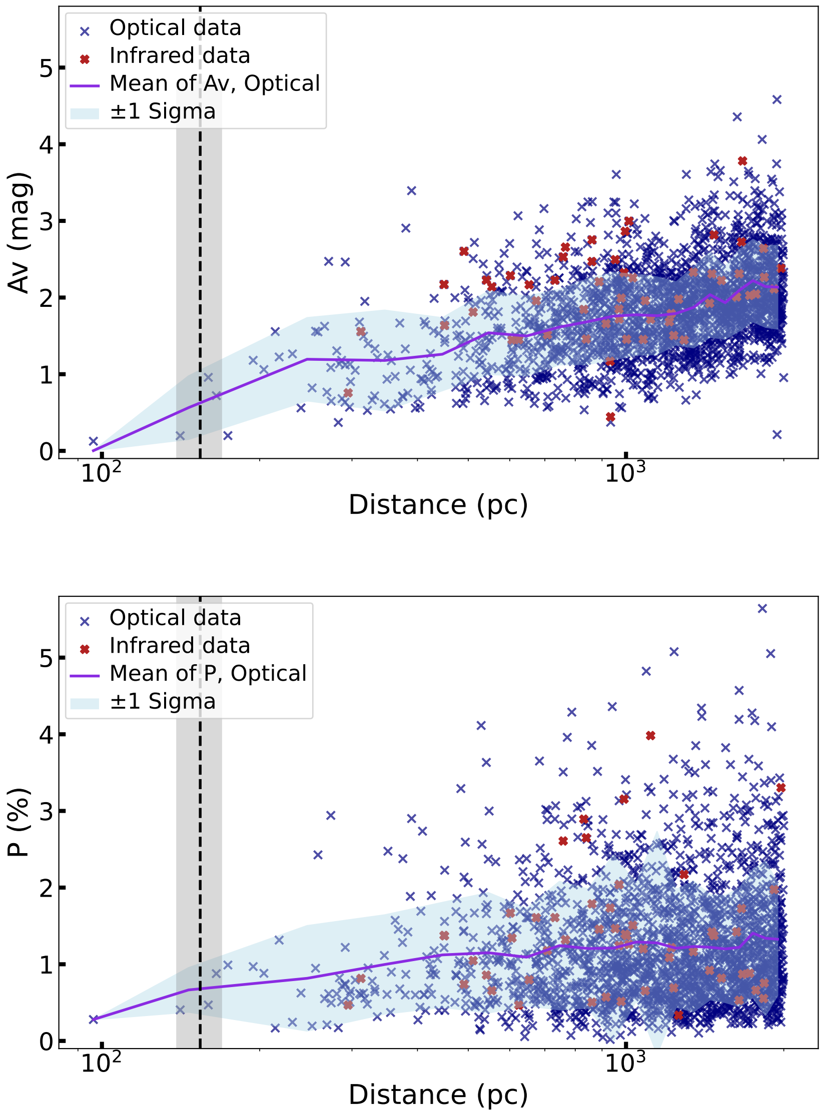

Figure 4.1: Top panel: Visual extinction (A_V) as a function of the distance of stars within 2 kpc from the Sun. The extinction and distance values are derived from the `StarHorse` catalog. Lower panel: Polarization percentage as a function of the distance. A vertical dashed line at 154 ± 15 pc marks the distance of the Snake filament. The purple line represents the mean value in bins of 100 pc, with the light blue shaded area indicating the $\pm 1\sigma$ uncertainty.

calibrated and reduced using CLASS software, GILDAS [1] software. The mean rms noise level in T_mb scale is 0.3 K with 0.05 $\mathrm{km\,s^{-1}}$ channels.

[1] https://www.iram.fr/IRAMFR/GILDAS/

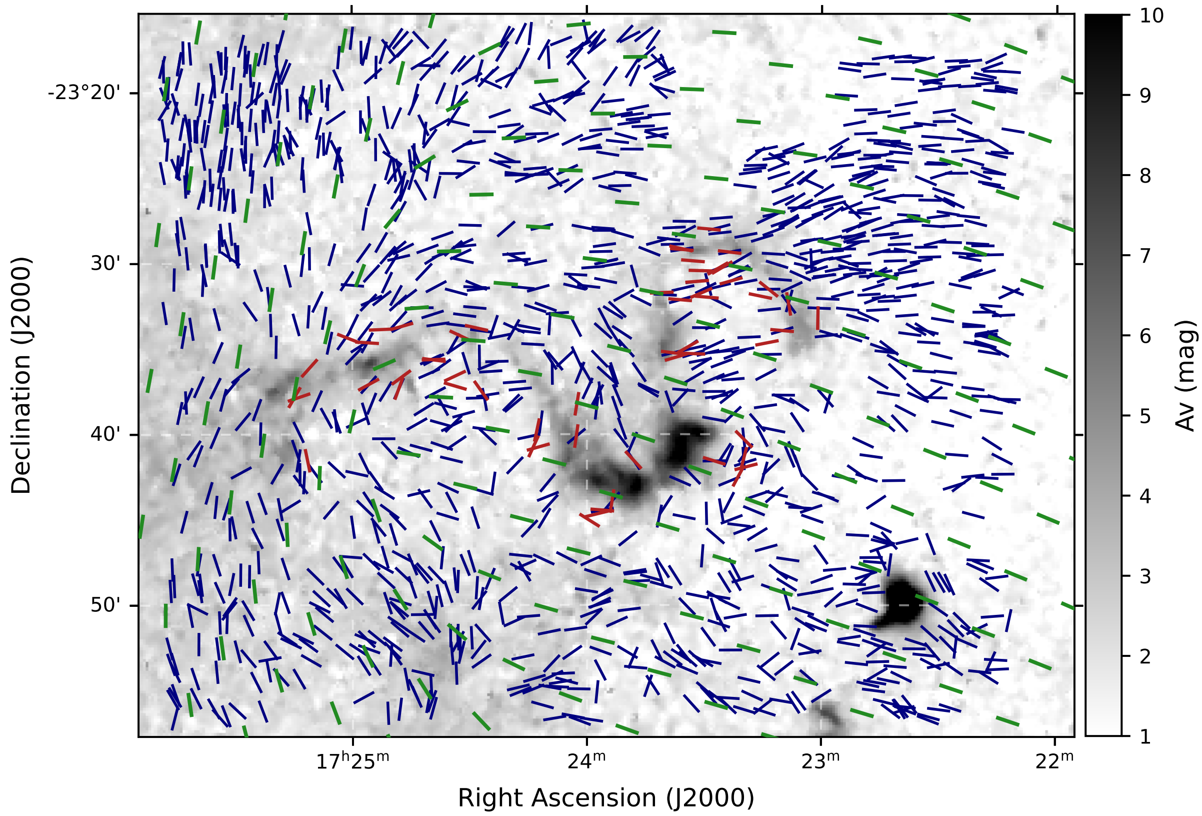

Figure 4.2: Dust extinction map of the Snake region in color scale. All segments represent the B-field orientation. Blue and red segments are inferred from the optical and NIR data, respectively, with S/N > 3. The green segments show the magnetic field orientation from *Planck* data at the resolution of $20'$. The vectors are scaled to the same size to enhance visualization clarity.

4.2.2 Starlight polarization data

The polarimetric observations were carried out using the 1.6 m and the IAG 60 cm telescopes at the Observatório do Pico dos Dias/Laboratório Nacional de Astrofísica (OPD/LNA, Brazil) during several missions, 2007 and 2024, for the optical data, conducted in the R band (6474 Å) and, 2018 and 2019, for the near-infrared data (NIR), conducted in the H band. The data were obtained using IAGPOL, an imaging polarimeter specifically adapted for polarimetric measurements. For further details on the setup of the polarimeter, refer to Magalhaes et al. (1996). The optical polarimetry was obtained for 20 fields, with a field of view of about $10' \times 10'$ each, covering the whole Snake filament region. The NIR data were obtained for 11 fields of view about $4' \times 4'$ each.

In this study, we assumed that the angle of optical and NIR starlight polarization, denoted as ϕ_{star}, is identical to the orientation of the magnetic field, ψ_{star}.

4.2.3 Polarized dust emission from Planck

We used the 353 μm Planck[2] polarization data at a resolution of 4.8 $'$. From the Stokes Q and U, we study the polarization angles of dust emission in the sky region containing the Snake filament. To improve the signal-to-noise ratio (S/N) of the extended emission, we applied a Gaussian convolution to the Planck beam, achieving 20$'$ resolution maps. We derived the polarization angle of dust emission, $\phi = 0.5\tan^{-1}(U/Q)$. The polarized intensity is computed as:

$$P = \sqrt{Q^2 + U^2}. \tag{4.1}$$

The Stokes parameters obtained from the Planck database are measured eastward from the north Galactic pole. These measurements were then converted to the equatorial coordinate system, with angles measured eastward from the north celestial pole. We applied the method suggested by Stephens et al. (2011) (See their appendix for more details). Using the equation A2 from their paper:

$$\text{offset angle} = \arcsin\left[\frac{\sin(123^\circ - l_1)\sin 62.6^\circ}{\sin(90^\circ - \delta)}\right] \tag{4.2}$$

and considering the Snake filament has galactic longitude coordinate $l \sim 1.9^\circ$ and a declination $\delta \sim -23.5^\circ$, we calculate the offset of 56°. since the area covered by the Snake filament is relatively small compared to the full field of view of the sky, we applied the same offset all over the field, and 56° was subtracted from ϕ.

The submillimeter polarization is assumed to be perpendicular to the magnetic field orientation, ψ. We rotate the angles by 90° to obtain the corresponding plane-of-sky magnetic field orientations, ψ_{submm}. Therefore throughout this work, the polarization data from optical, near-infrared, and submillimeter wavelengths consistently show that the polarization vectors align with the magnetic field direction in their respective regions.

4.3 Result

4.3.1 Data handling and cross-match with `StarHorse` catalog

For our analysis throughout this paper, we utilize data that correspond to entries in the `StarHorse` catalog (Anders et al. 2022). The `StarHorse` catalog provides stellar parameters, e.g., distances and extinctions, for 362 million stars, by combining Gaia EDR3 data (Gaia Collaboration et al., 2016, 2021) with photometric surveys such as Pan-STARRS1 (Chambers et al. 2016), SkyMapper (Onken et al. 2019), 2MASS (Cutri et al. 2003), and AllWISE (Cutri et al. 2013). Its improved precision and broad wavelength coverage enable distance accuracies of approximately 3% for stars with a magnitude of 14 and 15% for magnitudes of 17 (Anders et al. 2022). We decided that stars located at distances greater than 2 kpc may be affected by distant clouds, requiring their exclusion from our sample.

[2]http://pla.esac.esa.int/pla/

Consequently, all analyses and visualizations presented herein focus solely on stars within a distance of 2 kpc to ensure that our results are not influenced by the presence of distant background materials. In the NIR dataset, we identified 1244 stars, with 491 of these entries corresponding to the `StarHorse` catalog. Notably, 57 stars are situated within a distance of less than 2 kpc from the Sun. Conversely, the optical dataset includes 19627 stars, of which 13252 match entries in the `StarHorse` catalog. Among these, 2037 stars are located within 2 kpc of the Sun.

Figure 4.1 (upper panel) illustrates the trend of increasing visual extinction as a function of distance, characterized by a gradual slope for stars with distances up to 2 kpc. The blue crosses represent data points from the optical dataset, while the red crosses correspond to the NIR dataset. A vertical dashed black line at d = 154 pc (see Sect. 4.4.1) marks the distance of the Snake filament with the shaded gray area surrounding it (spanning from 139 pc to 169 pc) representing the region of uncertainty, defined as ±15 pc. The plot also includes the mean visual extinction ($A_{\rm V}$) calculated in bins of 100 pc, shown with a purple curve. This line offers a smoothed representation of the overall trend of increasing extinction with distance, helping to highlight the general pattern across the dataset. The light blue area surrounding the purple line shows the $\pm 1\sigma$ variation from the mean, providing an uncertainty in the extinction measurements over distance. The optical and NIR datasets show similar trends, while fewer data points are in the NIR data set. The bottom panel of Fig. 4.1 presents the polarization percentage as a function of distance using the same dataset. The mean polarization percentage, calculated in 100 pc bins, reveals an initial increase in polarization, followed by a relatively steady trend extending up to 2 kpc. This steady trend indicates the absence of any dense clouds located beyond the Snake filament, up to the 2 kpc threshold. For Fig. 4.1, we used S/N > 1 for the optical data to include low-polarization stars, which are likely located in the foreground of the Snake filament. For the NIR data, we applied S/N > 3, as the observing process for NIR is inherently noisier, resulting in lower S/N values. For the remaining analysis, we used a more stringent criterion of S/N > 3 for the optical and NIR data to ensure data reliability while retaining sufficient sources.

Figure 4.2 shows the dust extinction map of the Snake filament region at a spatial resolution of 20″ (Román-Zúñiga et al. 2010). Polarization vectors in optical (blue), near-infrared (NIR) (red), and submm (green) are plotted over the extinction map. The submm vectors are rotated by 90° to show the B-field orientation. The NIR data probe the denser part of the Snake filament, whereas the optical data trace the lower visual extinction of the observed field.

4.3.2 Line opacity

We estimate the opacity of ^{13}CO (1-0) and C^{18}O (1-0) using the following expression:

$$\tau = -\ln\left[1 - \frac{T_{\rm MB}}{J_\nu(T_{\rm ex}) - J_\nu(T_{\rm bg})}\right], \tag{4.3}$$

where $T_{\rm ex} = 15$ K is the excitation temperature derived from the *Herschel* dust temperature map, $T_{\rm MB}$ is the peak main beam temperature of the line, J_ν represents the equivalent Rayleigh-Jeans temperature, and $T_{\rm bg} = 2.73$ K is the temperature of the cosmic microwave background. To estimate uncertainties, we varied $T_{\rm ex}$ within a physically meaningful range, ensuring that the lower limit does not exceed the minimum excitation temperature,$T_{\rm ex} = 15$ K. The optical depth of $C^{18}O$ (1-0) is determined to be $\tau = 0.6^{+0.1}_{-0.1}$, calculated using $T_{\rm MB} = 5.5$ K. The uncertainties were estimated by considering a ±1 K variation in $T_{\rm ex}$. Similarly, for the ^{13}CO (1-0) line, we obtain $\tau = 2.1^{+0.4}_{-0.9}$ using $T_{\rm MB} = 11$ K. These results confirm that the $C^{18}O$ (1-0) gas is optically thin, whereas the ^{13}CO (1-0) gas is optically thick. The $C^{18}O$ (1-0) line has a relatively low critical density ($n_c \sim 10^3$ cm^{-3}), making it reasonable to consider that the excitation temperature ($T_{\rm ex}$) is approximately equal to the kinetic temperature ($T_{\rm k}$), considering dust-gas coupling. Although the *Herschel* dust temperature is typically higher than the excitation temperature, as mentioned earlier, we also calculated the line opacity for a variation in $T_{\rm ex}$ as an uncertainties.

4.4 Analysis and Discussion

4.4.1 Distance and source detection

We used the 3D dust extinction map provided by Edenhofer et al. (2024) to obtain the dust distribution within the Snake filament region. This map, which extends up to 1.25 kpc from the Sun with a $14'$ angular resolution, is based on data from 54 million stars as analyzed by Zhang et al. (2023). They derived the stars' atmospheric parameters, distances, and extinctions by forward-modeling the low-resolution Gaia BP/RP spectra (Carrasco et al., 2021). We employ the publicly accessible version of the map[1]. Figure 4.3 shows the dust extinction distribution as a function of the distance. We scaled the map values by 2.8 to convert them to $A_{\rm V}$ in magnitudes based on the recommendation of Edenhofer et al. (2024). The coordinates of the Snake filament's center, $l = 1.8°$ and $b = 6.9°$, were used to extract the relevant data from the 3D map. We observe a well-defined dust sheet with a distance of 154 pc, representing the Snake filament's distance. This distance agrees with the estimated distance of the entire Pipe Nebula (145 ± 16 pc, Alves & Franco 2007; 163 ± 5 pc, Dzib et al. 2018a).

This study utilizes version 7.1 of the SPHEREx Target List of ICE Sources (SPLICES), which is part of the SPHEREx all-sky survey mission (Ashby et al., 2023). The catalog contains 8.6×10^6 objects that are brighter than approximately 12 Vega magnitudes in the W2 band. To identify young stellar objects (YSOs), we use the W1[3.6 mag] - W2[4.5 mag] versus W2[4.5 mag] - W3[5.8 mag] color-color diagram of AGB candidates from SPLICES (see Ashby et al., 2023). The regions defined by Koenig & Leisawitz (2014) for the selection of Class I and Class II young stellar objects. No YSOs have been detected in the area using the Spitzer GLIMPSE color-color diagram. We utilize the mid-infrared colors [3.6 - 4.5] versus [4.5 - 5.8] to identify YSOs in the region. We consider a region of size 2 pc that

[1]https://zenodo.org/records/8187943

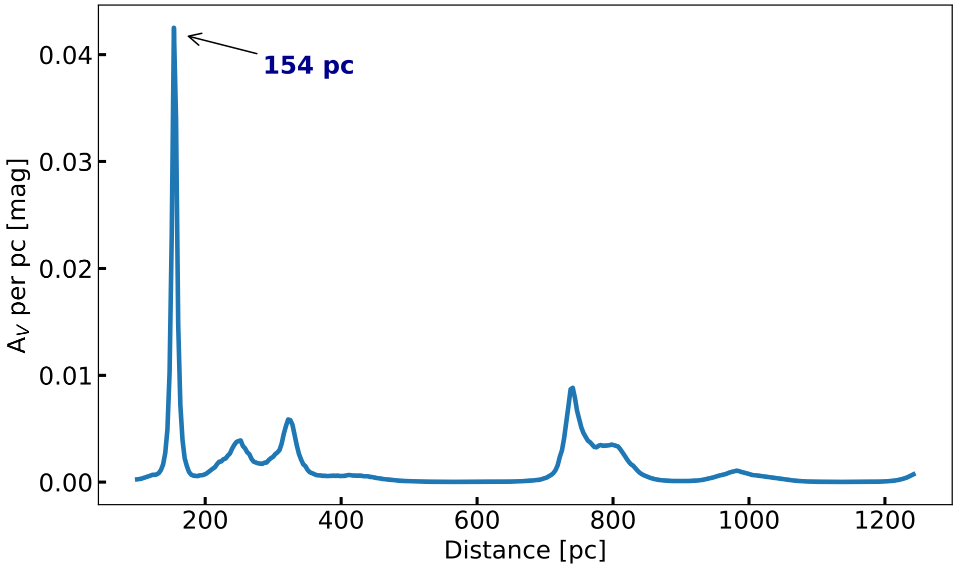

Figure 4.3: 2D dust extinction map illustrating the dust distribution as a function of distance up to 1.25 kpc from the Sun (Edenhofer et al. 2024). The peak at 154 pc indicates a distance corresponding to the Snake region.

encompasses the filamentary features associated with the Snake region, shown in Fig. 4.2, and find 822 objects that are detected in the region (black dots in Fig. 4.4). We apply a distance constraint, selecting objects that are 1 kpc away (represented by purple diamonds in Fig. 4.4), and we only find 19 objects within 1 kpc distance. Among these, we identify only one object as Class II, which is situated far from the Snake region.

4.4.2 Mass per length of filamentary structure

Theoretically, a self-gravitating isothermal cylinder has an infinite radius but a finite mass. The critical mass-to-length ratio at a temperature of 10 K is calculated as (Ostriker, 1964; Fiege & Pudritz, 2000):

$$\left(\frac{M}{L}\right)_{\rm cr} = \frac{2c_{\rm s}^2}{G} = 16\left(\frac{T}{10\,{\rm K}}\right)\,{\rm M}_\odot\,{\rm pc}^{-1}, \tag{4.4}$$

where G is the gravitational constant and $M_\odot$ is the Solar mass. If the actual mass-to-length ratio of the filament, $\left(\frac{M}{L}\right)_{\rm fil}$, exceeds the critical value, the filament will collapse radially. To estimate the mass of the filament, we use the following equation:

$$M_{\rm fil} = 1.13\times10^{-7}\times\sum_{i=1}^{n}\left(\frac{N({\rm H_2})}{{\rm cm}^{-2}}\right)_i\left(\frac{\theta}{''}\right)^2\left(\frac{d_{\rm cloud}}{\rm pc}\right)^2\mu_{\rm H_2}m_{\rm H}\,M_\odot, \tag{4.5}$$

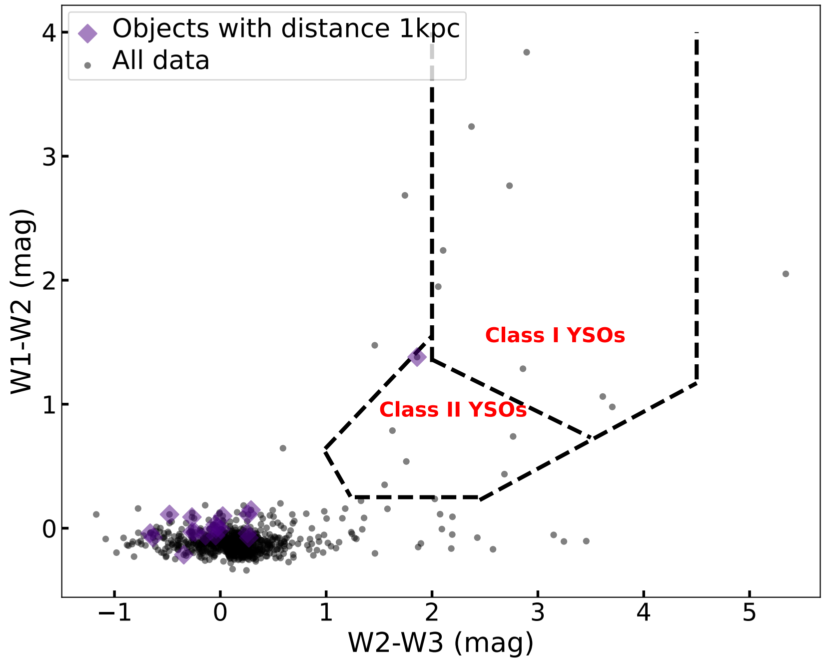

Figure 4.4: The W1-W2 versus W2-W3 color-color diagram of AGB candidates from the SPLICES survey. The dashed areas used by Koenig & Leisawitz (2014) to identify Class I and Class II YSOs are shown. Black dots represent all the data from SPLICES, and purple diamonds indicate objects within a distance of 1 kpc.

where the summation $\sum_{i=1}^{n}(N(\mathrm{H}_2)_i)$ includes contributions from n pixels within the filament area as introduced in Sect. 4.4.6, $m_{\mathrm{H}} = 1.67 \times 10^{-24}\,\mathrm{g}$ is the mass of a hydrogen atom, $\mu_{\mathrm{H}_2} = 2.8$ (from Kauffmann et al. 2008) is the mean molecular weight per hydrogen molecule, and $d_{\mathrm{cloud}} = 154\,\mathrm{pc}$ is the distance to the cloud, $\theta = 10''$ is the pixel size. We calculated the gas column density of the filament, $N(\mathrm{H}_2)$, from the visual extinction, A_{V} (Fig. 4.2). Using the relation provided by Bohlin et al. (1978), $N(\mathrm{H}_2) = 9.4 \times 10^{20} \times A_{\mathrm{V}}\,\mathrm{cm}^{-2}\,\mathrm{mag}^{-1}$, we converted A_{V} into the molecular hydrogen column density. The filament length is estimated to be $L = 2.4\,\mathrm{pc}$, with a detailed description of the measurement method provided in Sect. 4.4.6. The mass per unit length of the filament is determined to be $14.4\ M_{\odot}\,\mathrm{pc}^{-1}$, which is below the critical mass per unit length, $\left(\frac{M}{L}\right)_{\mathrm{cr}} = 22.4\,M_{\odot}\,\mathrm{pc}^{-1}$. This indicates that the Snake filament is stable against gravitational collapse. Consequently, this is likely the primary reason for the absence of star formation in this region.

4.4.3 Spatial Distribution of B-field

Figure 4.5 reveals two prominent peaks in the orientation of angles, which is evident in the histogram distribution (right panel). These two peaks are visible in the optical (blue), NIR (red), and submm (green) data, with their respective values marked as dashed vertical lines in the plot. Specifically, the optical and NIR data exhibit their first peaks within the range of approximately 85° to 102°, as highlighted in light blue in the right panel of Fig. 4.5. The optical data also show a second prominent peak at around 180°. In contrast, the submm data reveal two distinct peaks at 66° and 169°, with the second peak of the NIR data aligning closely with the second peak observed in the submm data. The accompanying plot (top panel of Fig.4.5) depicts the polarization angles as a function of right ascension, providing additional insights into how these peaks are associated with specific regions in the studied area. This visualization emphasizes the relationship between polarization angle and spatial distribution. As the right ascension decreases, the polarization angle transitions from vertical to horizontal, illustrating the dynamic nature of the polarization orientation (with respect to North) across the observed field. In contrast, the infrared data (in red color) illustrates a random distribution in both plots in Fig. 4.5. The overall polarization distribution across the entire region does not appear to follow any specific pattern. However, it is important to note that the infrared polarization vectors are low, resulting in low statistical significance, which could hinder the detection of well-defined patterns. Despite this limitation, a peak in the distribution can be observed around 80° to 100° (see the bottom panel of Fig. 4.5).

4.4.4 Polarisation efficiency

Figure 4.6 presents the scatter plots of polarization efficiency ($P_{\rm pol}/A_{\rm V}$) as a function of visual extinction ($A_{\rm V}$) in log-log space. The optical and NIR datasets are organized into 30 bins, represented by blue and red points, respectively. The error bars on each data point are calculated as the standard deviation of the polarization measurements within each bin, reflecting the measurement uncertainties in the analysis. The blue and red curves illustrate the density plots for the optical and NIR datasets, respectively. The optical and NIR data show a peak density within the visual extinction range of 1 to 3 magnitudes.

The plot includes two fitted lines corresponding to two datasets. The optical fit is represented by the equation: $P_{\rm pol}/A_{\rm V} = -0.73 \log A_{\rm V} + 0.04$. Conversely, the NIR fit is described by: $P_{\rm pol}/A_{\rm V} = -0.75 \log A_{\rm V} + 0.02$, which shows a slightly steeper decline in polarization efficiency with increasing visual extinction. The polarization efficiency exhibits a decrease at both optical and infrared wavelengths. This observation suggests that the mechanisms influencing polarization efficiency may differ between the two wavelengths.

The optical polarization is primarily associated with the diffuse cloud surrounding the Snake filament, while the infrared data predominantly trace slightly denser regions. However, both datasets in our analysis correspond to relatively low-density regions within the Snake filament, spanning a visual extinction range of 0.5 to 4.5 magnitudes (see Fig. 4.2). The slopes observed for both datasets indicate depolarization in this region, consistent

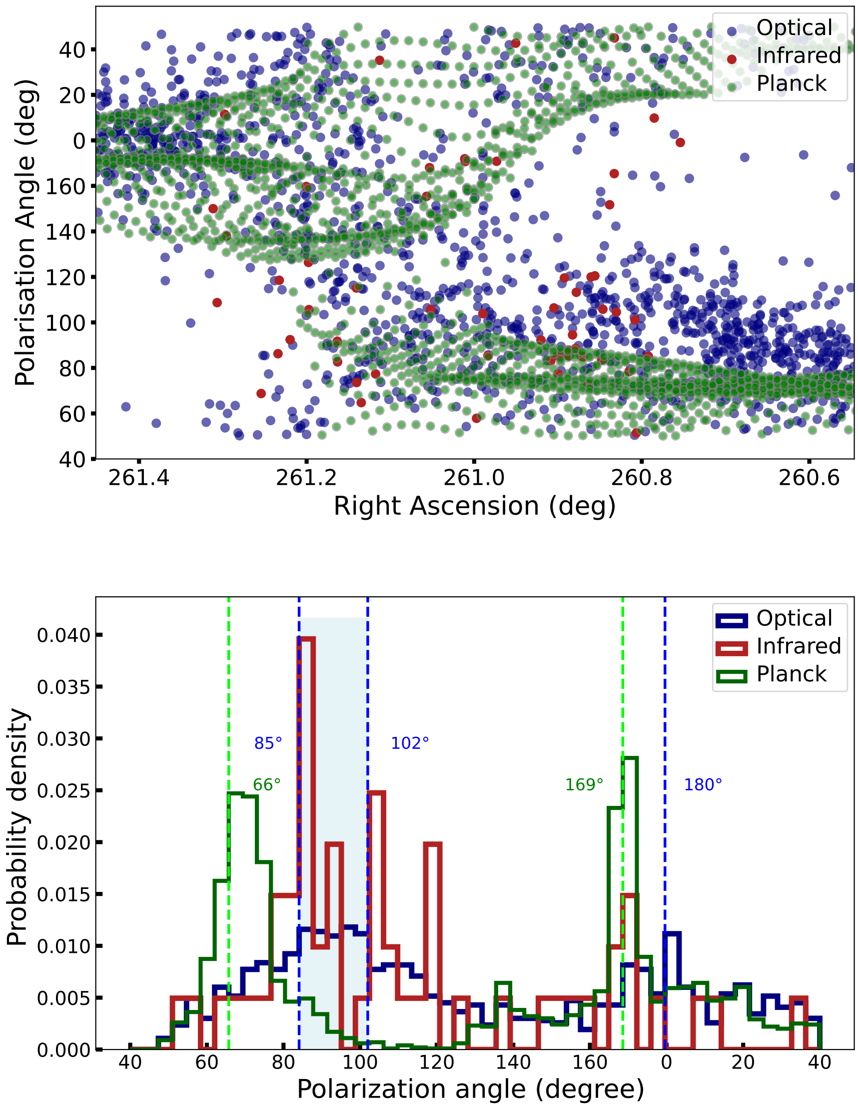

Figure 4.5: Distribution of polarization angles. Top panel: Distribution of polarization angles as a function of the right ascension of the field for the three dataset in optical, NIR and submm. Bottom panel: Histogram of the distribution of magnetic polarization angles for the same dataset. Optical data peaks are highlighted by blue-colored dashed lines, whereas submm dataset distribution peaks are highlighted by green-colored dashed lines.

with the radiative alignment theory (RAT, Lazarian & Hoang 2007b). As visual extinction increases, reduced radiation penetration within the cloud diminishes the effectiveness of radiative torques in aligning dust grains. As reported by Alves et al. (2014b), NIR polarisation measurements of the starless core in the Pipe Nebula yield α values of 1.0 for $A_{\rm V} < 9.5$ mag and 0.34 for $A_{\rm V} > 9.5$ mag. Redaelli et al. (2019b) determined a steep slope of $\alpha = 1.21$ for the FIR polarization data associated with the protostellar core IRAS 15398-3359. Similarly, Tabatabaei et al. (2024) derived a slope of 0.75 from NIR data of a filamentary structure in Barnard 59. Overall, the scatter plots demonstrate the relationship between polarization efficiency and visual extinction across optical and infrared datasets, providing insights into the dust properties and the physical conditions of the molecular clouds studied.

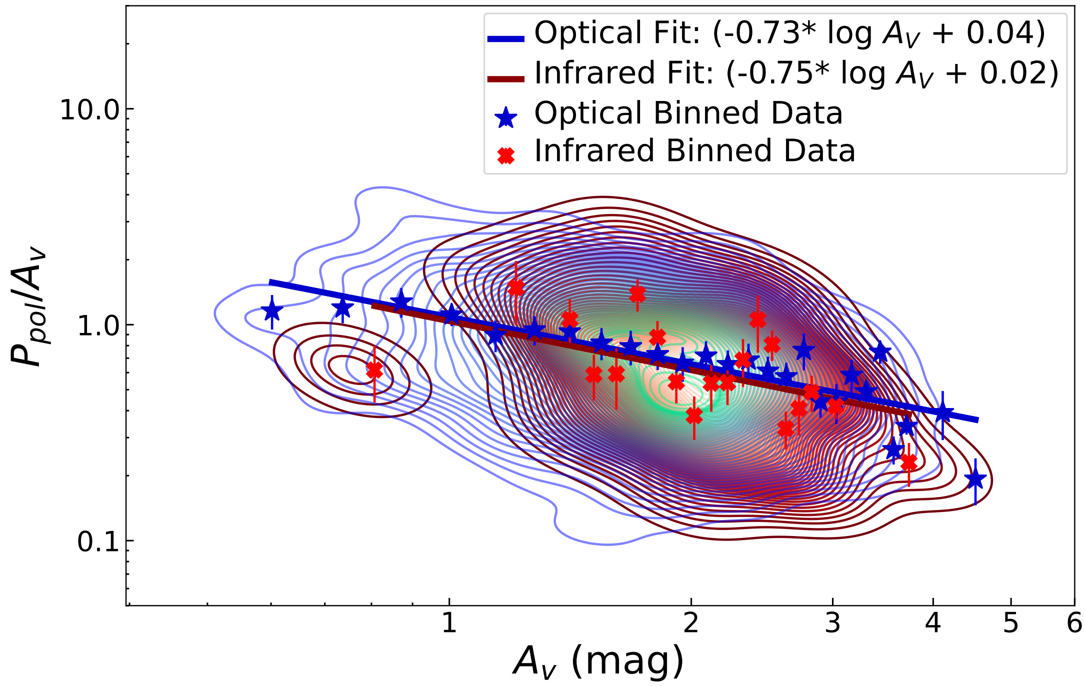

Figure 4.6: Scatter plots of the polarization efficiency ($P_{\rm pol}/A_{\rm V}$) as a function of the visual extinction ($A_{\rm V}$) in magnitudes in logarithmic scale. Measurement uncertainties are displayed as an error bar for each data point. Solid lines are the best fit for the datasets, as explained in the main text. The best-fit parameters are shown in the top-right corner.

4.4.5 Spectral line fitting

CO isotopologues are widely utilized to probe gas in molecular clouds at varying densities. The ^{13}CO (1-0) isotopologue is typically associated with tracing the diffuse outer regions of molecular clouds. In contrast, the rarer C^{18}O (1-0) line, with a critical density of $\sim 10^3\,{\rm cm}^{-3}$, serves as an excellent tracer for regions with higher column and volume densities (relative to ^{13}CO (1-0)), effectively avoiding saturation. In this section, we compare the polarization data with the gas kinematics using the complete set of NIR observations rather than limiting the analysis to data cross-matched with the `StarHorse` catalog (see

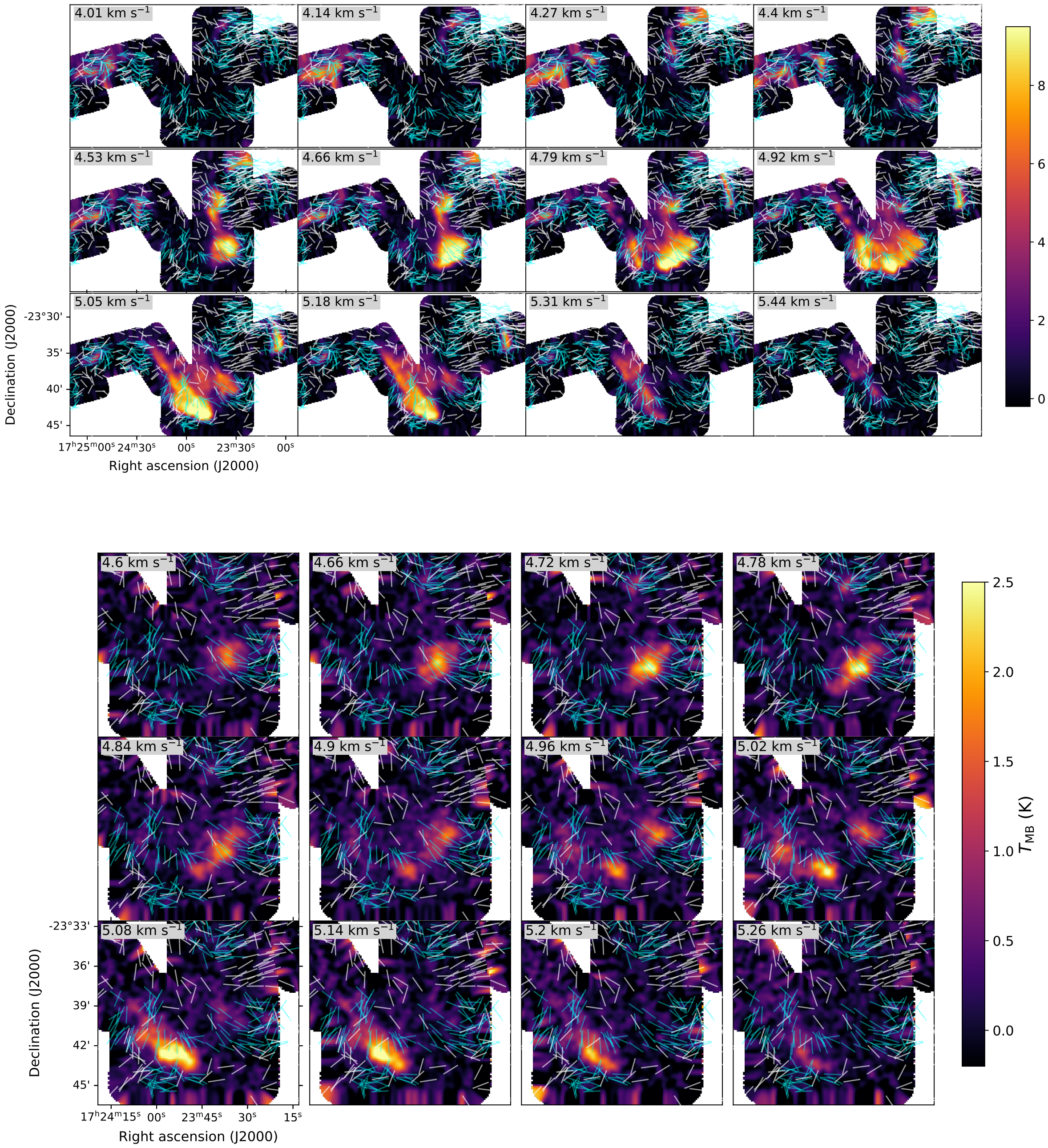

Figure 4.7: Top pannel: Channel maps between 4.01 and 5.44 $\mathrm{km\,s^{-1}}$ for the ^{13}CO (1-0) spectral cube, in 0.13 $\mathrm{km\,s^{-1}}$ steps. White and cyan segments illustrate B-field orientation in the optical (S/N>5) and infrared (S/N>3) bands, respectively. The velocity of each channel is shown on the top left of the panels. Bottom panel: Same as top panel, but for the C^{18}O (1-0) line. Channels are between 4.60 and 5.26 $\mathrm{km\,s^{-1}}$, in 0.06 $\mathrm{km\,s^{-1}}$ steps.

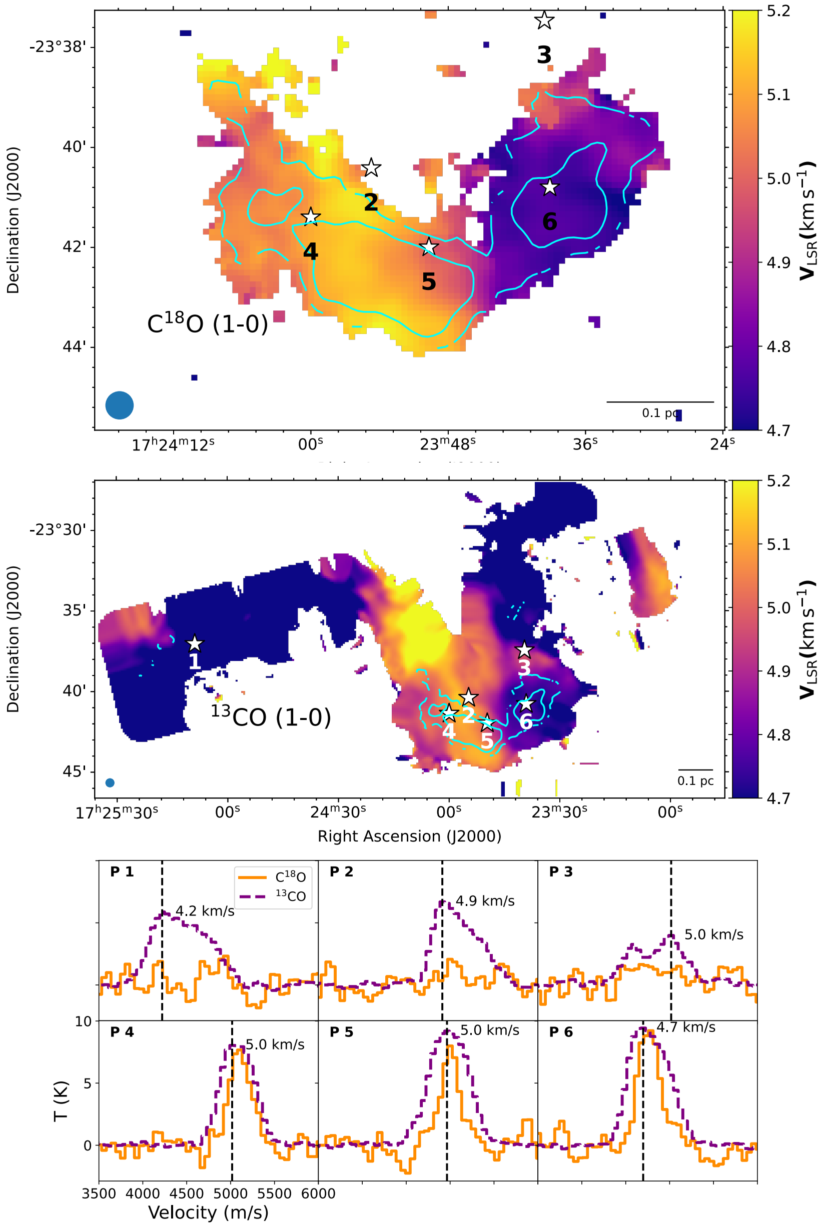

Figure 4.8: Top panel: Centroid velocity map of the C^{18}O (1-0) line. Middle panel: Centroid velocity map of the ^{13}CO (1-0) line. In both maps, we highlight six selected profiles at specific positions along the Snake, marked by white stars. The cyan contours represent the C^{18}O (1-0) integrated intensity at levels of 0.8 K and 1.6 K. The beam size is shown in the bottom-left corner, while the scale bar is displayed in the bottom-right corner. Bottom panel: Comparison of the six spectral profiles corresponding to the positions marked by white stars in both maps. The orange dashed profiles represent the C^{18}O (1-0) line multiplied by 5, while the purple solid profiles correspond to the ^{13}CO (1-0) line. The black dashed lines indicate the peak velocity of the ^{13}CO (1-0) line, with the velocity values labeled next to them.

Sect. 4.3.1). We established that no significant structures exist behind the Snake filament; therefore, all observed NIR data points are considered valid for this analysis.

Figure 4.7 displays the ^{13}CO (1-0) and C^{18}O (1-0) channel maps in 0.13 and 0.06 km s^{-1} steps, respectively. For both lines, the data presented have an S/N>3. Polarization vectors for optical (white) and NIR (cyan) wavelengths are overplotted on each panel. The ^{13}CO (1-0) emission at velocities lower than 4.4 km s^{-1} is confined to the east region of the filament, while higher velocities show more concentrated emission at the center of the filamentary structure. At the filament's center, velocities range from 4.53 km s^{-1} to 5.18 km s^{-1}, transitioning from west to east (see second row). While the C^{18}O (1-0) emission is only concentrated at the center of the filament, it appears at lower velocities on the western side of the map and shifts to higher velocities toward the east side.

The kinematic properties of the observed C^{18}O (1-0) molecular line were derived by fitting Gaussian profiles to each spectrum in the dataset using the Python package `pyspeckit` (Ginsburg & Mirocha, 2011b). A threshold of S/N $>$ 5 was applied to mask unreliable pixels, ensuring the fits were constrained to regions with sufficient signal. A single-Gaussian fit was performed across the unmasked pixels with initial parameter guesses refined iteratively using neighboring pixel values. Fits with residuals exceeding 2 $\times$ RMS or velocity dispersions (σ_v) broader than 0.35 km s^{-1} were masked and excluded. The resulting C^{18}O (1-0) model cube showed only 0.1 percent of the pixels had a bad fit, demonstrating the robustness of the one-Gaussian fitting approach. The top panel of Fig. 4.8 displays the centroid velocity map of the C^{18}O (1-0) line. The C^{18}O (1-0) line exhibits a narrow linewidth, ranging from $\sim$ 0.1 to 0.2 km s^{-1}, indicative of quiescent C^{18}O (1-0) gas dynamics in this region. Given that the sound speed in the region is $c_{\rm c}$ = 0.2 km s^{-1} (for T = 15K, from *Herschel* map), these velocity dispersions suggest that the motions are transonic (see Appendix C.1 for dispersion velocity map and sound speed calculation).

In contrast, the ^{13}CO (1-0) line exhibits more complex kinematics, particularly in the central regions of the Snake filament, where two velocity components are observed. Similar to C^{18}O (1-0), a single-Gaussian fit was first applied to pixels with S/N $>$ 4, followed by a dual-Gaussian fit for regions with significant residuals or broad line widths. Through visual inspection, we find that lines broader than 0.7 km s^{-1} exhibit profiles consistent with two velocity components. Based on this observation, we established a masking criterion that excludes pixels where the residuals exceed 2 $\times$ RMS and velocity dispersions broader than 0.7 km s^{-1} in the single-Gaussian fit. Accurately fitting the ^{13}CO (1-0) line with two Gaussian components in the central region of the Snake filament is challenging due to the line's high opacity, which exceeds a value of 1 (see Sect. 4.3.2). The middle panel of Fig. 4.8 presents the centroid velocity map of the ^{13}CO (1-0) line, derived using a single-Gaussian fitting. The central velocities ($V_{\rm LSR}$) of the ^{13}CO (1-0) line range approximately from $\sim$ 4.7km s^{-1} to $\sim$ 5.2 km s^{-1}, increasing from west to east.

A similar velocity gradient is observed in the C^{18}O (1-0) line, with velocities increasing from lower to higher values from west to east side. The bottom panel of Fig. 4.8 presents six spectral profiles at different positions along the Snake filament for both ^{13}CO (1-0) and C^{18}O (1-0) lines. These profiles highlight the saturation of the ^{13}CO (1-0) line, which prevents an accurate Gaussian fit. The orange dashed profiles represent the C^{18}O (1-0)

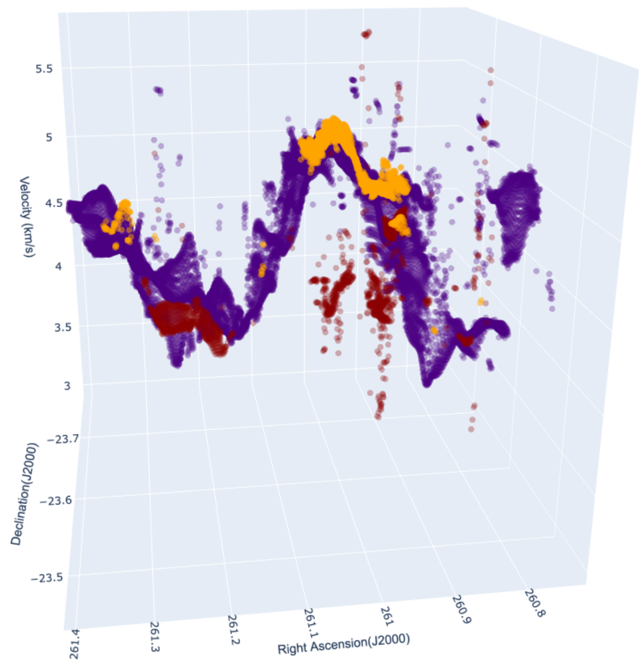

Figure 4.9: The PPV plot illustrates the kinematics of the ^{13}CO (1-0) and C^{18}O (1-0) lines. Each data point represents the spatial location and centroid velocity of a Gaussian component, with colors distinguishing different Gaussian fits. The centroid velocity of the C^{18}O (1-0) line is shown in orange, while the purple and red points correspond to the brighter and fainter intensity components of the ^{13}CO (1-0) line, respectively.

line with its temperature scaled by a factor of 5 for better comparison with the ^{13}CO (1-0) profile. The purple profiles correspond to the ^{13}CO (1-0) line. For positions 1 to 3 (first row of the plot), the C^{18}O (1-0) line shows no detectable signal, whereas the ^{13}CO (1-0) line exhibits a strong signal with two distinct velocity components. In positions 4 to 6 (second row of the plot), both lines show clear signals, each with a single velocity component. The peak velocities of the ^{13}CO (1-0) and C^{18}O (1-0) lines are in good agreement, as indicated by the black vertical dashed lines.

Figure 4.9 presents the 3D position-position-velocity (PPV) diagram, illustrating the C^{18}O (1-0) line in orange and the two velocity components of the ^{13}CO (1-0) line in purple and red, respectively. The higher velocity component of the ^{13}CO (1-0) line overlaps significantly with the velocity of the C^{18}O (1-0) line (see the orange data point and purple data point in the Fig. 4.9). From Figures 4.8 and 4.9, we conclude that both gas tracers follow the same cloud, exhibiting similar velocities. The gas shows lower velocities at both ends of the Snake filament, with velocities increasing toward the central region of the filamentary structure, which corresponds to the denser part of this region.

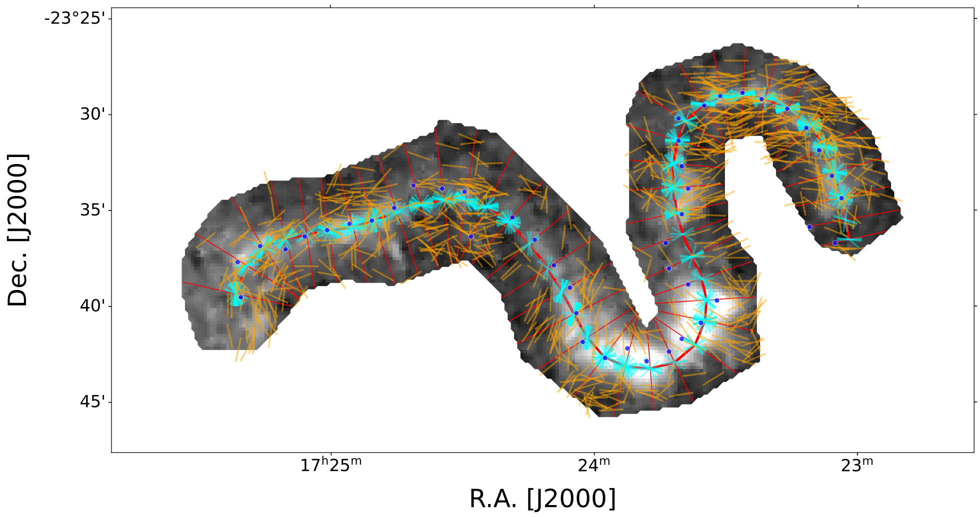

Figure 4.10: Dust extinction map illustrating the masked filamentary structure. The spine of the filament is outlined by a prominent red curve, while the thin red lines indicate the locations of perpendicular cuts. Blue circles represent peak pixel intensity along each cut. The orange vectors, representing optical(S/N>5) and infrared (S/N>3) polarization segments. The cyan vectors are projections of all the orange polarization vectors onto the spine. Each polarization vector was projected by finding its closest point on the spine and shifting it accordingly.

4.4.6 Filamentary structure

To further characterize the Snake's filamentary structure and its relationship with polarization data, we use the Python package `radfill` (Zucker & Chen 2018). The spine of the filament is defined by radfil by using the `fil_finder` package (Koch & Rosolowsky 2015) based on the Av map and mask map provided. We extracted evenly spaced cuts perpendicular to the spine at intervals corresponding to every 7 pixels along its length. Consequently, the center of the resulting profiles aligns with the peak value of Av. Using this spine, we determine a filament length of 2.3 pc. Figure 4.10 illustrates the spine in a thick red curve and the perpendicular cuts. The plot also includes polarization data from optical and infrared wavelengths, with the orange vectors representing the polarization angles. The cyan vectors are projections of the orange polarization vectors onto the spine. This projection was done by finding each polarization vector's closest point on the spine and shifting it accordingly.

Our goal is to analyze how the polarization angles change as we move along the filament's spine. The behavior of polarization vectors along the spine provides critical insights into the magnetic field geometry. Specifically, analyzing the relationship between the polarization vectors and the filament's curvature allows us to evaluate whether the vectors are predominantly aligned with the filament (parallel) or if there are regions where they deviate significantly (perpendicular).

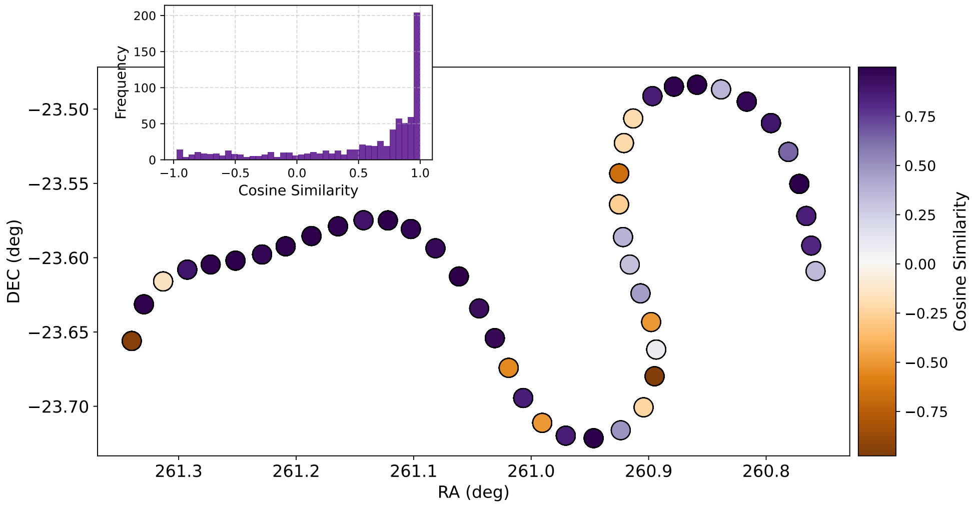

Figure 4.11: Color-coded scatter plot of cosine similarities between the polarization vectors and the tangent vectors to the spine of the Snake filament. The histogram in the top-left panel shows the distribution of cosine similarity values, highlighting the alignment between the two vector sets.

We can quantify this by calculating the cosine similarity between the polarization vectors and the tangent vectors to the spine. Cosine similarity values close to $+1$ and -1 indicate that the polarization vectors are aligned with the spine, while zero values suggest they are perpendicular to each other. Figure 4.11 presents a color-coded scatter plot of cosine similarities. Darker-colored circles (dark purple and dark orange) represent locations where the polarization vectors are aligned with the tangent of the spine at that position, while lighter-colored circles (light purple and light orange) indicate regions along the Snake filament where the two vectors tend to be perpendicular to each other. Polarization vectors are predominantly parallel to the spine direction at both ends of the Snake filament, as indicated by values close to $+1$ in Fig. 4.11. In contrast, near the central region of the filament, where the gas is denser, the polarization vectors tend to be more perpendicular to the spine. The histogram inset in the top-left corner of Fig. 4.11 shows a strong peak near $+1$, indicating that, across the entire filament, most polarization vectors are aligned with the spine direction at their respective positions. However, any spread in the values indicates regions where the polarization direction differs from the spine's orientation, telling us the complexity of the filament's structure.

4.5 Summary

In this work, we investigated the magnetic field geometry and kinematic properties of the Snake filament by combining archival submillimeter polarimetry from Planck and molecular line data from IRAM with new optical and NIR polarization measurements. Our analysis confirms that the Snake is the dominant dust structure along the line of sight within 2 kpc of the Sun, with no significant molecular structures located beyond this distance. As a result, the observed polarization angles of background stars trace the magnetic field associated with the Snake filament. Additionally, we determined the distance of the source to be 154 pc using Gaia data (see Sect. 4.4.1). This distance puts the Snake filament at the same distance as the Pipe Nebula.

The Snake filament is gravitationally stable. The estimated mass-to-length ratio is below the critical threshold, explaining the lack of star formation in the region. The polarization efficiency ($P_{\rm pol}/A_{\rm V}$) decreases with increasing visual extinction, with fitted slopes of 0.73 for optical data and 0.94 for NIR data. This behavior suggests depolarization in denser regions where reduced radiation penetration weakens dust grain alignment.

Kinematic analysis reveals a velocity gradient along the filament in both ^{13}CO (1-0) and C^{18}O (1-0) data. The C^{18}O (1-0) line, tracing denser regions, exhibits well-constrained single-Gaussian fits, while the ^{13}CO (1-0) line shows more complex kinematics, including multiple velocity components in the denser central region. Furthermore, the polarization vectors along the filament's spine exhibit strong alignment with the filament's spine tangent, as indicated by cosine similarity values peaking near +1. This alignment highlights the significant role of magnetic fields in shaping the filament's structure.

These results demonstrate that the Snake filament is immersed in a well-ordered magnetic field, which plays a critical role in maintaining its structural coherence and stability. The observed polarization and kinematics suggest that magnetic fields significantly influence the dynamics of the filament, shaping its evolution. This study contributes to understanding the role of magnetic fields in filamentary structures and their connection to star formation processes.

Acknowledgements Elena Redaelli acknowledges the support from the Minerva Fast Track Program of the Max Planck Society. G. Franco acknowledges the partial support from the Brazilian agencies CNPq and FAPEMIG. This research has used data from the *Herschel* Gould Belt survey (HGBS) project (http://gouldbelt-herschel.cea.fr). The HGBS is a *Herschel* Key Programme jointly carried out by SPIRE Specialist Astronomy Group 3 (SAG 3), scientists of several institutes in the PACS Consortium (CEA Saclay, INAF-IFSI Rome, and INAF-Arcetri, KU Leuven, MPIA Heidel- berg), and scientists of the *Herschel* Science Center (HSC). This work has made use of data from the European Space Agency (ESA) mission *Gaia* (https://www.cosmos.esa.int/gaia), processed by the *Gaia* Data Processing and Analysis Consortium (DPAC, https://www.cosmos.esa.int/web/gaia/dpac/consortium). Funding for the DPAC has been provided by national institutions, in particular the institutions participating in the *Gaia* Multilateral Agreement. The authors express their gratitude to Jaime Pineda for his valuable support with the data reduction process of IRAM data.

Chapter 5

Conclusions and future perspective

In this thesis, I presented the results of three projects investigating the role of magnetic fields in low-mass star formation region. These studies focused on the interplay between magnetic fields and kinematics in protostellar core and filamentary structures, using observations of molecular gas and polarization to analyze their dynamics and stability. This chapter summarizes the key findings from each project and discusses potential directions for future work in this area.

5.1 Summary of this thesis

In Chapter 2, I planed to explore the relationship between kinematics and magnetic fields during the earliest stages of the star formation process. Observations of protostellar envelopes are crucial for gaining a deeper understanding of gravitational collapse, a fundamental step toward star and planet formation. From a theoretical perspective, magnetic fields play a significant role in the early stages of star formation, particularly during the main accretion phase. To investigated this, we observed the molecular lines $C^{18}O$ (2–1) and DCO^+ (3–2) toward the Class 0 young stellar object IRAS15398-3359, using data obtained with the Atacama Pathfinder EXperiment (APEX) single-dish antenna, which provides an angular resolution of 28". We implemented a multi-component Gaussian fitting on the molecular data to study the kinematics. In addition, we used previous polarization observations on this source to predict the influence of the magnetic field on the core. The velocity gradient along the central object can be explained as an ongoing outflow motion. We reported the flowing of material from the filament toward the central object, and the merging of two velocity components in the $C^{18}O$ (2-1) emission around the protostar position, probably due to the merging of filamentary clouds. Our analysis showed that the large-scale magnetic field line observed previously is preferentially aligned to the rotation axis of the core.

In Chapter 3, I investigated how magnetic fields influence the properties and kinematics of a filament located to the east of the Barnard 59 clump in the Pipe Nebula. Understanding the physical relationship between dense cores and the filaments embedding them is crucial for constructing a comprehensive picture of star formation. To determine the magnetic field configuration, we utilized near-infrared polarization observations and applied the Davis–Chandrasekhar–Fermi method to estimate the magnetic field strength in the plane of the sky. Complementary data from the *James Clerk Maxwell Telescope* (*JCMT*) were used to analyze the kinematics of the filament, focusing on $C^{18}O$ and ^{13}CO $J = 3 - 2$ transitions. Additionally, we modeled the filament's radial density profile using polytropic cylindrical models. Our findings suggested that the filament is stable against radial collapse, with radial support provided by factors other than thermal pressure. Moreover, based on previous emission line observations, we proposed that gas is flowing toward the hub. While, the $C^{18}O$ (3–2) nonthermal motions indicated that the cloud remains in a quiescent state.

In Chapter 4, we analyzed the influence of magnetic fields on the structure and dynamics of the Snake filament using both polarization data and molecular line observations. Our objective was to investigate the role of magnetic fields in shaping the filamentary structure and to explore its internal kinematics. We conducted polarization observations in the optical and near-infrared bands using the 1.6 m and 60 cm telescopes at the Observatório do Pico dos Dias/ Laboratório Nacional de Astrofísica, Brazil. Additionally, molecular line observations of the $C^{18}O$ (1-0) and ^{13}CO (1-0) transitions were obtained with the IRAM 30m telescope. Our analysis focused on characterizing the polarization and gas properties within the filament, particularly the magnetic field orientation and its relationship with the filament's structure. The results showed that the polarization vectors align with the filament's spine, indicating a predominantly parallel magnetic field configuration in the lower-density regions. A velocity gradient along the filament was detected in both $C^{18}O$ (1-0) and ^{13}CO (1-0) lines, with ^{13}CO (1-0) tracing the denser gas regions. Furthermore, polarization efficiency was found to decrease with increasing visual extinction, consistent with reduced grain alignment in higher-density environments. Finally, the filament's mass-to-length ratio was below the critical threshold for gravitational collapse, indicating stability.

5.2 Prospective work

The recently commissioned Simultaneous Polarimeter and Rapid Camera in four bands (SPARC4) offers an unprecedented opportunity to investigate the properties of the interstellar medium at the Pico dos Dias Observatory. Simultaneous observations in four filters allow us to study how the polarization of starlight caused by the ISM varies with wavelength, enabling us to infer the properties of the dust grains responsible for the observed polarization. The four filters used by SPARC4 are very similar to the g,r,i,z bands of the Sloan Digital Sky Survey. Given our prior experience studying the Pipe Nebula, we selected 40 fields containing pre-stellar cores with varying degrees of interstellar extinction (A_v) for this project. The main goal is to investigate the physical properties of the dust grains in these cores and verify whether there are differences in their properties as a function of spatial distribution all over the complex and/or as a function of the core's interstellar extinction.

This project focuses on the relationship between interstellar polarization and wavelength. Using polarization data from the aforementioned observations, we will analyze the correlation between the wavelength of maximum polarization (λ_{max}) and extinction (A_{v}) in different cores. According to radiative alignment torque (RAT) theory (Hoang & Lazarian 2008), anisotropic radiation spins up dust grains, aligning them with the magnetic field. Grain size is a critical factor in this model, as λ_{max} depends on grain size and reddening along the line of sight. The study aims to extend the λ_{max}-A_{v} relation to higher extinction values than previous studies, offering insights into dust grain alignment under different ISM conditions.

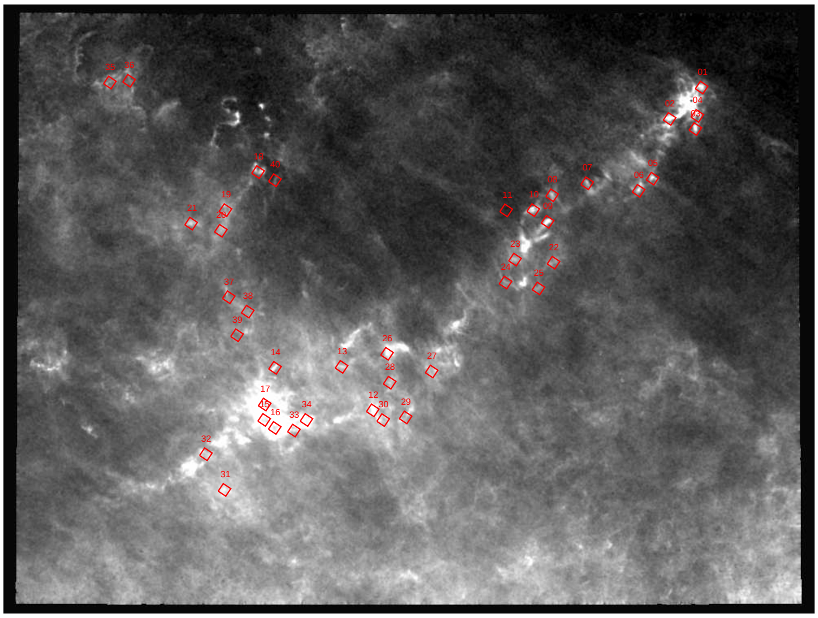

Figure 5.1: Distribution of 40 selected cores across the plane of the Pipe Nebula, plotted on top of the extinction map from Román-Zúñiga et al. (2010) (Credit: Prof. G. Franco).

Using these polarization data, we will estimate λ_{max} for each core via the Serkowski relation (Serkowski 1973; Serkowski et al. 1975):

$$\frac{P_\lambda}{P_{\mathrm{max}}} = \exp\left[-1.15\left(\ln\left(\frac{\lambda_{\mathrm{max}}}{\lambda}\right)\right)^2\right] \tag{5.1}$$

where P_λ is the polarization at wavelength λ, P_{max} is the maximum polarization, and λ_{max} is the wavelength corresponding to P_{max}. These findings will be combined with photometric data from the Gaia DR3 release and the STARHORSE catalog to map dust grain properties across the Pipe Nebula and evaluate the $\lambda_{\mathrm{max}} - A_{\mathrm{v}}$ relation.

Previous studies (Andersson & Potter 2007) have established a correlation between λ_{max} and A_{v} for extinction up to 4 magnitudes. For the Taurus dark cloud, the following relation was found:

$$\lambda\text{max} = (0.53 \pm 0.01\ \mu\text{m}) + (0.020 \pm 0.004\ \mu\text{m/mag})A_V \tag{5.2}$$

If RAT theory is correct, this relationship should persist at higher extinction levels, where few observations exist. We aim to extend this analysis to higher A_v values (from $A_\text{v} = 4.3$ mag to 20.7 mag), improving our understanding of dust grain alignment and the role of magnetic fields across different regions of the Pipe Nebula.

In April and June 2024, we utilized SPARC4 at LNA/OPD to collect data for this project (PI: Prof. Dr. Gabriel Franco). A preliminary analysis of the data (see Fig. 5.2) indicates that dust grains in one of the cores of the Barnard 59 region, presumably the most evolved part of the complex, exhibit distinct properties compared to grains in the Bowl, believed to be the least evolved region. We found that dust grains in B59 are larger than in the bowl, which fits nicely with the scenario of distinct evolutionary stages (see Fig. 5.2). B59 is more evolved and hence associated with larger grain growth with respect to the very early-on stage of the bowl. Despite unfavorable weather conditions during these nights, the results demonstrate the feasibility of the project and validate the capabilities of the SPARC4 camera. Additionally, our observing list includes many lines of sight not previously studied by Alves et al. (2008) or Franco et al. (2010), providing complementary insights. The project also serves as a valuable test of the SPARC4 camera's performance.

Encouraged by these preliminary results, we have applied for follow-up observations, and our proposal for OPD has been accepted (PI: F. Tabatabaei). We have been allocated additional observation time: four nights in May and four nights in June 2025. These observations will allow us to complete our data collection and further investigate this project.

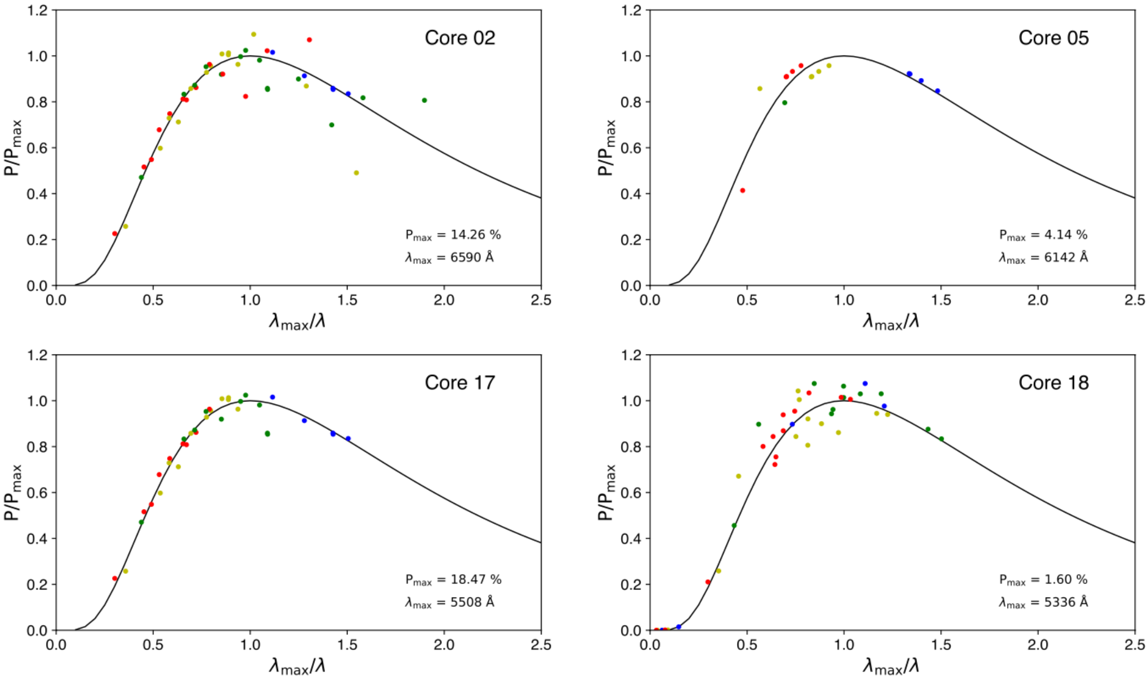

Figure 5.2: Examples of the Serkowski relations (Eq. 5.1) derived for observed cores in the Pipe Nebula region are shown. Each color represents data obtained from a different filter of the polarimeter. Specifically, blue corresponds to the g-filter, green to the r-filter, yellow to the i-filter, and red to the z-filter. The fitted relations indicate that the dust grains in the B59 region (Cores 02 and 05) are larger than those in the Bowl (Core 17). Core 18, located outside the main body of the Pipe Nebula, is part of the "smoke" region (Credit: Prof. G. Franco).

Appendix A

Appendices for Chapter 2

A.1 Positions of spectral grid

Figure A.1 shows the position of each spectra in Fig. refchannel. There are 40 black dots that show the exact location of each spectrum at an 18 arcsec interval from each other.

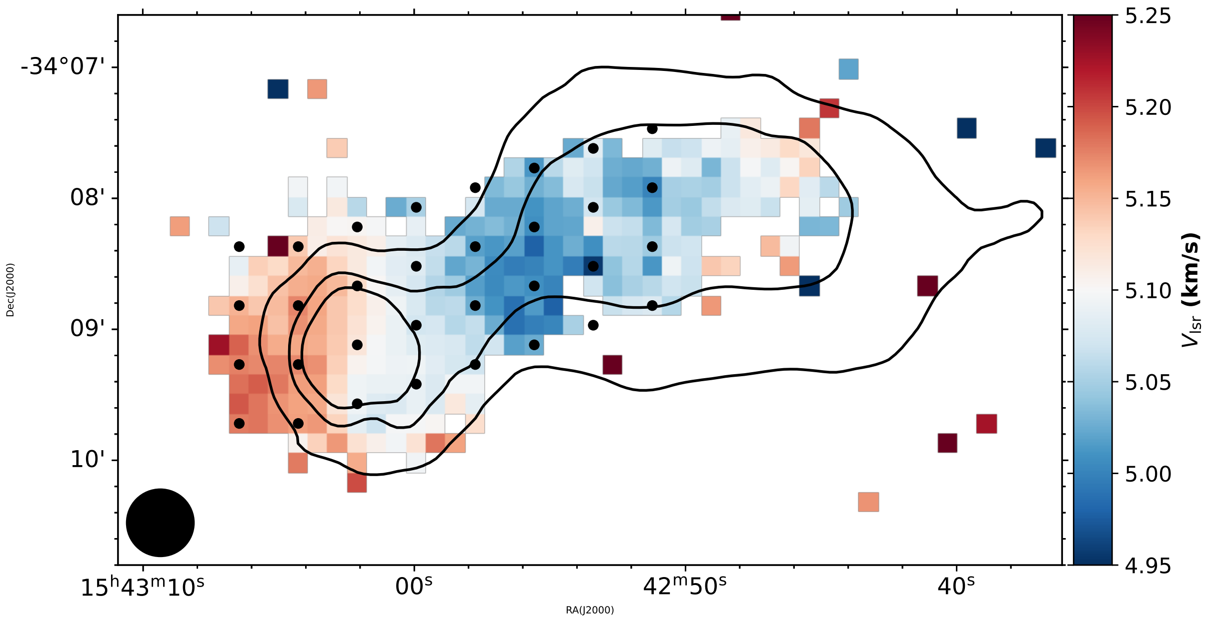

Figure A.1: Map of centroid velocity of DCO^+ (3-2). The black dots show the position of each spectrum. Overlaid in black contours is the H_2 column density (levels:[1.0,1.5,2.0] 10^{22} cm^{-2}).

Appendix B

Appendices for Chapter 3

B.1 Residual of the Gaussian fit

We fit a single Gaussian component to the spectra in the $C^{18}O$ (3-2) and ^{13}CO (3-2), using the Python PYSPECKIT library (citealtginsburg11). All spectra that have a peak signal-to-noise ratio lower than 3.5 are excluded from the analysis for the case of $C^{18}O$ (3-2) and lower than 4.5 (3-2) for ^{13}CO. Figure refresiduals shows the positions with bad fit for $C^{18}O$ and ^{13}CO emission lines. Red pixels display the places where the single Gaussian fit fails. We define them as places that have a residual higher than 2 × rms, and that Gaussian fits with a width broader than 0.35 km s^{-1} for both lines.

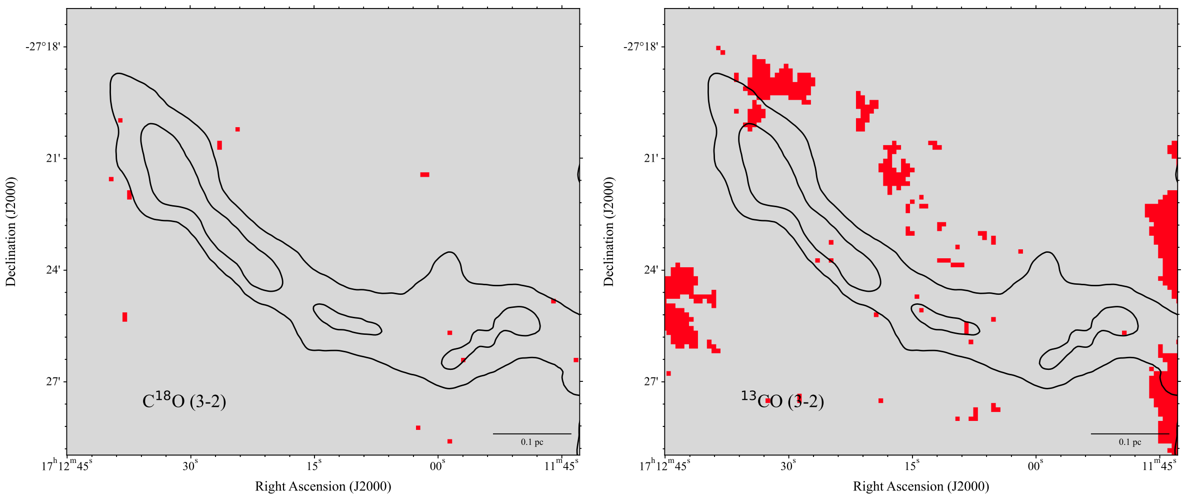

Figure B.1: Positions where the Gaussian fit fails for $C^{18}O$ (3-2) and ^{13}CO (3-2), shown in the top and bottom panels, respectively. Contours shows the column density of H_2 with levels [4,6] $\times 10^{22}$ cm^{-2}. Scale bars are at the bottom right of each panel.

B.2 Dust temperature map

Figure B.2 represents the dust temperature map of the filament from *Herschel* data. The three regions (R1, R2, and R3) used in the analysis are marked by black rectangles.

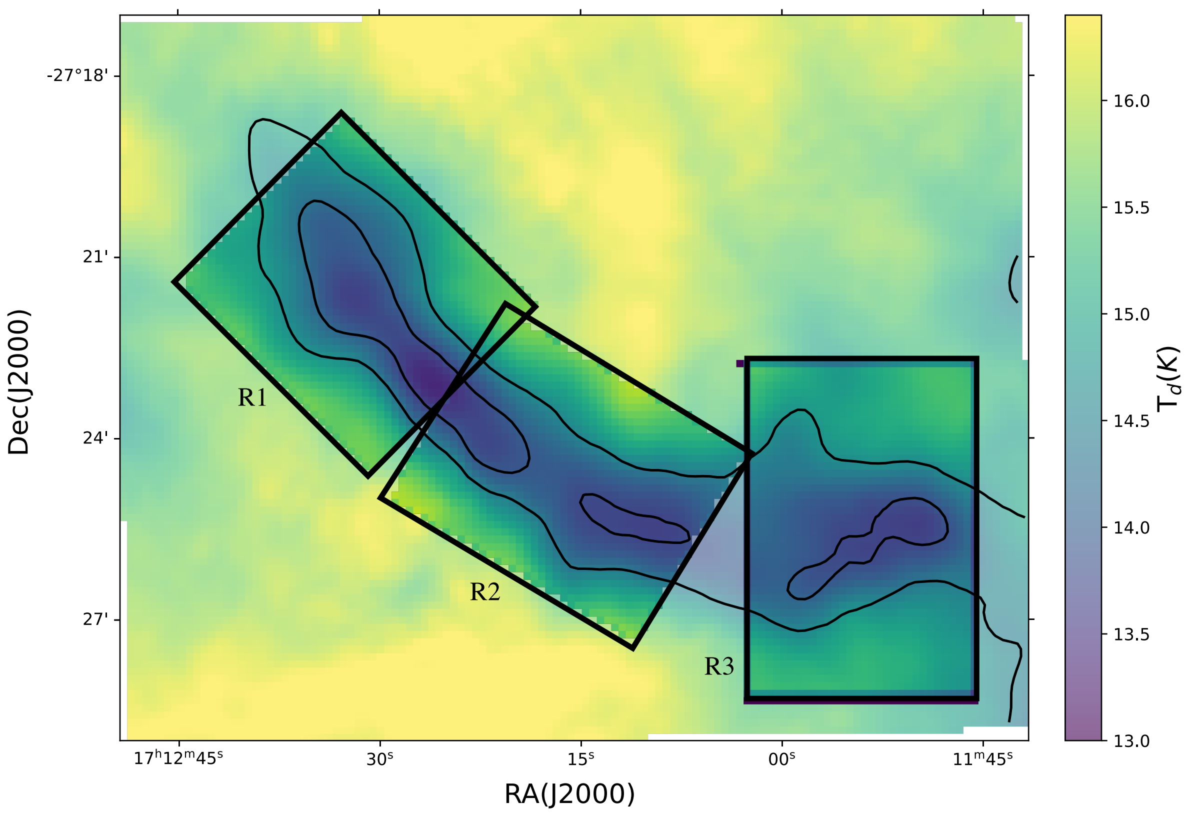

Figure B.2: Dust temperature map of the filament. The black rectangles display three regions of the filament. Contours show the column density of H_2 with levels [4,6] $\times 10^{22}$ cm^{-2}.

Appendix C

Appendices for Chapter 4

C.1 Velocity dispersion map $C^{18}O$ (1-0)

The linewidth of the observed $C^{18}O$ (1-0) molecular line was determined by fitting Gaussian profiles to each spectrum in the data cube. Figure C.1 illustrates the derived velocity dispersion map, σ_{v}, highlighting the narrow linewidths of the $C^{18}O$ (1-0) emission, with values typically around 0.1 $\mathrm{km\,s^{-1}}$ to 0.2 $\mathrm{km\,s^{-1}}$. The isothermal sound speed was obtained from:

$$c_s = \sqrt{\frac{k_B T}{\mu m_H}}, \tag{C.1}$$

where $\mu = 2.37$ (Kauffmann et al., 2008) is the mean molecular weight per free particle and m_{H} is the mass of hydrogen atom. we used the dust temperature, $T_d = 15\mathrm{K}$ from *Herschel* map as a proxy for the gas kinetic temperature.

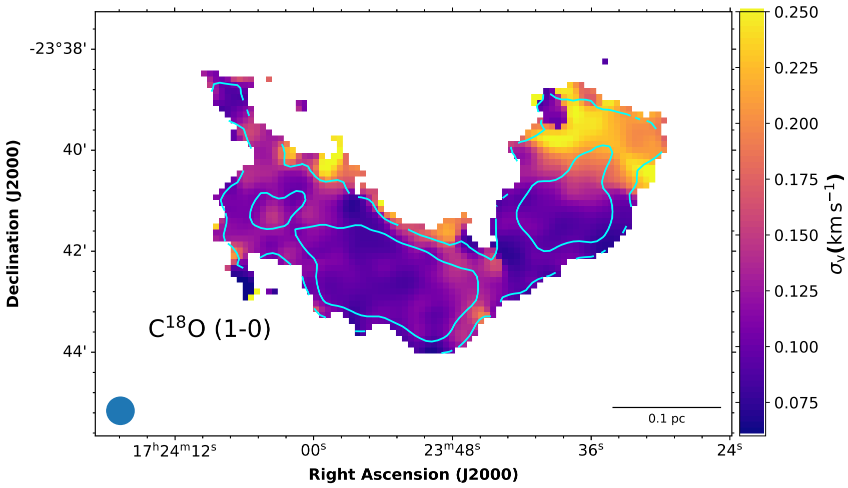

Figure C.1: Velocity dispersion ($\sigma_{\rm V}$) map of the $C^{18}O$ (1-0) line. The cyan contours represent the $C^{18}O$ (1-0) integrated intensity at levels 0.8 and 1.6 K. The beam size is indicated in the bottom-left corner, while the scale bar is displayed in the bottom-right corner.

Bibliography

Alves F. O., Franco G. A. P., 2007, A&A, 470, 597

Alves F. O., Franco G. A. P., Girart J. M., 2008, A&A, 486, L13

Alves F. O., Frau P., Girart J. M., Franco G. A. P., Santos F. P., Wiesemeyer H., 2014a, A&A, 569, L1

Alves F. O., Frau P., Girart J. M., Franco G. A. P., Santos F. P., Wiesemeyer H., 2014b, A&A, 569, L1

Anders F., et al., 2022, A&A, 658, A91

Andersson B. G., Potter S. B., 2007, ApJ, 665, 369

Andersson B. G., Lazarian A., Vaillancourt J. E., 2015, ARA&A, 53, 501

Andre P., Ward-Thompson D., Barsony M., 1993a, ApJ, 406, 122

André P., Ward-Thompson D., Barsony M., 1993b, ApJ, 406, 122

Andre P., Ward-Thompson D., Barsony M., 2000, in Mannings V., Boss A. P., Russell S. S., eds, Protostars and Planets IV. p. 59 (`arXiv:astro-ph/9903284`), doi:10.48550/arXiv.astro-ph/9903284

André P., et al., 2010a, A&A, 518, L102

André P., et al., 2010b, A&A, 518, L102

André P., et al., 2010c, A&A, 518, L102

André P., Di Francesco J., Ward-Thompson D., Inutsuka S. I., Pudritz R. E., Pineda J. E., 2014, in Beuther H., Klessen R. S., Dullemond C. P., Henning T., eds, Protostars and Planets VI. pp 27–51 (`arXiv:1312.6232`), doi:10.2458/azu_uapress_9780816531240-ch002

Arzoumanian D., et al., 2011, A&A, 529, L6

Arzoumanian D., et al., 2019, A&A, 621, A42

Ashby M. L. N., et al., 2023, ApJ, 949, 105

Auddy S., Basu S., Kudoh T., 2016, ApJ, 831, 46

Bacmann A., Lefloch B., Ceccarelli C., Castets A., Steinacker J., Loinard L., 2002, A&A, 389, L6

Barnes A. T., Henshaw J. D., Caselli P., Jiménez-Serra I., Tan J. C., Fontani F., Pon A., Ragan S., 2018, MNRAS, 475, 5268

Benedettini M., et al., 2018, A&A, 619, A52

Bergin E. A., Tafalla M., 2007, ARA&A, 45, 339

Bjerkeli P., Jørgensen J. K., Brinch C., 2016, A&A, 587, A145

Bohlin R. C., Savage B. D., Drake J. F., 1978, ApJ, 224, 132

Bolatto A. D., Wolfire M., Leroy A. K., 2013, ARA&A, 51, 207

Bontemps S., et al., 2010, A&A, 518, L85

Bourke T. L., Myers P. C., Robinson G., Hyland A. R., 2001, ApJ, 554, 916

Brauer R., Wolf S., Reissl S., 2016, A&A, 588, A129

Brooke T. Y., et al., 2007, ApJ, 655, 364

Buckle J. V., et al., 2009, MNRAS, 399, 1026

Burge C. A., Van Loo S., Falle S. A. E. G., Hartquist T. W., 2016, A&A, 596, A28

Carrasco J. M., et al., 2021, A&A, 652, A86

Caselli P., Walmsley C. M., Terzieva R., Herbst E., 1998, ApJ, 499, 234

Caselli P., Walmsley C. M., Tafalla M., Dore L., Myers P. C., 1999, ApJ, 523, L165

Caselli P., Walmsley C. M., Zucconi A., Tafalla M., Dore L., Myers P. C., 2002a, ApJ, 565, 331

Caselli P., Walmsley C. M., Zucconi A., Tafalla M., Dore L., Myers P. C., 2002b, ApJ, 565, 344

Ceccarelli C., et al., 2023, in Inutsuka S., Aikawa Y., Muto T., Tomida K., Tamura M., eds, Astronomical Society of the Pacific Conference Series Vol. 534, Protostars and Planets VII. p. 379

Chambers K. C., et al., 2016, arXiv e-prints, p. arXiv:1612.05560

Chandrasekhar S., Fermi E., 1953, ApJ, 118, 113

Chen H., Myers P. C., Ladd E. F., Wood D. O. S., 1995, ApJ, 445, 377

Chen H.-R. V., et al., 2019, ApJ, 875, 24

Cho J., Yoo H., 2016, ApJ, 821, 21

Cortes P. C., et al., 2016, ApJ, 825, L15

Coudé S., et al., 2019, ApJ, 877, 88

Crutcher R. M., 1999, ApJ, 520, 706

Crutcher R. M., 2012a, ARA&A, 50, 29

Crutcher R. M., 2012b, ARA&A, 50, 29

Crutcher R. M., Troland T. H., Goodman A. A., Heiles C., Kazes I., Myers P. C., 1993, ApJ, 407, 175

Crutcher R. M., Wandelt B., Heiles C., Falgarone E., Troland T. H., 2010, ApJ, 725, 466

Curtis E. I., Richer J. S., Buckle J. V., 2010, MNRAS, 401, 455

Cutri R. M., et al., 2003, 2MASS All Sky Catalog of point sources.

Cutri R. M., et al., 2013, Explanatory Supplement to the AllWISE Data Release Products, Explanatory Supplement to the AllWISE Data Release Products, by R. M. Cutri et al.

Davis L., 1951, Physical Review, 81, 890

Doi Y., et al., 2021, ApJ, 923, L9

Duarte-Cabral A., Chrysostomou A., Peretto N., Fuller G. A., Matthews B., Schieven G., Davis G. R., 2012, A&A, 543, A140

Dunham M. M., et al., 2014, in Beuther H., Klessen R. S., Dullemond C. P., Henning T., eds, Protostars and Planets VI. pp 195–218 (`arXiv:1401.1809`), doi:10.2458/azu_uapress_9780816531240-ch009

Dzib S. A., Loinard L., Ortiz-León G. N., Rodríguez L. F., Galli P. A. B., 2018a, ApJ, 867, 151

Dzib S. A., Loinard L., Ortiz-León G. N., Rodríguez L. F., Galli P. A. B., 2018b, ApJ, 867, 151

Edenhofer G., Zucker C., Frank P., Saydjari A. K., Speagle J. S., Finkbeiner D., Enßlin T. A., 2024, A&A, 685, A82

Elmegreen B. G., 2000, ApJ, 530, 277

Evans Neal J. I., et al., 2009, ApJS, 181, 321

Evans Neal J. I., Di Francesco J., Lee J.-E., Jørgensen J. K., Choi M., Myers P. C., Mardones D., 2015, ApJ, 814, 22

Falceta-Gonçalves D., Lazarian A., Kowal G., 2008, ApJ, 679, 537

Ferrière K. M., 2001, Reviews of Modern Physics, 73, 1031

Fiege J. D., Pudritz R. E., 2000, MNRAS, 311, 85

Forbrich J., Lada C. J., Muench A. A., Alves J., Lombardi M., 2009, ApJ, 704, 292

Forbrich J., Posselt B., Covey K. R., Lada C. J., 2010, ApJ, 719, 691

Franco G. A. P., Alves F. O., 2015a, ApJ, 807, 5

Franco G. A. P., Alves F. O., 2015b, ApJ, 807, 5

Franco G. A. P., Alves F. O., Girart J. M., 2010, ApJ, 723, 146

Frau P., Girart J. M., Zhang Q., Rao R., 2014, A&A, 567, A116

Frau P., Girart J. M., Alves F. O., Franco G. A. P., Onishi T., Román-Zúñiga C. G., 2015, A&A, 574, L6

Friberg P., Bastien P., Berry D., Savini G., Graves S. F., Pattle K., 2016, in Holland W. S., Zmuidzinas J., eds, Society of Photo-Optical Instrumentation Engineers (SPIE) Conference Series Vol. 9914, Millimeter, Submillimeter, and Far-Infrared Detectors and Instrumentation for Astronomy VIII. p. 991403, doi:10.1117/12.2231943

Gaia Collaboration et al., 2016, A&A, 595, A1

Gaia Collaboration et al., 2021, A&A, 649, A1

Galametz M., et al., 2018, A&A, 616, A139

Galli D., Walmsley M., Gonçalves J., 2002, A&A, 394, 275

Galli D., Lizano S., Shu F. H., Allen A., 2006, ApJ, 647, 374

Galli P. A. B., et al., 2018, ApJ, 859, 33

Gerner T., Shirley Y. L., Beuther H., Semenov D., Linz H., Albertsson T., Henning T., 2015, A&A, 579, A80

Ginsburg A., Mirocha J., 2011a, PySpecKit: Python Spectroscopic Toolkit, Astrophysics Source Code Library, record ascl:1109.001 (ascl:1109.001)

Ginsburg A., Mirocha J., 2011b, PySpecKit: Python Spectroscopic Toolkit, Astrophysics Source Code Library, record ascl:1109.001 (ascl:1109.001)

Goldreich P., Kylafis N. D., 1981, ApJ, 243, L75

Goldsmith P. F., 2001, ApJ, 557, 736

Gómez G. C., Vázquez-Semadeni E., Zamora-Avilés M., 2018, MNRAS, 480, 2939

Goodman A. A., Bastien P., Myers P. C., Menard F., 1990, ApJ, 359, 363

Goodman A., Benson P., Fuller G., Myers P., 1993, The Astrophysical Journal, 406, 528

Goodman A. A., Barranco J. A., Wilner D. J., Heyer M. H., 1998, ApJ, 504, 223

Greaves J. S., Holland W. S., Ward-Thompson D., 2001, ApJ, 546, L53

Greene T. P., Wilking B. A., Andre P., Young E. T., Lada C. J., 1994, ApJ, 434, 614

Hacar A., Tafalla M., 2011, A&A, 533, A34

Hacar A., Tafalla M., Kauffmann J., Kovács A., 2013, A&A, 554, A55

Hall J. S., 1949, Science, 109, 166

Hecht E., 2017, Optics

Heiles C., Troland T. H., 2003, ApJ, 586, 1067

Heitsch F., 2013a, ApJ, 769, 115

Heitsch F., 2013b, ApJ, 776, 62

Heitsch F., Zweibel E. G., Mac Low M.-M., Li P., Norman M. L., 2001, ApJ, 561, 800

Hennebelle P., André P., 2013, A&A, 560, A68

Hennebelle P., Inutsuka S.-i., 2019, Frontiers in Astronomy and Space Sciences, 6, 5

Hennemann M., et al., 2012, A&A, 543, L3

Henshaw J. D., Caselli P., Fontani F., Jiménez-Serra I., Tan J. C., Hernandez A. K., 2013a, MNRAS, 428, 3425

Henshaw J. D., Caselli P., Fontani F., Jiménez-Serra I., Tan J. C., Hernandez A. K., 2013b, MNRAS, 428, 3425

Heyer M., Dame T. M., 2015, ARA&A, 53, 583

Hildebrand R. H., Kirby L., Dotson J. L., Houde M., Vaillancourt J. E., 2009, ApJ, 696, 567

Hill T., et al., 2011, A&A, 533, A94

Hiltner W. A., 1949, Science, 109, 165

Hoang T., Lazarian A., 2008, MNRAS, 388, 117

Holland W. S., et al., 2013, MNRAS, 430, 2513

Houde M., Vaillancourt J. E., Hildebrand R. H., Chitsazzadeh S., Kirby L., 2009, ApJ, 706, 1504

Hull C. L. H., Zhang Q., 2019a, Frontiers in Astronomy and Space Sciences, 6

Hull C. L. H., Zhang Q., 2019b, Frontiers in Astronomy and Space Sciences, 6, 3

Joos M., Hennebelle P., Ciardi A., 2012, A&A, 543, A128

Jørgensen J. K., et al., 2013, ApJ, 779, L22

Kauffmann J., Bertoldi F., Bourke T. L., Evans N. J. I., Lee C. W., 2008, A&A, 487, 993

Kennicutt R. C., Evans N. J., 2012, ARA&A, 50, 531

Keto E., Caselli P., 2008, ApJ, 683, 238

Kirk H., Myers P. C., Bourke T. L., Gutermuth R. A., Hedden A., Wilson G. W., 2013, ApJ, 766, 115

Koch E. W., Rosolowsky E. W., 2015, MNRAS, 452, 3435

Koenig X. P., Leisawitz D. T., 2014, ApJ, 791, 131

Könyves V., et al., 2010, A&A, 518, L106

Könyves V., et al., 2015, A&A, 584, A91

Kounkel M., et al., 2017, ApJ, 834, 142

Krumholz M. R., Crutcher R. M., Hull C. L. H., 2013, ApJ, 767, L11

Kylafis N. D., 1983, ApJ, 267, 137

Lada C. J., 1987, in Peimbert M., Jugaku J., eds, IAU Symposium Vol. 115, Star Forming Regions. p. 1

Lamarre J. M., et al., 2010, A&A, 520, A9

Larson R. B., 1981, MNRAS, 194, 809

Lazarian A., Hoang T., 2007a, MNRAS, 378, 910

Lazarian A., Hoang T., 2007b, MNRAS, 378, 910

Lazarian A., Yuen K. H., Pogosyan D., 2020, arXiv e-prints, p. arXiv:2002.07996

Lee J. W. Y., Hull C. L. H., Offner S. S. R., 2017, ApJ, 834, 201

Li Z.-Y., Krasnopolsky R., Shang H., 2013, ApJ, 774, 82

Li H. B., Goodman A., Sridharan T. K., Houde M., Li Z. Y., Novak G., Tang K. S., 2014a, in Beuther H., Klessen R. S., Dullemond C. P., Henning T., eds, Protostars and Planets VI. pp 101–123 (`arXiv:1404.2024`), doi:10.2458/azu_uapress_9780816531240-ch005

Li Z. Y., Banerjee R., Pudritz R. E., Jørgensen J. K., Shang H., Krasnopolsky R., Maury A., 2014b, in Beuther H., Klessen R. S., Dullemond C. P., Henning T., eds, Protostars and Planets VI. p. 173 (`arXiv:1401.2219`), doi:10.2458/azu_uapress_9780816531240-ch008

Li P. S., Lopez-Rodriguez E., Ajeddig H., André P., McKee C. F., Rho J., Klein R. I., 2022, MNRAS, 510, 6085

Lombardi M., Alves J., Lada C. J., 2006, A&A, 454, 781

Mac Low M.-M., Klessen R. S., 2004a, Reviews of Modern Physics, 76, 125

Mac Low M.-M., Klessen R. S., 2004b, Reviews of Modern Physics, 76, 125

Mac Low M.-M., Smith M. D., Klessen R. S., Burkert A., 1998, Ap&SS, 261, 195

Magalhaes A. M., Rodrigues C. V., Margoniner V. E., Pereyra A., Heathcote S., 1996, in Roberge W. G., Whittet D. C. B., eds, Astronomical Society of the Pacific Conference Series Vol. 97, Polarimetry of the Interstellar Medium. p. 118

Mangum J. G., Shirley Y. L., 2015, PASP, 127, 266

Maury A. J., André P., Men'shchikov A., Könyves V., Bontemps S., 2011, A&A, 535, A77

McClure-Griffiths N. M., Dickey J. M., Gaensler B. M., Green A. J., Haverkorn M., 2006, ApJ, 652, 1339

McGuire B. A., 2022, ApJS, 259, 30

McKee C. F., Ostriker J. P., 1977, ApJ, 218, 148

McKee C. F., Ostriker E. C., 2007, ARA&A, 45, 565

Mellon R. R., Li Z.-Y., 2008, ApJ, 681, 1356

Men'shchikov A., et al., 2010, A&A, 518, L103

Miville-Deschênes M. A., et al., 2010, A&A, 518, L104

Molinari S., et al., 2010, A&A, 518, L100

Mouschovias T. C., 1991, in Lada C. J., Kylafis N. D., eds, NATO Advanced Study Institute (ASI) Series C Vol. 342, The Physics of Star Formation and Early Stellar Evolution. p. 61, doi:10.1007/978-94-011-3642-6_3

Mouschovias T. C., Ciolek G. E., 1999, in Lada C. J., Kylafis N. D., eds, NATO Advanced Study Institute (ASI) Series C Vol. 540, The Origin of Stars and Planetary Systems. p. 305

Mouschovias T. C., Spitzer Jr. L., 1976, ApJ, 210, 326

Myers P. C., 2009, ApJ, 700, 1609

Myers P. C., 2011, ApJ, 735, 82

Nakamura F., Li Z.-Y., 2008, ApJ, 687, 354

Nakano T., Nakamura T., 1978, PASJ, 30, 671

Okoda Y., Oya Y., Sakai N., Watanabe Y., Jørgensen J. K., Van Dishoeck E. F., Yamamoto S., 2018, ApJ, 864, L25

Onken C. A., et al., 2019, Publ. Astron. Soc. Australia, 36, e033

Ortiz-León G. N., et al., 2018, ApJ, 869, L33

Ostriker J., 1964, ApJ, 140, 1056

Ostriker E. C., Stone J. M., Gammie C. F., 2001, ApJ, 546, 980

Padoan P., Nordlund Å., 1999, ApJ, 526, 279

Padoan P., Juvela M., Goodman A. A., Nordlund Å., 2001, ApJ, 553, 227

Palmeirim P., et al., 2013a, A&A, 550, A38

Palmeirim P., et al., 2013b, A&A, 550, A38

Pattle K., Fissel L., 2019, Frontiers in Astronomy and Space Sciences, 6, 15

Pattle K., Fissel L., Tahani M., Liu T., Ntormousi E., 2022a, arXiv e-prints, p. arXiv:2203.11179

Pattle K., Fissel L., Tahani M., Liu T., Ntormousi E., 2022b, arXiv e-prints, p. arXiv:2203.11179

Pattle K., Fissel L., Tahani M., Liu T., Ntormousi E., 2023, in Inutsuka S., Aikawa Y., Muto T., Tomida K., Tamura M., eds, Astronomical Society of the Pacific Conference Series Vol. 534, Protostars and Planets VII. p. 193 (`arXiv:2203.11179`), doi:10.48550/arXiv.2203.11179

Pelkonen V. M., Juvela M., Padoan P., 2009, A&A, 502, 833

Peretto N., et al., 2012, A&A, 541, A63

Peretto N., et al., 2014, A&A, 561, A83

Pilbratt G. L., et al., 2010, A&A, 518, L1

Pillai T. G. S., et al., 2020a, Nature Astronomy, 4, 1195

Pillai T. G. S., et al., 2020b, Nature Astronomy, 4, 1195

Pineda J. E., Segura-Cox D., Caselli P., Cunningham N., Zhao B., Schmiedeke A., Maureira M. J., Neri R., 2020, Nature Astronomy, 4, 1158

Planck Collaboration et al., 2016a, A&A, 586, A138

Planck Collaboration et al., 2016b, A&A, 586, A138

Planck Collaboration et al., 2016c, A&A, 586, A138

Planck Collaboration et al., 2016d, A&A, 594, A1

Polychroni D., et al., 2013, ApJ, 777, L33

Ramírez E. A., Magalhães A. M., Davidson Jr. J. W., Pereyra A., Rubinho M., 2017, PASP, 129, 055001

Rathborne J. M., Lada C. J., Muench A. A., Alves J. F., Lombardi M., 2008, ApJS, 174, 396

Redaelli E., et al., 2017, ApJ, 850, 202

Redaelli E., Bizzocchi L., Caselli P., Sipilä O., Lattanzi V., Giuliano B. M., Spezzano S., 2019a, A&A, 629, A15

Redaelli E., Alves F. O., Santos F. P., Caselli P., 2019b, A&A, 631, A154

Redaelli E., Alves F. O., Santos F. P., Caselli P., 2019c, A&A, 631, A154

Robitaille T. P., Whitney B. A., 2010, ApJ, 710, L11

Román-Zúñiga C. G., Alves J. F., Lada C. J., Lombardi M., 2010, ApJ, 725, 2232

Roy A., et al., 2014a, A&A, 562, A138

Roy A., et al., 2014b, A&A, 562, A138

Rybicki G. B., Lightman A. P., 1985, Radiative processes in astrophysics.

Rygl K. L. J., et al., 2013, A&A, 549, L1

Santos F. P., Busquet G., Franco G. A. P., Girart J. M., Zhang Q., 2016, ApJ, 832, 186

Schneider S., Elmegreen B. G., 1979, ApJS, 41, 87

Seifried D., Banerjee R., Pudritz R. E., Klessen R. S., 2015, MNRAS, 446, 2776

Serkowski K., 1973, in Greenberg J. M., van de Hulst H. C., eds, IAU Symposium Vol. 52, Interstellar Dust and Related Topics. p. 145

Serkowski K., Mathewson D. S., Ford V. L., 1975, ApJ, 196, 261

Skalidis R., Tassis K., 2021, A&A, 647, A186

Soler J. D., 2019, A&A, 629, A96

Soler J. D., et al., 2016, A&A, 596, A93

Soler J. D., et al., 2017a, A&A, 603, A64

Soler J. D., et al., 2017b, A&A, 603, A64

Spitzer L., 1978, Physical processes in the interstellar medium, doi:10.1002/9783527617722.

Stahler S. W., Palla F., 2004, The Formation of Stars

Stephens I. W., Looney L. W., Dowell C. D., Vaillancourt J. E., Tassis K., 2011, ApJ, 728, 99

Sugitani K., et al., 2011, ApJ, 734, 63

Tabatabaei F. S., Redaelli E., Caselli P., Alves F. O., 2023, A&A, 672, A72

Tabatabaei F. S., Redaelli E., Galli D., Caselli P., Franco G. A. P., Duarte-Cabral A., Padovani M., 2024, A&A, 688, A98

Tachihara K., Dobashi K., Mizuno A., Ogawa H., Fukui Y., 1996, PASJ, 48, 489

Tassis K., Mouschovias T. C., 2005, ApJ, 618, 783

Thompson A. R., Moran J. M., Swenson Jr. G. W., 2017, Interferometry and Synthesis in Radio Astronomy, 3rd Edition, doi:10.1007/978-3-319-44431-4.

Toci C., Galli D., 2015a, MNRAS, 446, 2110 (TCa)

Toci C., Galli D., 2015b, MNRAS, 446, 2118 (TCb)

Tomisaka K., 2015, ApJ, 807, 47

Ward-Thompson D., Motte F., Andre P., 1999, MNRAS, 305, 143

Ward-Thompson D., André P., Crutcher R., Johnstone D., Onishi T., Wilson C., 2007, in Reipurth B., Jewitt D., Keil K., eds, Protostars and Planets V. p. 33 (arXiv:astro-ph/0603474), doi:10.48550/arXiv.astro-ph/0603474

Ward-Thompson D., et al., 2010, A&A, 518, L92

Wilson T. L., Rohlfs K., Hüttemeister S., 2009, Tools of Radio Astronomy, doi:10.1007/978-3-540-85122-6.

Wurster J., 2021, MNRAS, 501, 5873

Yen H.-W., Koch P. M., Takakuwa S., Krasnopolsky R., Ohashi N., Aso Y., 2017, ApJ, 834, 178

Yen H.-W., et al., 2021, ApJ, 907, 33

Zhang C.-P., Yuan J.-H., Li G.-X., Zhou J.-J., Wang J.-J., 2017, A&A, 598, A76

Zhang X., Green G. M., Rix H.-W., 2023, MNRAS, 524, 1855

Zucker C., Chen H. H.-H., 2018, ApJ, 864, 152

Zuckerman B., Palmer P., 1974, ARA&A, 12, 279

van Kempen T. A., van Dishoeck E. F., Hogerheijde M. R., Güsten R., 2009, A&A, 508, 259

Acknowledgements

Completing my PhD here has been an incredible journey—one that has shaped me in ways far beyond academics. These four years have been a mix of excitement, struggles, and personal growth, filled with both triumphs and moments of exhaustion and doubt. Looking back, I wouldn't trade a single moment, as every experience, whether uplifting or overwhelming, has contributed to who I am today. This journey would not have been the same without the people who supported, challenged, and inspired me along the way.

I am deeply grateful to my supervisors, Paola Caselli and Elena Redaelli, without whom none of this would be possible. Paola, I cannot thank you enough for everything—from giving me the opportunity to begin my research career in your group to your invaluable guidance, trust, and support throughout these years. Your encouragement not only shaped my academic growth but also helped me find a healthy balance between work and life, for which I am truly grateful. Elena, I have learned from you. Your mentorship has shaped my research journey, allowing me both independence and the reassurance of your advice whenever needed, which I truly appreciate. Your patience, whether in answering my smallest questions or tackling complex problems, has been a constant source of motivation.

To all my friends, you have been my incredible supporters, making this journey more bearable with your kindness, humor, patience, and encouragement. There are countless friends to thank, but I would like to extend a special mention to Shayeste and Niloofar, our endless conversations helped me through my most challenging days. Anirvan, thanks for your endless support and always being there during the difficult moments of my time in Munich.

Finally, my sincere gratitude goes to my parents, for shaping me into the person I am today. From a young age, you nurtured my curiosity and passion for science, giving me the freedom to follow my own path, even when our perspectives differed. This achievement is as much yours as it is mine.